University of Strathclyde

Department of Naval Architecture, Ocean and Marine Engineering

THE DEVELOPMENT OF A REAL-TIME WAVE ENERGY DEVICE CONTROL ALGORITHM BASED ON ARTIFICIAL NEURAL NETWORK

by

Liang Li

A thesis submitted in fulfillment of the requirements for the degree of Doctor of Philosophy

October 2018

This thesis is the result of the author's original research. It has been composed by the author and has not been previously submitted for examination which has led to the award of a degree.

Singed: Date:

Table of Contents

Abstract

This thesis is aimed at proposing an artificial intelligence controller to maximize the energy absorption of wave energy converter (WEC) in practical application. The controller maximizes the energy absorption by locking and releasing the WEC alternately, and such control is known as the latching control. The model predictive control strategy is used to implement real-time control. Since the control inputs are future wave forces, the controller is a non-causal system. An artificial neural network is developed and trained by the machine learning algorithm to predict the short-term wave forces.

Firstly, the state-space dynamic model is developed to simulate the kinetic motion of the WEC in sea waves. Compared with traditional convolution dynamic model, the state-space representation extremely enhances the computation efficiency. Moreover, the state-space model is represented by a differential formula so that it is more convenient to implement the control algorithm. The state-space model is acquired based on the so-called system identification, which transforms the frequency-domain hydrodynamic coefficients of the WEC into a set of state vectors. A Rankine source boundary element method code is developed to calculate the hydrodynamic coefficients. By separating the entire fluid boundary into a set of elements and distributing the Rankine source across the elements uniformly, the velocity potential of the fluid is determined.

The latching control, a kind of phase control, maximizes the energy absorption by tuning the velocity phase and making it in phase with the wave excitation forces. The tuning of velocity phase is fulfilled by locking the WEC at some time instants following the control command. The Pontryagin's maximum principle is applied to derive the control command, which maximizes the energy absorption over a time horizon $[t_i, t_{i+p}]$. By receding the time horizon forward step by step, the control command is updated at each time instant and thereby the control is implemented in a real-time manner. It is the basic idea of the model predictive control. Since the derived control command just maximizes the energy absorption over the time horizon $[t_i, t_{i+p}]$

rather than the entire interval [0, *T*], the model predictive control is a sub-optimal control strategy.

The inputs to a non-causal wave energy controller are future wave forces, and it is what prevents the practical application of wave energy control. An artificial neural network is developed to predict the short-term wave forces. Unlike traditional deterministic forecasting approach, which is based on a specific model defined by the users, the neural network forecasts the future wave forces by learning from examples itself since even the users don't know anything about the prediction model. In another word, the neural network is a data-driven prediction approach. The developed neural network is trained by a set of examples using the machine learning algorithm.

With the artificial neural network, the real-time smart controller is incorporated into a heaving-point absorber to maximize the energy absorption. It is shown that the energy absorption is indeed increased substantially even if the wave forces are predicted. It indicates that the real-time controller is applicable in the real practice. Besides, the effects of prediction duration and prediction deviation on the control performance are also investigated. Long prediction duration enhances the control efficiency whereas the energy absorption is reduced with the presence of prediction deviation. Since the deviation accumulates with the prediction duration, a moderate prediction duration is thus recommended.

The multi-stable mechanism of the WEC is also investigated in this thesis. A non-linear PTO (power take-off) system with two oblique springs is proposed. The PTO system is either monostable or bistable depending on the initial configuration of the oblique springs. Correspondingly, a single-well potential or a double-well potential is identified. The behaviors of the WEC show considerable discrepancies in the two modes. At the monostable mode, the WEC responds to the waves in a linear manner. The energy absorption and bandwidth are hardly varied compared with a linear WEC. Comparatively, the WEC operates with a distinguished mechanism at the bistable mode. Two types of floater responses are identified. The energy capture is significantly increased although the bandwidth is narrowed at the same time. The enhancement of

energy absorption is mainly attributed to the tuning of the velocity phase, which occurs when the floater moves around the two potential wells.

Acknowledgements

I am deeply indebted to Dr. Zhiming Yuan for giving me the academic freedom to work on the topic which I am really interested in. It is my great honor to cooperate with him and do my postgraduate research under his supervision. Thanks to his open mind, idea and generous financial support, I had an enjoyable and unforgettable time during the past three years in Glasgow.

I would like to express my gratitude to Professor Atilla Incecik for this kind support during my PhD project. Many thanks are due to Professor Zhen Gao for his valuable comments on the wave energy control during my visit to NTNU.

I would like to thank Mrs. Susan Pawson and all other staff in the department of NAOME for their kind help with all the administrative issues.

Finally, I want to dedicate this thesis to my parents for their unconditional love, support and encouragement throughout my life.

List of Figures

List of Tables

Nomenclature

ρ	Water density
g	Acceleration of gravity
ω	Wave oscillating frequency
C	Damping coefficient of the PTO system
K	Stiffness of the PTO system
c	Damping efficient of the latching force
$\boldsymbol{\Phi}$	Velocity potential
φ	Spatial velocity potential
φ_D	Diffraction velocity potential
φ_I	Incident wave velocity potential
φ_i (i = 1,2,…,6)	Radiation velocity potential
A	Wave amplitude
μ	Added mass
λ	Potential damping
ψ	Wave force transfer function
σ	Rankine source strength
G	Rankine source green function
$\vec{\boldsymbol{A}}$, $\vec{\boldsymbol{B}}$ and $\vec{\boldsymbol{C}}$	System matrix of the state-space model
β	Latching control command
$\boldsymbol{\chi}$	Lagrange multipliers
$\boldsymbol{w}$	Weight of neural network
$\boldsymbol{b}$	Bias of neural network
Θ	Cost function of neural network
ϕ	Learning rate
ν	Up-crossing rate

1. Introduction

1.1. Background

Since the first proposal of wave energy concept [1], ocean wave has been accepted as a prospective solution to the sustainable generation of power due to its high power density and all-day availability. The device used to harvest energy from ocean wave is known as the wave energy converter (WEC). The operation mechanism of WEC can be briefly separated into three categories: oscillating-buoy, pressure differential and overtopping.

Despite that WEC concept with various types of energy extracting mechanisms have been proposed, most full-scale WEC products belong to the oscillating-buoy group [2-4]. A remarkable advantage of the oscillating-buoy WEC is the high-level reliability of its power take-off (PTO) system, e.g. a direct-drive generator or a hydraulic motor. However, the energy harvesting efficiency is sometimes unsatisfactory, especially within the off-resonance range, since the power is extracted from the inertial motion of the floater. One of the solutions to solve this problem is the incorporation of wave energy control. Genest and Ringwood [5] applied the pseudospectral control to maximize the energy extraction of an oscillating-buoy WEC. Sclavounos and Ma [6] increased the energy extraction by controlling the damping of the PTO system. Alternatively, the multi-stable mechanism can also be used to increase the energy harvesting efficiency of a WEC in random waves. Kurniawan and Zhang [7] applied the multi-stable mechanism to a pitching WEC to improve its energy harvesting.

Early control strategies were all based on the assumption that the inputs (the wave force) to the controller are fully known. Since the energy absorption is maximized over the entire interval concerned, such a control algorithm is also called the optimal control. Apparently, the optimal control algorithm is not applicable in practice since the long-term wave force information is unpredictable. Recently, the model predictive control algorithm has been widely applied in the maximization of wave energy harvesting. Instead of maximizing the energy absorption over the entire interval, the model predictive control seeks the optimum over a short time horizon in the future. By

receding the time horizon forward step by step, the model predictive control is implemented online and in a real-time manner. Since the model predictive control just requires short-term wave forces over the time horizon, it shows prospect in the practical application.

For either the optimal control or the model predictive control, the control inputs are future wave forces so that the controller is a non-causal system. Obviously, the wave force prediction is important to the successful implementation of the wave energy control. Thanks to the explosive growth of the artificial intelligence, the machine learning algorithm is being widely used for regression analysis, allowing us to predict the wave forces using an alternative approach. The application of artificial intelligence for short-term prediction is initially seen decades ago in traffic science. Smith and Demetsky [8] compared the neural network and nonparametric regression approaches for the prediction of the traffic flow in a highway. A similar approach was adopted by Dougherty and Cobbett [9] to predict the traffic flow, speed and occupancy in the Netherlands. Afterward, the artificial intelligence is introduced to the energy management. Yu and Xu [10] utilized the backpropagation neural network to forecast the short-term natural gas loading at city Shanghai based on the local population. Fadare [11] predicted the solar energy potential in Nigeria based on the past 10-year measured geographical and meteorological data in the local area. More recently, researchers begin to adopt the artificial intelligence to improve the energy efficiency of renewable energy systems. Kalogirou [12] presented a comprehensive review of the applications of artificial neural networks in renewable energy systems. One of the specific applications is the prediction of inputs to the control systems.

Recently, the community of wave energy starts to utilize the multi-stable mechanism to increase the energy conversion efficiency. One remarkable advantage of the non-linear system is the potential capability of energy harvesting in a wide range of frequency [13]. Based on previous publications, the multi-sable mechanism is a prospective solution to the enhancement of wave energy conversion. Lopez et al. [14] examined the influence of PTO system configuration on the performance of the so-called CECO system under a wide range of wave conditions. Zhang and Yang [15] showed that a PTO system with non-linear spring could harvest more energy in random

waves. They all showed that the energy absorption could be enhanced with a non-linear PTO system.

1.2. Research objective

The work in this thesis is mainly aimed at developing a real-time control algorithm with the ability of wave force prediction so that it can be implemented directly to a realistic industrial WEC product and bring economic benefits to the wave energy industry. The specific research targets are listed as:

- To develop a numerical approach to simulate the dynamics of WECs efficiently and precisely
- To develop a real-time control algorithm
- To develop a reliable wave force prediction approach that can be used in the real-time control algorithm
- To develop a multi-stable mechanism to increase the wave energy extraction

1.3. Research methodology

This thesis conducts an inter-disciplinary research, and three main aspects are addressed in accordance with the research targets listed above: wave-structure interaction, real-time non-causal control, dynamic process prediction.

1.3.1. Wave-structure interaction

Assuming that the wave flow is irrotational, and the fluid is inviscid and incompressible, and , the velocity potential is a valid description of the fluid field. A boundary element method based on the Rankine Green function is developed to address the frequency-domain hydrodynamic coefficients (added mass, radiation damping, wave excitation forces) of the WEC. A state-space model is subsequently developed with the frequency-domain hydrodynamic coefficients to simulate the time-domain movement of a floating body in random sea waves.

1.3.2. Control algorithm

The model predictive control algorithm is adopted to implement real-time control to the WEC, which maximizes the energy absorption over a receding time horizon [t_i, t_{i+p}]. From a mathematical point of view, it is to find the maximal value of energy absorption subject to a constraint dynamical model of the WEC. The energy absorption is maximized by the Pontryagin's maximum principle [16] through the introduction of the Hamiltonian.

1.3.3. Wave force prediction

The short-term wave forces are predicted using the artificial intelligence technology. An artificial neural network with multi-layers is developed to predict future wave forces based on the measured past wave forces. The neural network is trained with the machine learning algorithm to model the underlying relation between future force and past force via a large amount of training examples. The training examples are generated numerically based the Airy wave model (Please refer to Eq. (3.15) in Chapter 3.4).

1.4. Main contribution

The main contribution in this thesis is to introduce the machine learning algorithm to the short-term wave force prediction and utilize it in the real-time control of wave energy converter. In previous wave energy control studies, the future wave forces were assumed already known preventing the practical application of wave energy control. A predictive real-time control algorithm based on the artificial neural network is developed in this thesis, which shows great prospect in the practical application.

Additionally, the multi-stable mechanism of wave energy converter is also investigated, which may act as an alternative approach to enhance the energy extraction efficiency.

1.5. Thesis structure

This thesis is structured in the following chapters and a brief outline of the content of each chapter is given below:

- Chapter 1 Introduction

  Give a brief introduction to the background of WEC control and summary the object of the research in this thesis. The methodology that will be adopted in the research is interpreted briefly as well.

- Chapter 2 Literature Review

  Present a detailed and comprehensive literature review on the WEC control, the multi-stable mechanism of WEC, and the hybrid offshore renewable energy system.

- Chapter 3 Hydrodynamic Model of the WEC

  Interpret how the boundary element method adopted and the state-space representation are used to develop the dynamic model of the WEC in ocean waves. The dynamic model is also validated in this chapter.

- Chapter 4 Real-time Control Algorithm

  Present details on how the real-time control algorithm is developed.

- Chapter 5 Wave Force Prediction with Artificial Neural Network

  Predict the wave forces using the artificial neural network. The development of the multi-layer neural network and how the neural network is trained with the machine learning algorithm will be interpreted.

- Chapter 6 Control Effect on Energy Absorption

  Demonstrate the energy absorption with the implementation of the real-time controller. The effects of prediction error and prediction horizon will be discussed.

- Chapter 7 Control Effect on Extreme Response and Fatigue Damage Load

  Investigate the real-time control effect on the extreme response and the fatigue damage load.

- Chapter 8 Multi-stable Mechanism

Examine how the multi-stable mechanism is utilized to enhance the energy absorption

- Chapter 9 Conclusions

  Present the achievements in this thesis and outline future work plan

Figure 1-1 summaries the work flow. A multi-layer neural network is developed to approximate the underlying relations between the past wave forces and the future wave forces. The neural network is trained with the machine learning algorithm. The trained neural network is used for the short-term wave force prediction. The predicted wave forces are imported to the controller, which maximizes the energy extraction of the WEC.

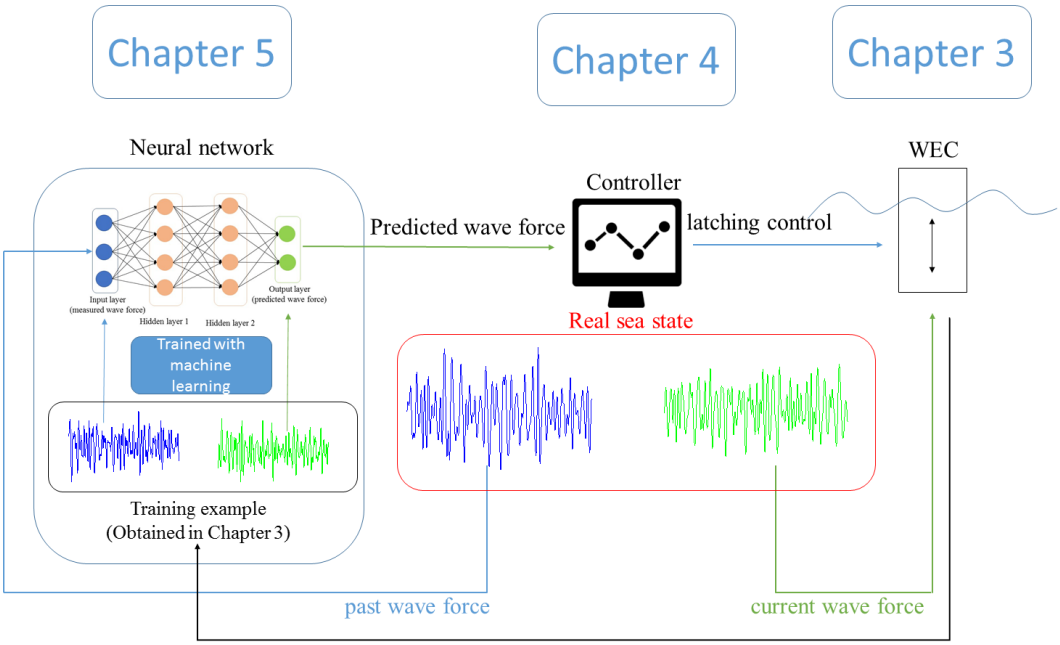

Figure 1-1 Work flow.

2. Literature Review

It is expected that the global demand for energy will climb up to 25 percent by 2040 and the world is pursuing economic and renewable energy sources to keep up with this considerable demand growth [17]. Compared with other ocean energy resources, wave energy is a kind of resource with high power density and all-day availability. Owing to these advantages, wave energy is regarded as a prospective solution to the sustainable generation of power. Ocean wave are mainly generated by the offshore wind passing over the surface of the sea. If the waves propagate more slowly than the wind, there is an energy transfer from the wind to the waves. In linear wave theory, the motion of a fluid particle is elliptical, and the oscillation motion is highest at the surface. In a specific sea state, the average wave energy density per unit area at free surface is proportional to the square of wave height

$$E = \rho g \int_0^\infty S(\omega) d\omega = \rho g H_s^2 / 16 \tag{2.1}$$

where ρ is the water density; g is the acceleration of gravity; H_s the significant wave height for the actual sea state. ω is the wave frequency and $S(\omega)$ is the wave spectrum. Due to the elliptical motion of the fluid particle, the wave energy is partitioned between the kinetic energy (velocity) and the potential energy (displacement). Therefore, these two types of stored energy can be utilized to produce electrical power.

2.1. Wave energy converter

The device used to extract energy from the ocean waves is commonly known as the wave energy converter. A typical WEC consists of two main components: the mechanical interface and the power take-off system. The mechanical interface is the structure of the WEC, determining how the wave energy is harvested. Some mechanical interfaces harvest the kinetic energy whereas others collect the potential energy. The PTO system is the device that converts the harvested wave energy into the electrical energy.

2.1.1. Energy conversion mechanism

Depending on the energy conversion mechanism, WEC can be briefly categorized into three groups: pressure differential, overtopping, and oscillating-buoy.

Oscillating-water column WEC

This type of WEC does not utilize the potential energy or the kinetic energy directly. Instead, it uses the wave motion to produce a pressure differential inside and outside the chamber, which is utilized to drive a turbine or a piston connected to the generator. The oscillating-water-column WEC usually carries a submerged chamber and a turbine. The oscillation of the piston will compress and extend the air inside the chamber, and then the pressure differential drives the turbine to produce power.

He et al. [18] integrated asymmetric pneumatic chambers to a floater breakwater to harvest energy from the waves. The combined concept was proposed to increase the amplitude of the oscillating air-pressures inside both chambers over a wide range of frequency. Experimental study of the concept was performed. Babarit et al. [19] investigate the energy absorption performance of a fixed-bottom pressure-differential wave energy converter. Their study indicated that the pressure-differential wave energy converter is a feasible technology both with respect to energy absorption and selected economic performance indicators. Zhang et al. [20] used a two-phase flow model to investigate the air-wave interaction of an oscillating-water-column WEC. Their simulations showed that the bandwidth of energy absorption was narrow and centered around the resonant frequency.

Overtopping WEC

An overtopping WEC produces power by converting the potential energy of the wave. The idea of an overtopping WEC is to store the water close to the wave crest into a reservoir by over spilling. The reservoir is higher than the average free sea level so that the store water carries potential energy. This kind of WEC works very like a hydroelectric dam. Apparently, the strong non-linear hydrodynamics is involved here.

Due to the complex energy conversion mechanism, the type of WEC is not fully investigated and most studies apply model test method.

In the early 1980s, Tapchan was proposed in Norway [21]. The Tapchan comprises a collector, a converter, a water reservoir, and a low-head water-turbine. The horn-shaped collector was used to concentrate the incoming waves before they enter the converter. The converter is a gradually narrowing channel with wall heights equal to the filling level of the reservoir. As a result, the wave energy is gradually transformed into potential energy in the reservoir. Then, the stored water will drive the turbine to produce power. Margheritini et al. [22] investigated the reliability and hydraulic performance of an innovative overtopping device 'Sea Slot-cone Generator'. The structure consists of a number of reservoirs on the top of each other above the mean water level in which the water of incoming waves is stored temporarily. In each reservoir, expressively designed low head hydro-turbines are converting the potential energy of the stored water into power. Although the structure cost of the SSG was low, the energy absorption efficiency was unsatisfactory. Vicinanza et al. [23] came up with an innovative overtopping WEC on the basis of breakwaters. Turbines were installed to harvest energy from waves overtopping in a front reservoir.

Oscillating-buoy WEC

For a floating body subject to sea waves, it will oscillate under the cyclic loads of waves. The movement carries kinetic energy and can be converted to electricity power. It is the energy conversion mechanism of the oscillating-buoy WEC. An oscillating-buoy WEC is commonly composed of two bodies, the floater, and the basement. The basement is fixed at the seabed or moored in the sea with a mooring system. The floater is displaced in the sea waves and subject to the wave loads. The relative motion between the floater and the basement is used for energy production. The oscillating-buoy WEC is more welcomed compared with the above two since the energy conversion mechanism is very simple. Moreover, the wave-structure interaction can be commonly addressed by linear wave theory.

Masubuchi and Kawatani [24] developed a frequency-domain response model of a two-body WEC in regular waves. The hydrodynamic interactions were considered.

They showed that the energy absorption efficiency was sufficiently high within a wide frequency band. Due to the limitation of the computation capacity at that time, only linear WECs with simple PTO system (usually simplified as a damper-spring system) could be addressed. Nowadays, studies on non-linear oscillating-buoy WECs become feasible thanks to the progress of simulation tools. Younesian and Alam [25] utilized a non-linear PTO system characteristic of multi-stable mechanism to enhance the energy absorption efficiency and broaden the bandwidth. It was shown that the non-linearity of the PTO system brought a lot of benefits to the energy absorption. Zhang et al. [26] took the advantage of non-linear snap-through to improve the energy harvesting of a heaving point-absorber. The non-linear snap-through mechanism was characteristics of negative stiffness and double-well potential. They showed that the energy absorption was enhanced significantly by the snap-through mechanism. Xiao et al. [27] performed a comparative study on the power capture performance of an oscillating-buoy WEC with three PTO systems: a bistable impulsive PTO, a coupled linear PTO, and a coupled bistable PTO.

2.1.2. Power take-off system

Regardless of the energy conversion mechanism, the final output of a WEC is the electrical energy which must be generated by a kind of electrical device. The most frequently used power take-off devices are the air turbine, the hydraulic generator, and the direct drive generator.

Air turbine

A WEC equipped with an air turbine operates fundamentally like a wind turbine. Unlike a wind turbine, the air flow driving the turbine is generated by the pressure differential in a chamber. Consequently, the air turbine is commonly seen in a pressure differential WEC. The pressure differential is generated either by a piston or the inner wave elevation in a chamber. Since the sea waves are periodic, the air flow going through the turbine is reciprocating so that the efficiency of the turbine is substantially lower than other PTO systems. A solution to this problem is the installation of a rectifying system. Wells [28] invented a self-rectifying axial-flow turbine, the famous Wells turbine. The torque of the Wells turbine is not sensitive to the air flow direction,

and thereby it can operate with a relatively stable efficiency. Several modified versions of the Wells turbine have been proposed (see Figure 2-1 and Figure 2-2), and the impulse turbine [29] seems to be the most popular one among them. Its rotor is basically identical to the rotor of a conventional single-stage steam turbine of axial-flow impulse type. Two tows of guide vane are placed symmetrically on the rotor to self-rectify. The Denniss-Auld turbine [30] is another self-rectifying turbine, which shares some characteristics with the Wells turbine. The angle of stagger of a Denniss-Auld turbine is adjustable. Although self- rectifying turbine behaves much better than the classical turbine, the average efficiency is still moderate.

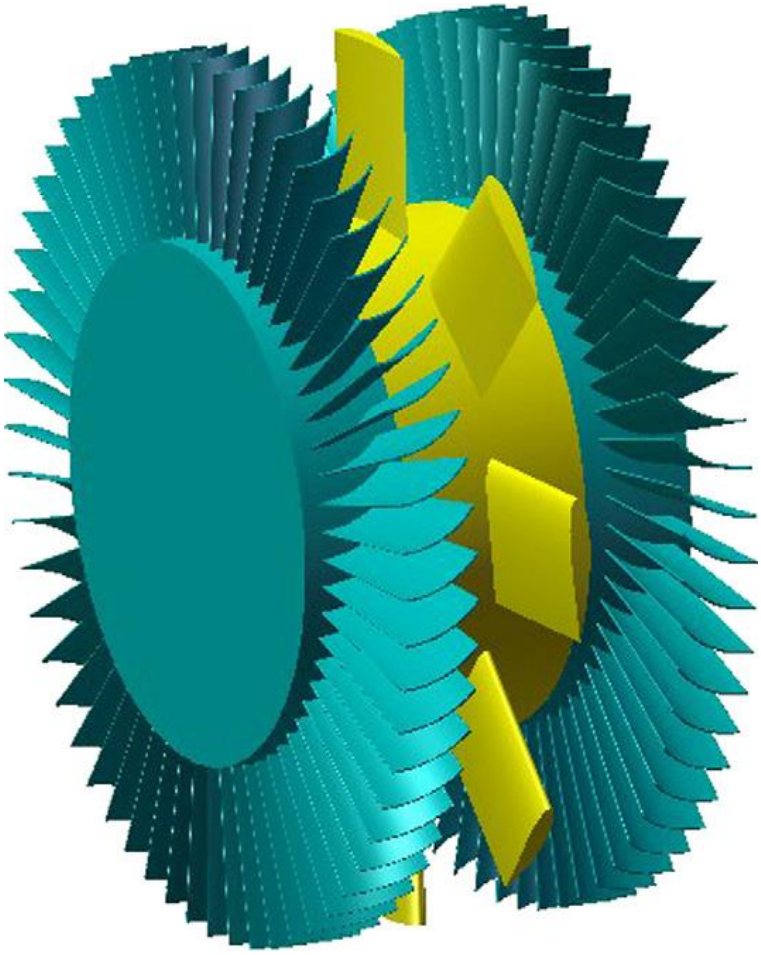

Figure 2-1 Wells turbine, the version with guide vanes [31].

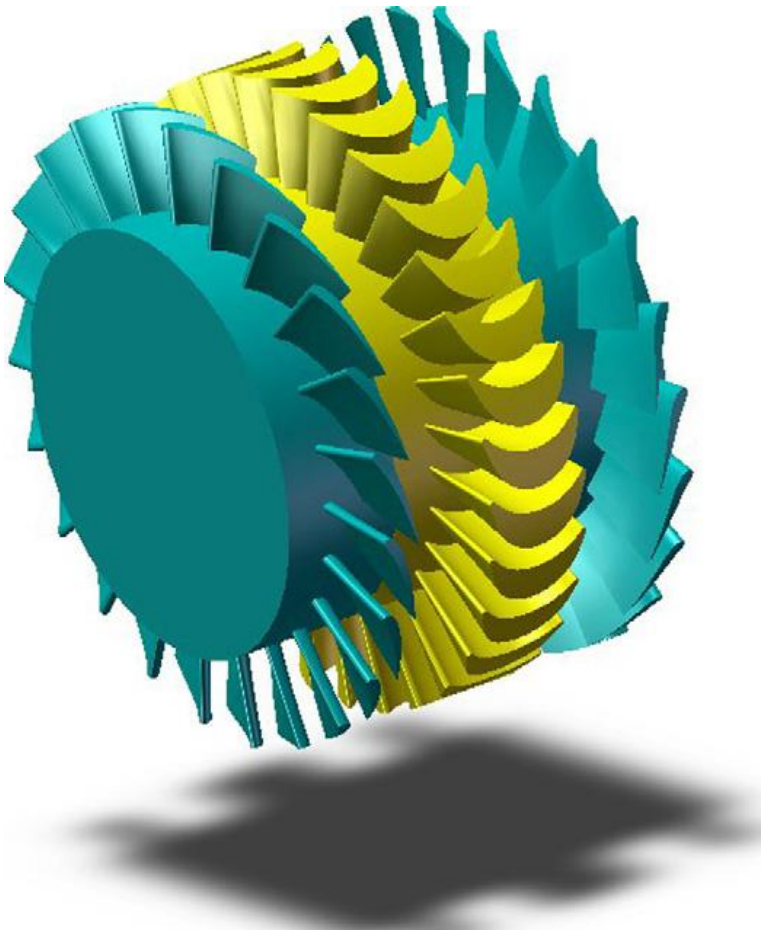

Figure 2-2 Impulse turbine [31].

Hydraulic generator

The hydraulic generator usually includes a gas accumulator system capable of storing energy over a few wave periods, which can smooth out the very irregular power absorbed from the waves. The body motion is converted into hydraulic energy by a hydraulic cylinder or ram (or a set of them). A high-speed hydraulic motor drives a conventional electrical generator. The hydraulic PTO system is particularly suitable to convert energy from the very large forces or moments applied by the waves on slowly oscillating bodies. The hydraulic PTO system is typically used in an oscillating-buoy WEC. Compared with the air turbine, the hydraulic generator is obviously a much more complicated machine so that its main disadvantage is the reliability.

Direct drive generator

For most WECs, a rotating electrical generator is driven by a mechanical interface: air turbine or hydraulic motor. The electrical equipment is largely similar to the wind turbine generator. Comparatively, the direct drive generator is another category, which does not require the mechanical interface. Since the mechanical interface is removed, the efficiency loss taking place in the mechanical interface is avoided. As shown in Figure 2-3, a typical direct drive generator consists of the coil (translator) and the magnet (stator). When the WEC oscillates under the excitation of sea waves, it will carry the stator and the magnet assembly creates a change in the magnetic field, producing current in the coil.

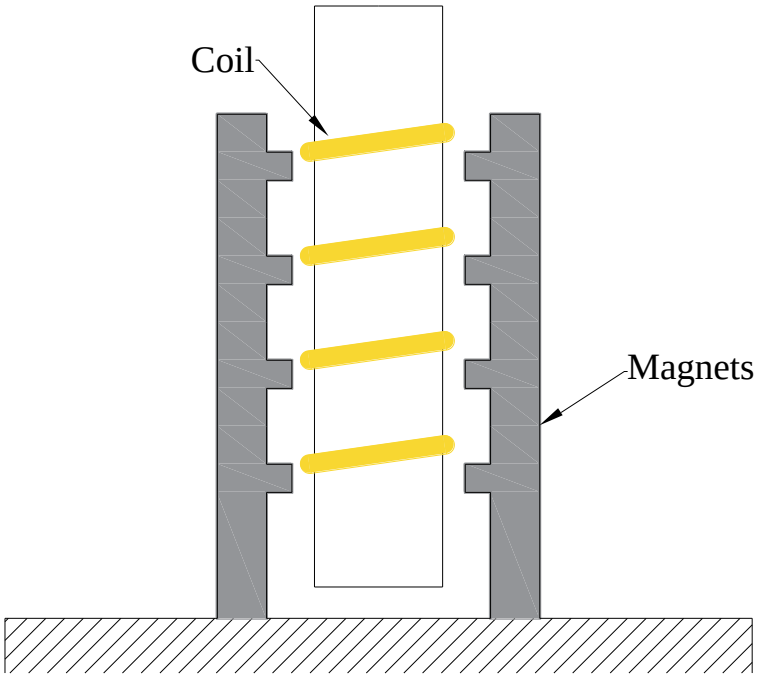

Figure 2-3 Direct drive generator.

2.1.3. Industrial product

Although the WEC has been investigated scientifically for decades, it is until recently that full-scale industrial concepts are proposed.

The Wave Dragon concept [2], the world's first offshore grid-connected wave energy device, was first tested in 2004. Wave Dragon is a typical representation of the overtopping WEC. This test unit supplied electricity to the grid in more than 20,000

hours. The Aquamarine Power tested the Oyster 800 at Billie Croo test site from 2012 to 2015. During this period, the Oyster kept connecting to a grid. The Pelamis project was launched by Pelamis Wave Power [3] in 2014, which successfully provided power to the national grid of Scotland. The Pelamis is the world's first offshore wave power converter to successfully generate electricity into a national grid. In the same year, the Archimedes Waveswing proposed by AWS Ocean Energy Ltd [32] was tested in Portugal. This product produces power from the changes in sub-sea water pressure caused by passing flow. Ocean Power Technologies [33] developed the PowerBuoy. This concept is a kind of oscillating-buoy WEC and integrates intelligent computer control systems to maximize the extraction and conversion of the natural energy in ocean waves. The United States Department of Energy proposed the Azura concept [4], which has been supplying energy to the power grid in North America.

2.2. Wave-structure interaction

Despite that various energy absorption mechanisms have been developed and applied, the WEC must be placed in the oceans. Therefore, the wave-structure interaction is one of the essential issues in the investigation of WEC. Until now, two categories of approaches are basically adopted to simulate the dynamic performance of a WEC subject to sea waves.

The first approach is the computational fluid dynamics (CFD) method [34], which is boosted by the rapid progress of computation devices. The CFD method is aimed at solving the Navier-Stokes equations using the finite differences equation. Zhang et al. [20] used the finite volume method to examine the energy extraction of an oscillating water column WEC. The flow field, the free surface, and the pressure distribution were fully represented. Devolder et al. [35] used the CFD toolbox OpenFOAM to perform numerical simulations of multiple floating point-absorber WECs arranged in a geometrical array. With the consideration of the viscous effect of the flow, their numerical model gave an accurate prediction against the model test measurement. The CFD method is able to give a full and detailed description of the fluid field and take the non-linearity of wave-structure interactions into account. One drawback of the CFD method is that it consumes an enormous of computation resources.

Another state-of-the-art approach is the potential flow theory. Thanks to the high computation efficiency of the potential flow method, it has been widely adopted in the development of the WEC mathematical model. The potential flow theory simplifies the Navier-Stokes equations by removing the viscous. The fluid field is described by the velocity potential, which is a scalar and satisfies the Laplace equation within the fluid domain and thereby the calculation of the velocity potential can be addressed as the boundary value problem from a mathematical point of view. The potential flow theory is initially applied in the seakeeping problem, which aims to get the dynamics of a floating body in sea waves. Faltinsen [36] gave a comprehensive interpretation of the boundary element method and how it was applied to calculate the motions of a floating structure in sea waves. Newman [37] presented how the boundary integral equation was established in detailed. Cummins [38] developed the impulse response theory based on the potential flow theory and gave a generic domain-model of floater motions in stochastic waves. His approach is one of the most widely used methods in WEC dynamic model. In the impulse response theory, the wave radiation force is represented by the convolution term, which reduces the calculation efficiency. Most recently, the state-space model is gradually adopted by researchers to replace the impulse response model. The state-space model represents a physical system as a set of input, output and state variables. It has been shown to dramatically increase computational speeds and allow utilization of conventional control methods that rely on linear state space models [39]. The identical method was adopted in Zhang et al. [40] as well.

2.3. Wave energy control

As discussed above, a hydraulic motor or a direct drive generator typically is used by an oscillating-buoy WEC to convert the wave energy. In this circumstance, the PTO system can be approximated as a linear spring-damper system. It is well-known that a linear oscillation system is sensitive to the excitation frequency. The early theoretical studies on the oscillating-buoy WEC revealed that, if the device is to be an efficient absorber, its own frequency of oscillation should match the frequency of the incoming waves, i.e. it should operate at near-resonance conditions [31]. This can be achieved easily by adjusting the parameters (e.g. damping, spring, and inertia) of the WEC. The

real sea waves are not monochromatic but consist of components with various oscillating frequencies so that the energy efficiency of a pure oscillating-buoy WEC is generally unsatisfactory. A solution to this problem is to apply active control to the WEC.

The primary aim of an active wave energy control is to maximize the average power output under the constraint set by the energy device. Additionally, a control system may also be implemented to help in protecting the device and its machinery under severe storm conditions. This thesis merely considers the energy maximization. Also, the control algorithm for WECs with various energy conversion mechanisms vary significantly and this thesis only discusses the wave energy control for body-oscillating WEC.

2.3.1. Latching and declutching control

Among various control strategies [5, 41, 42], the phase control may be the most commonly used control approach, which tunes the response phase and makes the response in phase with the wave forces to acquire resonance. The latching control and the declutching control are two typical representations of the phase control family. The declutching control enhances energy absorption by switching on and off alternatively the PTO system. The PTO system is switched off during part of the wave cycle to let the velocity build up rapidly. When the velocity run up to sufficient level, the PTO system is switched on again to produce power again. Babarit et al. [43] studied how the declutching control influenced the energy absorption of a WEC in regular and irregular waves. Comparatively, the latching control works by locking and releasing the PTO system occasionally. By controlling the phase between the velocity and the wave force, the wave force is always accelerating the floater and thereby the energy absorption reaches the optimal value. The latching control was firstly introduced by Budal and Falnes [44]. Babarit and Clement [45] assessed the benefits produced by the latching control. Based on the pre-generated wave elevations, the optimal command theory was applied to determine the control command. Greenhow and White [46] studied the relation between energy absorption and latching duration in regular waves. Hoskin and Nichols [47] used optimal command theory to derive the optimal

latching duration. Babarit et al. [48] compared different latching control strategies of a WEC in the random sea. When the control strategy was designed to maximize different variables (the amplitude of motion, the amplitude of velocity, etc), the performance of the WEC showed discrepancies.

2.3.2. Real-time implementation of control

In addition to the control algorithm, how the control is implemented is another crucial issue of wave energy control. Early control algorithms aimed to maximize the energy absorption over the entire interval so that they are categorized as the optimal control. The optimal control assumes that the waves over the entire interval are fully known and the control action is already determined before the physical process really happens. Apparently, such an assumption is invalid in the real world. If the control algorithm is to be effective in the real world, it must be applied in a real-time manner. Recently, the model predictive control strategy is widely used to implement the real-time control action. The model predictive control maximizes the power absorption over a future time horizon. By receding the time horizon forward step by step, the control action is applied in a real-time manner. Since the power absorption is maximized over the receding horizon rather than the entire time interval, the model predictive control belongs to the sub-optimal control. Son and Yeung [49] optimized the energy extraction of a dual coaxial-cylinder WEC with the model predictive control strategy. The damping coefficient of the PTO system was adjusted in a real-time manner to maximize the power absorption. Li et al. [50] implemented the dynamic programming for optimal control theory to realize a real-time control action. Their control algorithm was also based on the model predictive control. The model predictive control possesses some favorable features to enable itself a prospective solution to the enhancement of power absorption. Firstly, the control efficiency is sufficient high although it belongs to the sub-optimal control family. It was shown in Hals et al. [42] and Hals et al. [51] that the control strategy allows the WEC to produces power close to the theoretical limits. Another advantage is that it is able to consider constraints on the system forces and limitations in system velocity and position in the context of current future desired velocity or position. Cretel et al. [52] applied the model predictive control to a point-absorber WEC with consideration of constraints on

motion amplitude. Brekken [53] set limitations on PTO force and WEC velocity in the application of the model predictive control.

2.4. Short-term wave prediction

The main challenge in the practical application of the real-time control is that the conditions for optimal energy absorption can be realized only if future incident wave forces are known [54, 55]. Therefore, the short-term wave force prediction is essential in the application of real-time control. Although it is able to predict the waves by meteorological observation [56-58], it is normally complex and requires large amounts of meteorological as well as oceanographic data. It is probably smarter to predict the waves by observing themselves. The wave observation method can be briefly classified into two categories. The first group is the spatial prediction, which forecasts the wave information at a certain point based on the observations at nearby locations. This type of approach can be effectively applied in the WEC array as each device operates as an observation station. Belmont et al. [59] forecasted the waves with the deterministic sea-wave prediction method. The technique first measures the shape of the sea surface around the site concerned and then uses the measurement to build a model capable of estimating the shape of the sea surface when it propagates to the prediction site. The spatial approach is usually complex due to the presence of radiation/diffraction waves as well as wave evolution during the propagation process, especially in the nearshore region or in a harbor. The second group forecasts sea waves with the collection of past wave information right at the site concerned and thereby no other observations are required. This approach is by nature a random signal processing technology and may require the dynamic model of the random process. Consequently, it is applicable to the prediction of many variables, such as wave elevation, wave force, floater velocity, etc. Fusco and Ringwood [60] came up with a linear autoregressive model, which implicitly considered the cyclical behavior of waves. Ge and Kerrigan [61] predicted the wave elevations using autoregressive moving average model. Halliday et al. [62] utilized the fast Fourier transformation to predict the random sea waves. A wave prediction model based on the grey model was developed by Truong and Ahn [63].

Most recently, the artificial intelligence technology is introduced to the prediction problem. Unlike the above deterministic forecasting approach (the forecasting model must be specified by the user), the artificial intelligence method is a data-driven prediction approach. It learns to predict the wave forces itself because even the user has no idea of the details of the forecasting model. Among various artificial prediction models (Bayesian network, decision tree and support vector machines, etc.), the neural network is the most commonly used. Computations are structured in terms of an interconnected layer of artificial neurons, processing information using a connectionist approach to computation. Deo and Naidu [64] developed a neural network to perform real-time wave heights prediction. The prediction was based on the observation of waves at the site concerned so that it was the local observation approach. Oh and Suh [65] incorporated the empirical orthogonal function and the wavelet analysis of the neural network. The hybrid model learned to approximate the inherent relation between wave elevation at the site concerned and elevations at surrounding stations from the training examples. Therefore, their hybrid model belongs to the spatial prediction group. Similar prediction approach was adopted by Agrawal and Deo [66] and Mandal and Prabaharan [67]. The essential work in neural network prediction is the machine learning algorithm, namely how the neural network learns from the training data and makes the prediction. Popular learning algorithms are the gradient descent method, the Newton's method, and the Levenberg-Marquardt method.

2.5. Multi-stable mechanism

The non-linear behaviour of WEC could also be utilized to increase energy absorption. The feature of a non-linear energy capture system can be represented by the stability mechanism. A linear system is monostable whereas a non-linear system is multi-stable. Multi-stable systems are characteristic of a non-linear snap-through mechanism. For example, a bistable system has a double-well potential with a single unstable equilibrium position and two stable equilibrium positions. Accordingly, two types of responses exit. The first one is local movement within a single potential well. The second is oscillation around the two wells, either chaotic or periodic. The stability mechanism was firstly studied in the realm of vibration energy [68]. Panigrahi et al. [69] measured the twinkling energy with non-linear snap-through structures

experimentally. Baglio et al. [70] presented a non-linear device for vibrational energy harvesting, which took the advantage of snap-through buckling. Cottone et al. [71] and Arrieta et al. [72] used the multi-stable system to investigate the broadband energy harvesting. In their work, the frequency bandwidths were broadened several times. Godoy and Trindade [73] optimized a nonlinear vibration absorber based on the snap-through. Zhou et al. [74] took the advantage of snap-through mechanism to improve the efficiency of random energy harvesting. It is recently that multi-stable mechanism is introduced to ocean wave energy harvesting. Younesian and Alam [25] proposed a multi-stable energy capture system, which was composed of two springs and two sliders. Zhang et al. [75] proposed an adaptive bistable power capture mechanism (composed of springs and sliders) for a point absorber WEC. They showed that this novel mechanism can both increase the frequency bandwidth and improve power capture. Xiao et al. [27] utilized the magnets to achieve the bistable mechanism of a non-linear PTO system.

3. Hydrodynamic Model of the WEC

3.1. Introduction

Despite various types of WECs, this thesis only considers a heaving point-absorber. A heaving point-absorber produces electrical energy by converting the kinetic energy of the floater so that a dynamic model should be developed to simulate the wave-structure interaction. Early studies on WEC usually used an analytical approach, which was based on frequency-domain analysis and only applicable in monochromatic waves. The progress in computation capacity boosts the application of the numerical method. Popular numerical methods are the CFD technique and the impulse response model based on the potential flow theory. The CFD technique is powerful at describing the details of the wave-structure interaction, e.g. the vortex and the non-linear wave excitation forces. Bharath et al. [76] predict the performance of a spherical WEC using the Reynolds averaged Navier-Stokes (RANS) model. They investigated the breaking waves in extreme sea state and showed that the wave excitation force did not vary linearly with wave amplitude. If the focus is on the global performance (motions, power output, etc), the impulse response theory is preferred. Since the impulse response theory gives a deterministic dynamic model, it is more welcomed in wave energy control. The impulse response theory is based on the frequency-domain hydrodynamic coefficients (added mass, radiation damping and excitation force transfer function) and represents the radiation wave force with a convolution term. Therefore, it is also known as an indirect time-domain method.

This chapter develops the hydrodynamic model of the point-absorber. Firstly, a boundary element method will be developed to acquire the velocity potentials of radiation/diffraction waves. The boundary element method is based on the Rankine Green function. With the acquired velocity potentials, the frequency-domain hydrodynamic coefficients of the point-absorber are obtained. Subsequently, a state-space model will be developed to represent the dynamics of the point-absorber in time-domain. The state-space representation is a mathematical model of a dynamic system as a set of input, output and state variables related by first-order differential equations.

3.2. The heaving point-absorber WEC

The heaving point-absorber WEC considered in this thesis is shown in Figure 3-1. The submerged part of the floater is a hemisphere with a radius of 5 m. The floater is rigidly connected to the PTO system fixed at the seabed. Only heave motion of the floater is allowed. A right-handed coordinate system fixed to the earth is used. The center of the coordinate system is fixed at the mean sea surface. *Z* axial is positive upward. *X* axial is along the propagation direction of the sea waves.

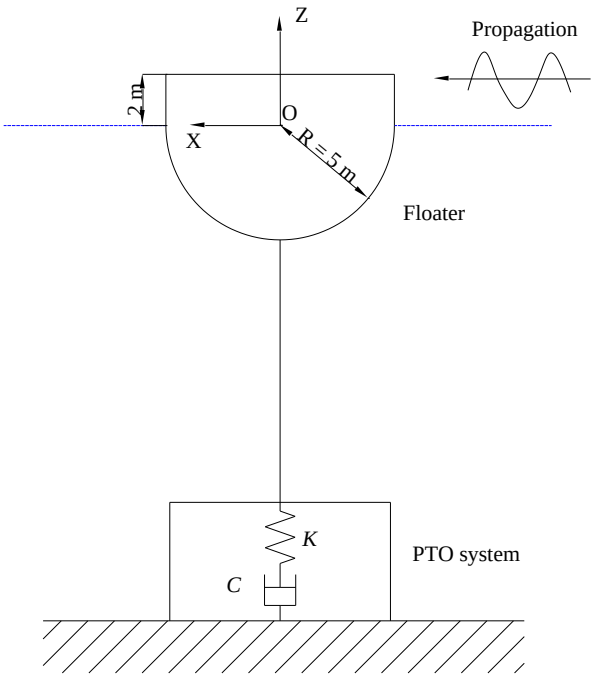

Figure 3-1 The heaving point-absorber concerned.

A linear direct drive generator is adopted to produce power by extracting kinetic energy from the floater. The Lorentz force acting on a moving point charge q with velocity $\boldsymbol{v}$ in magnetic field $\boldsymbol{B}$ is given by $q\boldsymbol{v}\times\boldsymbol{B}$, which can be regarded as a damping force. Also, the mechanical facilities will also provide the restoring stiffness. Therefore, the PTO system is numerically represented by a damper-spring system, with damping coefficient C and stiffness K, which is a reasonable simplification of the permanent-magnet linear generator [77]. According to Vicente et al. [78], the stiffness of a PTO system is typically around ten percent of the hydrostatic coefficient so that $K = 0.1\rho g\pi R^2$ is adopted. Figure 3-2 illustrates the sensitivity of the PTO system to the wave frequency ω and the damping coefficient C. Figure 3-2 is run in regular wave

load case with various combinations of ω and C. In each load case, the amplitude of the incident regular wave is 1 m. The development of the hydrodynamic model will be presented in Chapter 3.4 and please refer to Chapter 3.5 for the verification of the hydrodynamic model. As shown, the energy conversion is maximized at $C = 8.14\times10^5$ kg/s and therefore $C = 8.14\times10^5$ kg/s is used hereinafter. The controller regulates the WEC response by locking and releasing the floater alternately following a certain rule. This kind of control is widely known as the latching control. The latching action is represented with a very large but finite damping coefficient c.

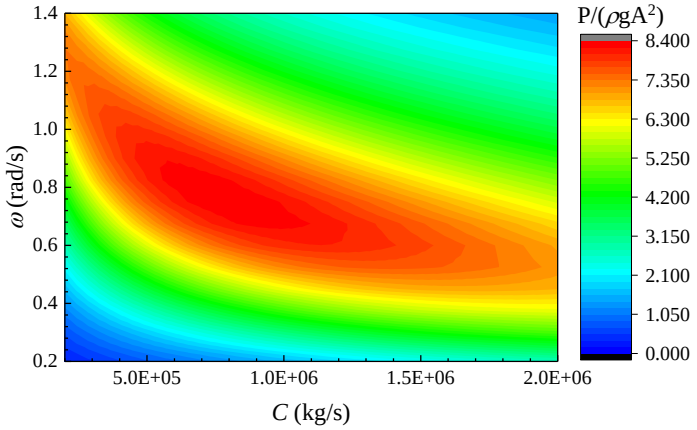

Figure 3-2. Sensitivity of energy absorption to wave frequency and damping coefficient.

3.3. Boundary element method

3.3.1. Boundary value formula

Assuming the flow field is ideal, linear potential flow theory is applied to derive the hydrodynamic coefficients of the point-absorber. The flow within the fluid domain is described by velocity potential $\Phi(\boldsymbol{r}, t)$ in which $\boldsymbol{r} = (x, y, z)$ denotes the position of the point concerned. $\Phi(\boldsymbol{r}, t)$ satisfies the Laplace equation in the whole fluid domain. Consequently, the calculation of $\Phi(\boldsymbol{r}, t)$ is converted to the boundary value problem. Figure 3-3 shows the boundary of the fluid domain. The lateral length is 30 m whereas the length along the wave direction is dependent on the wave length. Generally, the longitudinal size is two times of the wave length. For very long waves (the wave frequency is very low), the length is somewhat smaller.

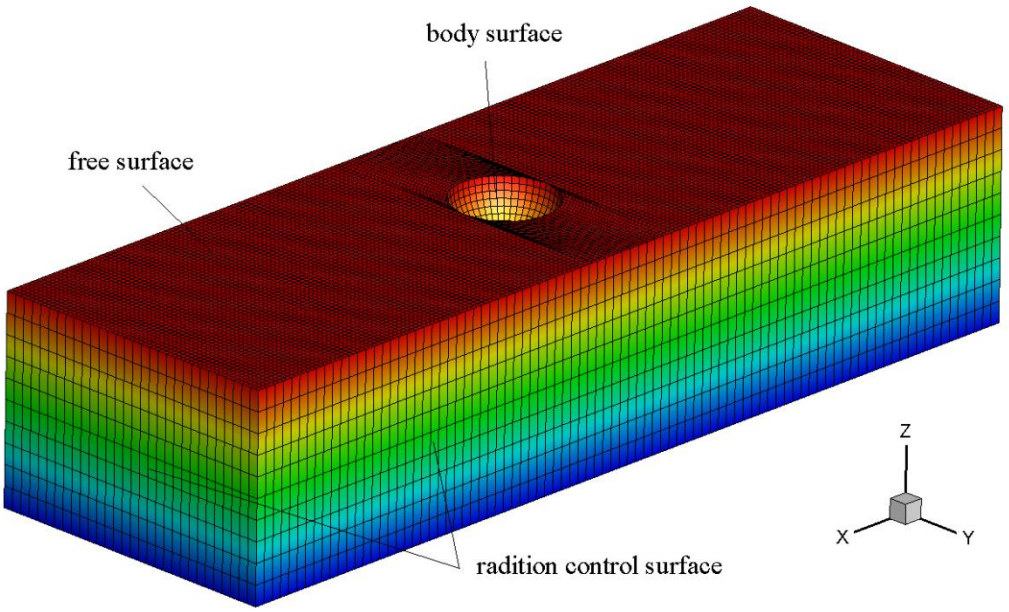

Figure 3-3. Fluid boundary condition.

According to the linear potential flow theory, the entire velocity potential can be separated into three components: the incident wave potential, the radiation wave potential and the diffraction wave potential:

$$\begin{aligned}\Phi(\boldsymbol{r},t) &= \mathrm{Re}\left[\varphi \cdot e^{-i\omega t}\right] \\ &= \mathrm{Re}\left[A\varphi_I \cdot e^{-i\omega t}\right] + \mathrm{Re}\left[A\varphi_D \cdot e^{-i\omega t}\right] + \mathrm{Re}\left[\sum_{i=1}^{6} \xi_i \varphi_i \cdot e^{-i\omega t}\right]\end{aligned} \tag{3.1}$$

where ω is the angular frequency of the incident wave; A is the amplitude of the incident wave; φ_D is the spatial diffraction wave potential; φ_i (i = 1,2,…,6) are the spatial radiation potential in six degrees of freedom and ξ_i are the corresponding motion amplitudes (ξ_1, surge; ξ_2, sway; ξ_3, heave; ξ_4, roll; ξ_5, pitch; ξ_6, yaw). Since the point-absorber is allowed to oscillated up and down, only φ_3 is considered in this thesis. φ_I is the spatial potential of the incident wave

$$\varphi_I(\boldsymbol{r}) = \frac{g}{i\omega} \cdot \frac{\cosh(kz+kh)}{\cosh(kh)} \cdot e^{ik(x\cos\vartheta + y\sin\vartheta)} \tag{3.2}$$

where ϑ is the incident wave angle, which is set to 180° representing the head waves.

The boundary value formula of the diffraction wave potential φ_D is given by

$$\begin{aligned}
&\nabla^2\varphi_D = 0, \textit{in the fluid domain} \\
&g\frac{\partial\varphi_D}{\partial z} - \omega^2\varphi_D = 0, \textit{on steady free water surface} \\
&\frac{\partial\varphi_D}{\partial \boldsymbol{n}} = -\frac{\partial\varphi_I}{\partial \boldsymbol{n}}, \textit{on mean wetted surface of WEC} \\
&\frac{\partial\varphi_D}{\partial \boldsymbol{n}} - ik\varphi_D = 0, \textit{on radiation control surface} \\
&\frac{\partial\varphi_D}{\partial z} = 0, \textit{on sea bed}
\end{aligned} \tag{3.3}$$

The boundary value formula of the radiation wave potential φ_i is given by

$$\begin{aligned}
&\nabla^2\varphi_i = 0, \textit{in the fluid domain} \\
&g\frac{\partial\varphi_i}{\partial z} - \omega^2\varphi_i = 0, \textit{on steady free water surface} \\
&\frac{\partial\varphi_S}{\partial \boldsymbol{n}} = -i\omega n_i, \textit{on mean wetted surface} \quad , i = 1,2,\ldots,6 \\
&\frac{\partial\varphi_i}{\partial \boldsymbol{n}} - ik\varphi_i = 0, \textit{on radiation control surface} \\
&\frac{\partial\varphi_i}{\partial z} = 0, \textit{on sea bed}
\end{aligned} \tag{3.4}$$

where n_i is generalized normal vector

$$n_i = \begin{cases} \boldsymbol{n} & i = 1,2,3 \\ \boldsymbol{m}\times\boldsymbol{n} & i = 4,5,6 \end{cases} \tag{3.5}$$

$\boldsymbol{m}$ is the vector from the point concerned to the CoG (centre of gravity) of the buoy. In this thesis, CoG = (0 m,0 m, -2 m) is used. and $\boldsymbol{n} = (n_1, n_2, n_3)$ is the unit normal vector directed inward on the body surface; k is the wave number determined by the dispersion relation

$$k\cdot\tanh kH = \frac{\omega^2}{\mathrm{g}} \tag{3.6}$$

where H is the water depth.

Assuming that the velocity potential has been acquired, the wave force transfer function ψ, the added mass μ, and the potential damping λ are given by

$$\psi_j(\omega) = -\rho i\omega \iint_s (\varphi_S + \varphi_I) n_j dS,\ j = 1,2,...6 \tag{3.7}$$

$$\mu_{ij}(\omega) = \mathrm{Im}\left[-\frac{\rho}{\omega} \iint_S \varphi_j n_i dS \right], i,\ j = 1,2,...,6 \tag{3.8}$$

$$\lambda_{ij}(\omega) = \mathrm{Re}\left[-\rho \iint_S \varphi_j n_i dS \right], i,\ j = 1,2,...,6 \tag{3.9}$$

3.3.2. 3-D Rankine source panel method

By distributing sources on the entire boundary of the fluid domain, the velocity potential $\varphi(\boldsymbol{r})$ at point $\boldsymbol{r}$ = (x, y, z) within the fluid domain can be represented by Eq. (3.10).

$$\varphi(\boldsymbol{r}) = \iint_s G(\boldsymbol{r}, \boldsymbol{\varsigma}) \cdot \sigma(\boldsymbol{\varsigma}) dS \tag{3.10}$$

where $\sigma(\boldsymbol{\varsigma})$ is the source strength at point $\boldsymbol{\varsigma}$ = (ς_1, ς_2, ς_3) on the boundary of the fluid domain. $G(\boldsymbol{r}, \boldsymbol{\varsigma})$ is the Green function.

Eq. (3.10) is an analytical integral formula and should be represented by a discretized approach in the numerical calculation. Generally, the boundary element method can be grouped based on the discretization of the boundary surface. This can be done in many ways, ranging from a very simple flat panels and constant sources on each panel to a high-order approximation where the sources are not uniformly distributed. For example, the shape of the panel can be described by the NURBS-based panel. Although the high-order method is able to model the buoy shape and the source distribution more accurately, the Green function in the high-order method is very complex and produces a large number of variables assigned to each element. Therefore, this thesis adopts the constant panel method to discretize the boundary integral. In the constant panel method, the panel is flat and the sources are uniformly distributed across the panel.

After the boundary integral has been discretized, a source type (or Green function) should be selected. In this thesis, the Rankine source is adopted which is associated with a simple Green function

$$G(\boldsymbol{r},\boldsymbol{\varsigma}) = \frac{1}{\sqrt{(x-\varsigma_1)^2+(y-\varsigma_2)^2+(z-\varsigma_3)^2}} \tag{3.11}$$

The application of the Rankine source inherently implies that the sources must be distributed on the entire fluid boundary (wetted buoy surface, free water surface, radiation control surface, seabed). It is worth noting that the sources may just need to be distributed on partial fluid boundary if an alternative source is used.

By dividing the whole boundary into N panels and distributing the Rankine source on the element uniformly, analytical formula Eq. (3.10) can be expressed in an integral way

$$\varphi(\boldsymbol{r}) = \sum_{j=1}^{N} G_{ij}(\boldsymbol{r},\boldsymbol{\varsigma}_j)\cdot\sigma(\boldsymbol{\varsigma}_j) \tag{3.12}$$

$\sigma(\varsigma_j)$ is the source strength assigned to element j. G_{ij} is named as the influence matrix with dimension $N \times N$, which represents the velocity potential at point $\boldsymbol{r} = (x, y, z)$ induced by element j. A brief interpretation of the Rankine source method is presented in Appendix A, and please refer to Hess and Smith [79] for the details.

3.4. State-space representation

According to the impulse response theory [38], the time-domain motion equation of the heaving point-absorber in stochastic waves is given by

$$(M+m)\ddot{z}(t) = F_{wave}(t) - \int_0^t h(t-\tau)\dot{z}(\tau)d\tau - (C+\beta(t)c)\dot{z}(t) - (K+\rho g\pi R^2)z(t) \tag{3.13}$$

where M ($M = 2/3\rho\pi R^3$) is the mass of the floater and m is the added mass of heave mode at infinite frequency. z, $\dot{z}$ and $\ddot{z}$ are the displacement, the velocity and the acceleration. $\beta(t)$ is the binary control command. When $\beta = 1$, the latching control is

applied; when $\beta = 0$, it is not. Applying the latching control, the PTO system switches abruptly between two states ($\beta = 0,1$) so that it is a bang-bang control. h is the so-called retardation kernel function which represents the memory effect of the free surface. It can be obtained either from the added mass $\mu(\omega)$ or the potential damping $\lambda(\omega)$

$$h(t) = \frac{2}{\pi}\int_0^\infty \frac{\mu_{33}(\omega)}{\omega}\sin(\omega t)d\omega = \frac{2}{\pi}\int_0^\infty \lambda_{33}(\omega)\cos(\omega t)d\omega \tag{3.14}$$

A linear wave model is adopted to generate the stochastic wave elevations, which consists of a set of regular waves with different oscillating frequencies and phases

$$\begin{aligned} \zeta(t) &= \mathrm{Re}\left[\sum_{j=1}^{N} A_j e^{i(\omega_j t+\varepsilon_j)}\right] \\ A_j &= \sqrt{2S(\omega_j)\Delta\omega} \end{aligned} \tag{3.15}$$

where A_j, ω_j, and ε_j are the wave amplitude, the frequency and the random phase of the regular wave component j. $S(\omega)$ is the wave spectrum. If ω_j is uniformly distributed over the wave frequency range, the stochastic wave elevations will start to repeat after a certain duration [36]. To address this issue, the correction technique in Li et al. [80] is adopted here. The wave frequency range is firstly uniformly divided into N segments and ω_j is randomly distributed within segment j (see Figure 3-4).

Figure 3-4 Distribution of wave seeds.

The wave excitation force F_{wave} is estimated by the linear transform function ψ

$$F_{wave}(t) = \mathrm{Re}\left[\sum_{j=1}^{N} \psi_3(\omega_j) A_j e^{i(\omega_j t+\varepsilon_j)}\right] \tag{3.16}$$

Eq. (3.13) is widely used in the seakeeping problem to simulate the dynamics of a floating body. However, it is inconvenient to incorporate the real-time control strategy using Eq. (3.13) and thereby a state-space model is used to represent the point-absorber dynamics. Denote a system with input $x(t)$ and output $y(t)$, the following approaches are available to describe the dynamic process

$$\frac{d^n y}{dt^n} + q_{n-1}\frac{d^{n-1} y}{dt^{n-1}} + \ldots + q_1\frac{dy}{dt} + q_0 y = p_{n-1}\frac{d^{n-1} x}{dt^{n-1}} + p_{n-2}\frac{d^{n-2} x}{dt^{n-2}} + \ldots + p_1\frac{dx}{dt} + p_0 x \quad (3.17)$$

$$y(t) = \int_0^t h(t-\tau)x(\tau)d\tau \quad (3.18)$$

$$\begin{aligned} \dot{\boldsymbol{u}}(t) &= \vec{\boldsymbol{A}} \cdot \boldsymbol{u}(t) + \vec{\boldsymbol{B}} x(t) \\ y(t) &= \vec{\boldsymbol{C}} \cdot \boldsymbol{u}(t) \end{aligned} \quad (3.19)$$

Eq. (3.17) is the ordinary differential equation with order n. Eq. (3.18) is the convolution integral. Eq. (3.19) is the state-space representation, in which $\boldsymbol{u}(t)$ is the state vector with dimension $n\times 1$. $\vec{\boldsymbol{A}}$, $\vec{\boldsymbol{B}}$ and $\vec{\boldsymbol{C}}$ are the system matrix, the state matrix and the output matrix, with dimension $n\times n$, $n\times 1$ and $1\times n$. Please note that the radiation force follows Eq. (3.18) so that one can use the state-space model to represent it.

Combining Eq. (3.17) and Eq. (3.19), one gets

$$\begin{aligned} \vec{\boldsymbol{A}} &= \begin{bmatrix} -q_{n-1} & -q_{n-1} & \cdots & -q_1 & -q_0 \\ 1 & 0 & \cdots & 0 & 0 \\ 0 & 1 & \cdots & 0 & 0 \\ \vdots & \vdots & \ddots & 0 & 0 \\ 0 & 0 & \cdots & 1 & 0 \end{bmatrix}, \vec{\boldsymbol{B}} = \begin{bmatrix} 1 \\ 0 \\ 0 \\ \vdots \\ 0 \end{bmatrix} \\ \vec{\boldsymbol{C}} &= \begin{bmatrix} p_{n-1} & p_{n-2} & \cdots & p_1 & p_0 \end{bmatrix} \end{aligned} \quad (3.20)$$

Combing Eq. (3.18) and Eq. (3.19), one gets

$$h(t) = \vec{\boldsymbol{C}} e^{\vec{\boldsymbol{A}}t} \vec{\boldsymbol{B}} \quad (3.21)$$

Taking the Laplace transform of Eq. (3.17), one gets

$$h(s)=\frac{Y(s)}{U(s)}=\frac{p_{n-1}s^{n-1}+p_{n-2}s^{n-2}+\cdots+p_1+p_0}{s^n+q_{n-1}s^{n-1}+\cdots+q_1+q_0} \tag{3.22}$$

Eq. (3.18) is the time-domain expression of retardation kernel function, and it can be transformed to the frequency-domain through the Fourier transformation

$$h(i\omega)=\int_0^\infty h(\tau)e^{-i\omega\tau}dt\tau=\lambda_{33}(\omega)+i\omega\left[\mu_{33}(\omega)-m\right] \tag{3.23}$$

Eq. (3.21) and Eq. (3.22) are correlated through the Fourier transformation

$$\tilde{F}\left\{h(t)\right\}=h(s)\big|_{s=i\omega}=h(i\omega) \tag{3.24}$$

According to Eq. (3.24)

$$\frac{p_{n-1}(i\omega)^{n-1}+p_{n-2}(i\omega)^{n-2}+\ldots+p_1+p_0}{(i\omega)^n+q_{n-1}(i\omega)^{n-1}+\ldots+q_1+q_0}=\lambda_{33}(\omega)+i\omega\left[\mu_{33}(\omega)-m\right] \tag{3.25}$$

so that

$$\begin{aligned}\lambda_{33}(\omega)&=\mathrm{Re}\left\{\frac{p_{n-1}(i\omega)^{n-1}+p_{n-2}(i\omega)^{n-2}+\ldots+p_1+p_0}{(i\omega)^n+q_{n-1}(i\omega)^{n-1}+\ldots+q_1+q_0}\right\}\\ \mu_{33}(\omega)&=\mathrm{Im}\left\{\frac{1}{\omega}\cdot\frac{p_{n-1}(i\omega)^{n-1}+p_{n-2}(i\omega)^{n-2}+\ldots+p_1+p_0}{(i\omega)^n+q_{n-1}(i\omega)^{n-1}+\ldots+q_1+q_0}\right\}+m\end{aligned} \tag{3.26}$$

Parameters $\boldsymbol{p}$ and $\boldsymbol{q}$ can be estimated by the least square method. The calculation of $\vec{\boldsymbol{A}}$, $\vec{\boldsymbol{B}}$ and $\vec{\boldsymbol{C}}$ is also called system identification. By using the state-space representation, Eq. (3.13) can be re-written as

$$\begin{aligned}&\left(M+m\right)\ddot{z}=F_{wave}-\vec{\boldsymbol{C}}\boldsymbol{u}-\rho g\pi R^2 z-\left(C+\beta c\right)\dot{z}-Kz\\ &\dot{\boldsymbol{u}}=\vec{\boldsymbol{A}}\boldsymbol{u}+\vec{\boldsymbol{B}}\dot{z}\end{aligned} \tag{3.27}$$

Define a state vector $\boldsymbol{x}=[\,z,\dot{z},\boldsymbol{u}^T]^T$ with dimension (n+2)×1. Then Eq. (3.27) is expressed as

$$\dot{\boldsymbol{x}} = \boldsymbol{\gamma} \cdot \boldsymbol{x} + \boldsymbol{\eta}$$

$$\boldsymbol{\gamma} = \begin{bmatrix} 0 & 1 & \mathbf{0} \\ -\dfrac{\rho g \pi R^2 + K}{M+m} & -\dfrac{C+\beta c}{M+m} & -\dfrac{\vec{\boldsymbol{C}}}{M+m} \\ \mathbf{0} & \vec{\boldsymbol{B}} & \vec{\boldsymbol{A}} \end{bmatrix}, \boldsymbol{\eta} = \begin{bmatrix} 0 \\ \dfrac{F_{wave}}{M+m} \\ \mathbf{0} \end{bmatrix} \tag{3.28}$$

Eq. (3.28) is a first-order differential equation, and it is solved by the 4-th order Rongue-Kutta method with the initial condition $\boldsymbol{x}(0) = \mathbf{0}$. Then, the average power capture is given by

$$P = \frac{1}{T}\int_0^T C \cdot \dot{z}(t,\beta)^2 dt \tag{3.29}$$

3.5. Verification

3.5.1. System identification

As shown above, the hydrodynamic model is based on the system identification. To ensure that the state matrices obtained by the system identification are reliable, the original hydrodynamic coefficients and those estimated by the state matrices (estimated by Eq. (3.26)) are compared in Figure 3-5, where the order of the system is selected as n = 5. The red dot represents the original hydrodynamic coefficients obtained by the boundary element analysis and the black curve stand for the hydrodynamic coefficients estimated by the system identification (Eq. (3.26)). As shown, a 5th-order state-space model can approximate the convolution term efficiently. The good approximation manifests that the parameters used in the state-space representation are reliable.

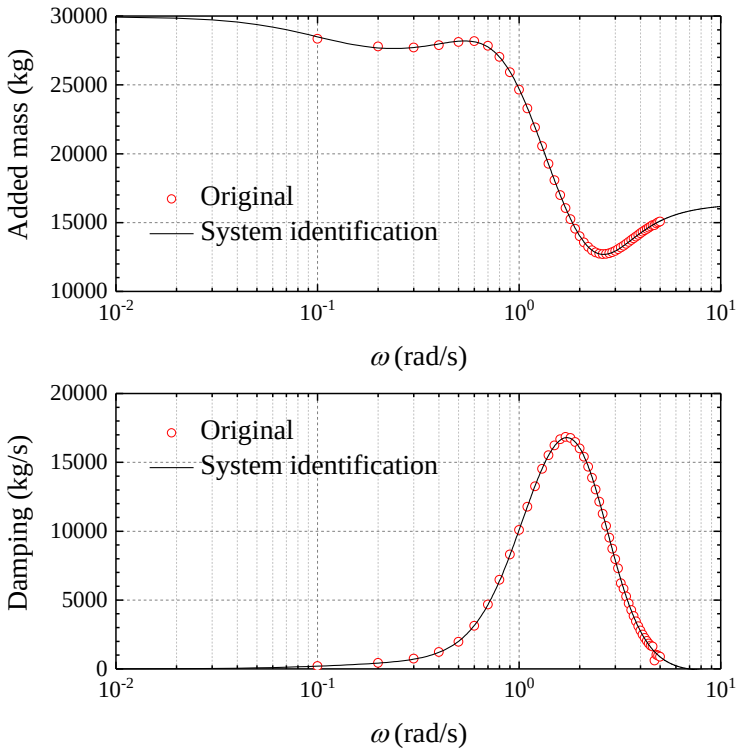

Figure 3-5 System identification results.

3.5.2. State-space representation

The state-space model is verified against frequency-domain hydrodynamic analysis programme Wadam [81] under a set of unit regular waves with various periods. The PTO system is modeled by adding an additional damping ($C = 8.14\times10^5$ kg/s) and an additional stiffness ($K = 0.1\rho g\pi R^2$) in Wadam. Please note that the point-absorber is a linear system without the latching control so that Wadam is applicable here. The displacement of the heaving point-absorber in regular waves with a set of frequencies are simulated with the present hydrodynamic model and the Wadam, respectively. In each load case, the amplitude of incident wave is set to 1 m. The displacements of the point-absorber in regular waves obtained by the two simulation tools are compared in Figure 3-6. As shown, the agreement between the two simulation tools is very good.

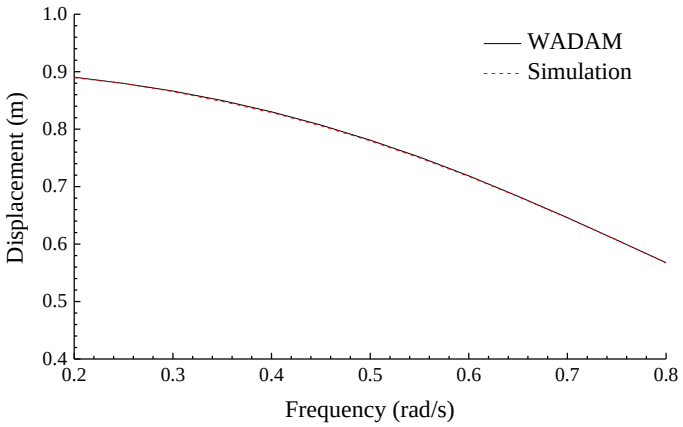

Figure 3-6. Floater motions in regular waves.

The state-space model is also validated against experimental measurement. It is a pity that the test data of the point-absorber used in this thesis are not available and thereby the experimental data of a cone-cylinder WEC measured by Vantorre et al. [82] here. The model testing was conducted in a wave flume of 70 m length and 4 m width. All the data were recorded at a water depth of 1.0 m. The configuration of the WEC is illustrated in Figure 3-7. As shown, the test model was also a heaving oscillating-buoy WEC. The floater was a cone-cylinder with a top angle of 90°. The radius was 0.155 m and the draft was 0.218 m. In the test, the PTO system was merely represented with a linear damper. Figure 3-8 shows the panel model of the cone-cylinder.

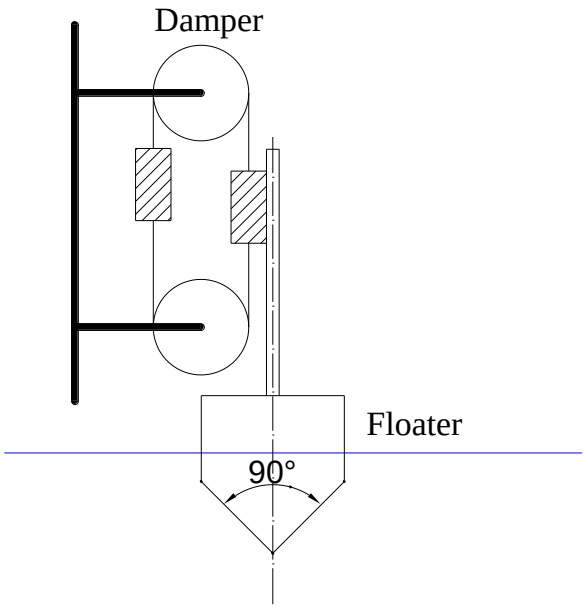

Figure 3-7 Configuration of the WEC in Vantorre et al. [82].

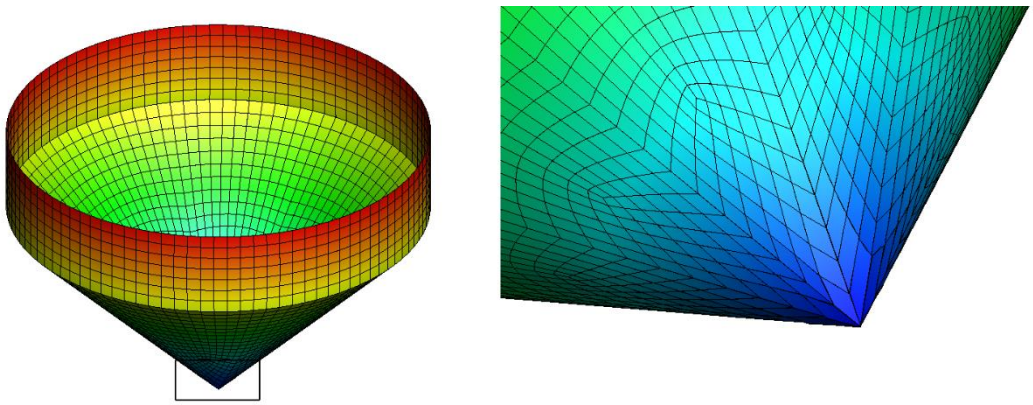

Figure 3-8 Panel model of the WEC in Vantorre et al. [82].

Figure 3-9 compares the motions of the cone-cylinder in regular wave (A = 0.045 m, T = 1.5 s) measured in the model test and predicted by the present hydrodynamic analysis approach. In general, the agreement between experimental data and simulation results are good although the motion amplitude predicted by the simulation tool is slightly larger. In the experimental condition, the viscous behavior of the wave flow was not eligible considering the small size of the floater. The hydrodynamics is addressed within the framework of potential flow theory inherently implying that no viscous damping was considered. Consequently, the simulation tool will give a larger response.

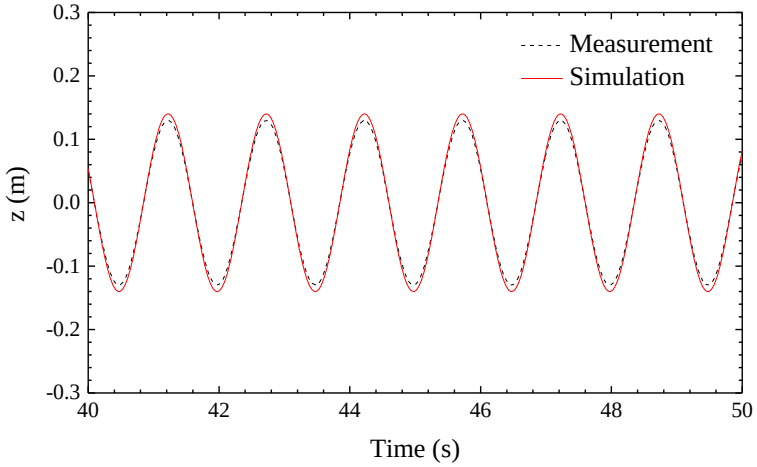

Figure 3-9 Floater motion in regular waves. (A = 0.045 m, T = 1.5 s, C = 21.43 kg/s)

3.6. Summary

This chapter develops the state-space representation of the WEC dynamics, which is a first-order differential equation system. Compared with the traditional seakeeping

time-domain motion equation based on convolution integral term, the state-space representation increases the computation speed dramatically. Moreover, the representation of dynamics based on differential makes it easier to implement the control algorithm, which is aimed at maximizing the energy absorption (This will be clarified in Chapter 4).

The system identification is based on the frequency-domain hydrodynamic coefficients. A boundary element method, based on Rankine Green function, is developed to address the wave-structure interactions within the framework of linear potential flow theory. Viscous and non-linear effects are not considered in the boundary element method. By handling the calculation of velocity potential as a boundary value problem, the strengths of the Rankine sources distributed on the fluid boundary are determined and thereby the hydrodynamic coefficients are available.

4. Real-time Control Algorithm

4.1. Introduction

An oscillating-buoy wave energy converter produces power by converting the kinetic energy of the floater. As demonstrated in previous studies [83], the energy harvesting efficiency of an oscillating-buoy WEC is strongly dependent on the frequency of the incident waves. The energy absorption is maximized when the resonant frequency of the WEC coincides with the wave oscillating frequency. The energy absorption drops significantly when the wave oscillating frequency shifts away from the resonant frequency. Therefore, the efficiency of oscillating-buoy WEC is usually unsatisfactory in the random sea waves.

The active control is introduced to maximize the energy absorption by regulating the dynamic response of an oscillating-buoy WEC in random waves. Among various control algorithms, one control strategy is aimed at tuning the phase of the WEC and making it in phase with the wave excitation forces. In this circumstance, the kinetic energy will not be dissipated by the wave forces. This kind of control strategy is known as the phase control. Many ways are available to tune the phase, one of which is to lock the WEC at some time instants. It is the latching control. Latching control was first proposed by Budal and Falnes [44]. They tuned the velocity phase by locking and releasing the WEC alternately. They pointed out that the energy absorption is maximized on condition that the velocity is in phase with the wave excitation forces.

Wave energy control is by nature an optimization problem, and it is mostly examined scientifically and hardly applied in practice. If the future long-term wave forces are fully known, the control is optimal and such control is called the optimal control. For example, Budal and Falnes [44] assumed that the wave forces were fully known, and they derived the control command before the wave-structure interaction really happened. The same assumption is seen in many researcher's works [40, 43, 45].

However, it is very difficult to fully know the long-term future wave forces in the real world. Although one can predict long-term wave forces with certain engineering tools, the uncertainty may be very significant. Therefore, the optimal control is not

applicable in practice. To solve this problem, this chapter will develop a real-time latching control algorithm. The control algorithm is based on the model predictive control, which maximizes the energy absorption over a time-horizon rather than the entire simulation interval. Since the energy extraction is maximized over the 'time-horizon', only short-term future wave forces in the next few seconds are required. The short-term future wave forces are predictable and thereby the model predictive control is applicable in the practice. It is temporarily assumed in this chapter that the wave forces over the time-horizon are known. Chapter 5 will illustrate how the wave forces are predicted in this thesis.

4.2. Optimal command theory

Assume that the wave forces during the interval [0, T] are already known, the objective of the latching control is to maximize the average energy absorption through the binary control command $\beta(t)$

$$\max P = \frac{1}{T}\int_0^T C \cdot \dot{z}(t,\beta)^2 dt \tag{4.1}$$

From a mathematical point of view, it is required to find the maximum of P subject to constraint Eq. (3.13) or Eq. (3.28). Apparently, Eq. (3.13) is not easy to handle with an analytical approach and it is why the state-space representation is developed in this thesis. If the incident wave is regular, the analytical solution is available [45]. Otherwise, the solution is non-causal [54], which means that the current control output depends on the future control input. Regardless of the incident waves, define a Hamiltonian $\hat{H}$:

$$\hat{H} = C\dot{z}^2 + \boldsymbol{\chi}(\boldsymbol{\gamma} \cdot \boldsymbol{x} + \boldsymbol{\eta}) \tag{4.2}$$

$\boldsymbol{\chi}$ is a state vector with dimension 1×(n+2), which can be regarded as the Lagrange multipliers. Combing Eq. (3.28) and Eq. (4.2), the specific expression of the Hamiltonian is given by

$$\hat{H} = C\dot{z}^2 + \chi_1\dot{z} + \chi_2\left[\frac{F_{wave}}{M+m} - \frac{\rho g\pi R^2 + K}{M+m}z - \frac{C+\beta c}{M+m}\dot{z} - \frac{1}{M+m}\sum_{i=1}^{n}C_i u_i\right] + \sum_{i=1}^{n}\left[\chi_{i+2}\left(B_i\dot{z} + \sum_{j=1}^{n}A_{ij}u_j\right)\right] \tag{4.3}$$

According to the Pontryagin's maximum principle, the optimal β is the one maximizing the Hamiltonian at every time step throughout [0, T]. The Hamiltonian is a linear function of β so that β must be the extremal values (0 or 1) in order to maximize the Hamiltonian. It is easy to find that the Hamiltonian reaches the maximum value on condition that

$$\beta = \begin{cases} 1 & \chi_2 c\dot{z} < 0 \\ 0 & otherwise \end{cases} \tag{4.4}$$

Since random waves within the interval [0, T] are already known, the time series of floater movement can be calculated. Subsequently, it is required to calculate χ_2 at each time step and apply the latching control based on the binary sequence. Please note that the Lagrange multipliers satisfy the following relation

$$\begin{aligned} &\dot{\chi}_i = -\frac{\partial H}{\partial x_i}(t, \mathbf{x}, \beta), i = 1, 2, ..., n+2 \\ &\boldsymbol{\chi}(T) = \mathbf{0} \end{aligned} \tag{4.5}$$

According to Eq. (4.3), the Lagrange multipliers are specified as

$$\begin{aligned} &\dot{\chi}_1 = \chi_2\frac{\rho g\pi R^2 + K}{M+m} \\ &\dot{\chi}_2 = -2C\dot{z} - \chi_1 + \chi_2\frac{C+\beta c}{M+m} - \sum_{i=1}^{n}\left(\chi_{i+2}B_i\right) \\ &\dot{\chi}_{i+2} = \frac{\chi_2 C_i}{M+m} - \sum_{j=1}^{n}\left(\chi_{j+2}A_{ji}\right) \\ &\boldsymbol{\chi}(T) = \mathbf{0} \end{aligned} \tag{4.6}$$

Eq. (4.6) cannot be solved numerically like an initial value problem as the final condition is given here. In Li et al. [50], the canonical equations were solved based on

the combination of discretization and dynamic programming. Zhong and Yeung [84] derived the control command with the so-called quadratic programming formulation. In this study, an iterative process is applied to calculate $\boldsymbol{\chi}$. Firstly, run the simulation with $\beta(t) = 0$ to obtain the motions free of latching action by integrating Eq. (3.28) forward from $t = 0$ to $t = T$. Subsequently, determine χ by integrating Eq. (4.6) backwards from $t = T$ to $t = 0$ ($\boldsymbol{\chi}(T) = \mathbf{0}$ is now an initial condition). Based on Eq. (4.4), the control command $\beta(t)$ is deduced. Iterating the process with the determined control command until the results converge, the optimal control command $\beta(t)$ can be derived.

Apparently, the control performance is dominated by the control command $\beta(t)$, which demands the controller whether to lock the floater or not. Babarit and Clement [45] developed an analytical method to estimate the optimal locked duration in regular waves. Their analytical expression is used in this thesis to validate the present control algorithm.

As mentioned before, the WEC switches abruptly between two states (β = 0,1). When the latching action is not applied, the dynamic model of the WEC is given by

$$\begin{aligned} \dot{\boldsymbol{x}} &= \boldsymbol{\gamma} \cdot \boldsymbol{x} + \mathrm{Re}\left[\boldsymbol{\eta} e^{i(\omega t+\varepsilon)}\right] \\ \boldsymbol{\gamma} &= \begin{bmatrix} 0 & 1 & \mathbf{0} \\ -\dfrac{\rho g \pi R^2 + K}{M+m} & -\dfrac{C}{M+m} & -\dfrac{\vec{\boldsymbol{C}}}{M+m} \\ \mathbf{0} & \vec{\boldsymbol{B}} & \vec{\boldsymbol{A}} \end{bmatrix}, \boldsymbol{\eta} = \begin{bmatrix} 0 \\ \dfrac{F_{wave}}{M+m} \\ \mathbf{0} \end{bmatrix} \end{aligned} \tag{4.7}$$

Given an initial condition $\boldsymbol{x}(t_i) = \boldsymbol{x}_i$, the general solution of can be expressed in term of matrix exponentials [45]

$$\boldsymbol{x}(t) = e^{\boldsymbol{\gamma}(t-t_i)}\boldsymbol{x}_i + \mathrm{Re}\left[(\boldsymbol{I} \cdot e^{i\omega(t-t_i)} - e^{\boldsymbol{\gamma}(t-t_i)}) \times (i\omega\boldsymbol{I} - \boldsymbol{\gamma})^{-1}\boldsymbol{\eta} e^{i(\omega t_i+\varepsilon)}\right] \tag{4.8}$$

where is ε the phase of wave excitation force at $t = 0$.

It is now to seek a periodic steady-state solution of the controlled motion. Assume that the velocity of the controller movement vanishes at $t = 0$. As shown in Figure 4-1, apply the latching action during the interval $[0, t_0]$, and then release the WEC and set

it free until instant $t = t_1$. Now, the task is to determine the latched duration t_0, which maximizes the energy absorption.

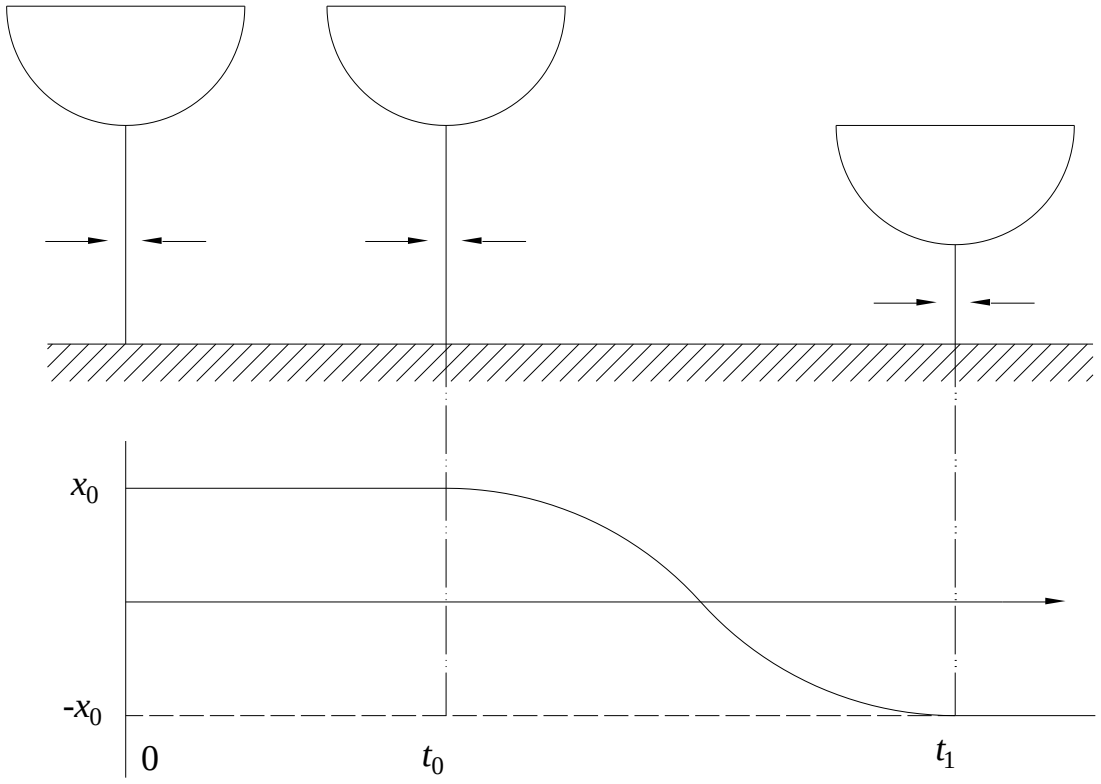

Figure 4-1. Controlled movement.

It is straightforward to know that the controller movement under regular waves is periodic, and thereby the displacement at $t = t_1$ should be equal to the negation of the displacement at $t = 0$

$$\boldsymbol{x}(0) = -\boldsymbol{x}(t_1) \tag{4.9}$$

and the wave excitation force is also equal to its reflection

$$\mathrm{Re}(F_{wave} \cdot e^{i(\omega t_1 + \varepsilon)}) = -\mathrm{Re}(F_{wave} \cdot e^{i\varepsilon}) \tag{4.10}$$

From Eq. (4.10)

$$\begin{aligned} & e^{i\omega t_1} = -1 \\ & t_1 = (k + \frac{1}{2})\frac{2\pi}{\omega}, k \in N \end{aligned} \tag{4.11}$$

It indicates that, under regular waves, the ratio between the period of the controller motion and the wave period must be odd. This thesis investigates the optimal command theory so that $k = 0$, implying that $t = \pi/\omega$

At time instant $t = t_0$,

$$\begin{aligned} \boldsymbol{x}(t_0) &= \boldsymbol{x}_i = e^{\boldsymbol{\gamma}' t_0}\boldsymbol{x}_0 + \mathrm{Re}\left[(\boldsymbol{I}\cdot e^{i\omega t_0} - e^{\boldsymbol{\gamma}' t_0}) \times (i\omega \boldsymbol{I} - \boldsymbol{\gamma}')^{-1}\boldsymbol{\eta}' \right] \\ \boldsymbol{\gamma}' &= \begin{bmatrix} 0 & 1 & \mathbf{0} \\ 0 & 0 & \mathbf{0} \\ \mathbf{0} & \mathbf{0} & \vec{\boldsymbol{A}} \end{bmatrix}, \boldsymbol{\eta}' = \mathbf{0} \end{aligned} \tag{4.12}$$

where $\boldsymbol{x}_0$ is the initial condition at $t = 0$.

At time instant $t = t_1$,

$$\boldsymbol{x}(t_1) = -\boldsymbol{x}_0 = e^{\boldsymbol{\gamma}(t_1 - t_0)}\boldsymbol{x}_i + \mathrm{Re}\left[(\boldsymbol{I}\cdot e^{i\omega(t_1 - t_0)} - e^{\boldsymbol{\gamma}(t_1 - t_0)}) \times (i\omega \boldsymbol{I} - \boldsymbol{\gamma})^{-1}\boldsymbol{\eta} e^{i(\omega t_0 + \varepsilon)} \right] \tag{4.13}$$

Denote $\Delta t = t_1 - t_0$ and combine Eq. (4.12) and Eq. (4.13)

$$\boldsymbol{x}_0 = -(\boldsymbol{I} + e^{\boldsymbol{\gamma}\Delta + \boldsymbol{\gamma}' t_0})^{-1} \times \mathrm{Re}\left\{ \left[(\boldsymbol{I} e^{i\omega\Delta} - e^{\boldsymbol{\gamma}\Delta})(i\omega \boldsymbol{I} - \boldsymbol{\gamma})^{-1}\boldsymbol{\eta} \right] \times e^{i(\omega t_0 + \varepsilon)} \right\} \tag{4.14}$$

Since the latching action is applied over $[0, t_0]$ so that the velocity vanishes during this period. Since $\boldsymbol{x}_0 = [\, z, \dot{z}, \boldsymbol{u}^T]^T$, the latched duration t_0 should satisfy that $\dot{z} = 0$. As demonstrated by Babarit and Clement [45], for any value of ε in $[0, \pi]$, one can compute all the values of t_0 in $[0, \pi/\omega]$ satisfying $\dot{z} = 0$. By repeating this procedure for a set of phase ε, all the couples (ε, t_0) are determined. Afterward, the optimal couple maximizing the energy extraction is selected. Please refer to Babarit and Clement [45] for more details.

Figure 4-2 displays the latched durations obtained with the current simulation tool and Eq. (4.14). Both the two methods suggest that the optimal latched duration increases when the wave frequency shifts to lower values, implying that stronger latching action is needed in the case of long waves.

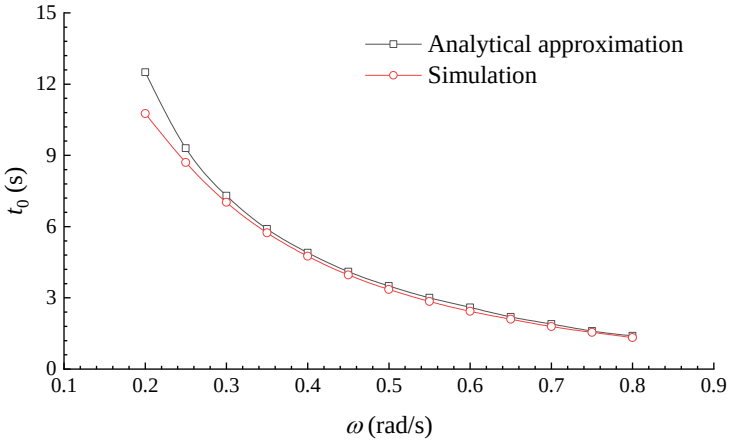

Figure 4-2. Optimal latched durations.

Budal and Falnes [44] found that the energy absorption is maximized when the velocity is in phase with the wave excitation forces. This property is widely accepted as the criterion to validate the latching control. This feature is also adopted to validate the control algorithm. Figure 4-3 plots the times of the wave force and the buoy velocity with optimal latching control in regular wave. The wave amplitude is 1 m and the wave frequency is 0.3 rad/s. As shown in Figure 4-3, the controlled floater velocity is in phase with the wave force. It indicates the control algorithm is reliable.

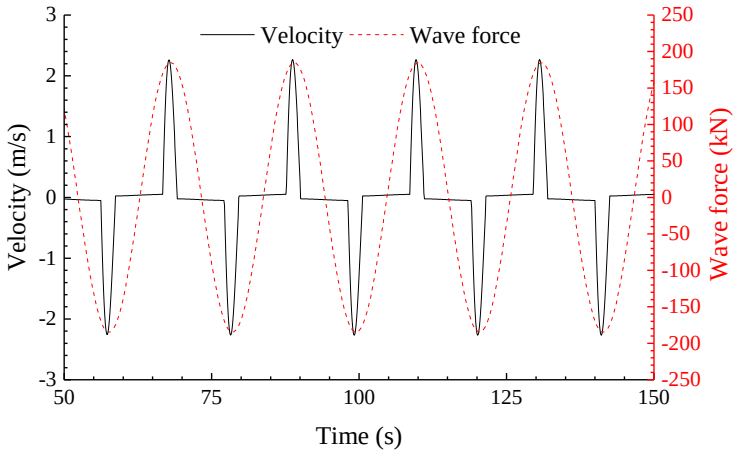

Figure 4-3 The phase between velocity and wave force in regular wave, A= 1 m, ω = 0.3 rad/s.

4.3. Real-time implementation of control

The optimal command theory cannot be applied directly since it is impossible to know the wave forces over the entire interval. One can forecast the short-term wave

forces over a relatively short interval [t, $t+\tau$] so that the optimal command theory can be used within the prediction interval. It is the basic idea of the real-time control strategy in this thesis, which is widely known as the model predictive control or the receding horizon control.

The procedure of the model predictive control is illustrated in Figure 4-4. At time step t_i, predict the wave forces within horizon [t_{i+1}, $t_{i+1}+\tau$] using a prediction model. Then, the control command $\beta(t)$, $t \in [t_{i+1}, t_{i+1}+\tau]$, can be deduced with the optimal command theory. At time step t_{i+1}, apply the control action which has been deduced at the previous step. Please note that only the control command $\beta(t_{i+1})$ is adopted. Repeat the process again to predict the control action at time step t_{i+2}. By repeating this algorithm step by step, the real-time control is implemented throughout the entire interval.

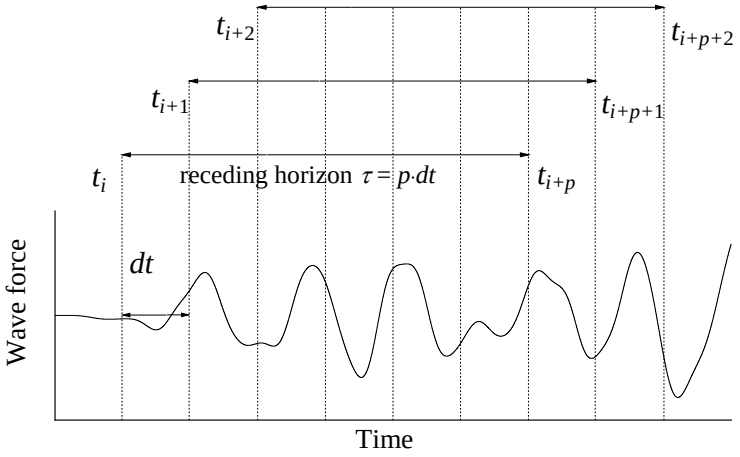

Figure 4-4 Illustration of the receding horizon algorithm.

The model predictive control maximizes the energy absorption over the receding horizon [t_{i+1}, $t_{i+1}+\tau$] rather than the entire interval [0, T], and thereby it is a kind of sub-optimal control. That is to say, the energy absorption obtained with application of the model predictive control is lower than the theoretical limit. Previous studies have manifested that the efficiency of the model predictive control can be very close to the theoretical limit as long as the receding horizon τ is sufficiently long [85]. Therefore, the model predictive control is an effective approach to enhance the energy absorption.

4.4. Summary

A real-time latching control, based on the model predictive control algorithm, is developed in this chapter. A Hamiltonian is introduced to represent the energy absorption, and the real-time algorithm applies the optimal command theory to maximize the energy absorption over a receding time-horizon. When the velocity and the Lagrange multipliers have opposite signs, the point absorber is locked and versa vice. Recede the time-horizon forwards step and step, the latching control is implemented in a real-time manner.

The optimal latching duration is validated against the analytical expression proposed by Babarit and Clement [45]. Both the analytical expression and the numerical simulation indicate that the latched period drops as the wave frequency increases. When the wave frequency is sufficiently high, the latched duration is nearly zero (no latching control is implemented). This feature illustrates that the latching control may be ineffective in short waves where the wave frequency is sufficiently high. Chapter 6.2 will discuss this issue in more details.

In this chapter, the control command is obtained with the assumption that the wave forces over the receding horizon are already known, which is obviously invalid in the real world. In an actual case, the wave forces over the receding horizon must be predicted as to apply the wave energy control. The next chapter will interpret how the short-term wave forces are forecasted using the machine learning algorithm.

Please note that a realistic wave energy controller consumes energy as well. Since this thesis mainly develops the control algorithm rather than builds a realistic controller, this issue is neglected throughout this thesis.

5. Wave Force Prediction with Artificial Neural Network

5.1. Introduction

As presented in Chapter 4, the inputs to the latching control are future wave forces over the receding time horizon so that the wave forces must be known before the latching control could be applied. It is one of the obstacles that prevent the practical application of wave energy control.

Many approaches followed in the literature are based on a spatial prediction of the wave elevation. The wave elevation at a certain location reconstructed from one or more observations at nearby locations. Based on the predicted wave elevations, the wave forces are subsequently estimated using a transferring model. However, the spatial prediction is very complex because it has to take into account the possible multi-direction of waves [59], the presence of radiated and diffracted waves [86], and non-linearities in the waves propagation.

The solution in this thesis is to predict the future wave force based only on its history using an artificial neural network. Although the sea wave forces are stochastic, the future wave forces and the past wave forces are highly correlated by frequency-domain function Eq. (3.16). However, such a correlation is nearly impossible to identify given the time-domain data although it indeed exists. One fantastic power of the neural network is that it can approximate nearly every function [87]. Owing to this feature, the neural network can identify such correlation. The artificial neural network was firstly proposed by Mcculloch and Pitts [88]. At that time, the structure of the neural network was very simple since the inference between densely connected nets with many hidden layers is rather difficult to identify. In 2006, Hinton et al. [89] proposed a fast, greedy algorithm for the multi-layers network. Their work marked the era of 'deep learning'.

In fact, the neural network has already been used for short-term prediction in other fields. Lv et al. [90] used the neural network to predict the traffic flow. Islam and Morimoto [91] utilized the neural network for inside air temperature prediction of a pillar cooler. Recently, the neural network was introduced to marine hydrodynamics.

Pourzangbar et al. [92] predicted scour of breakwaters using genetic programming and artificial neural network, respectively. Ebtehaj et al. [93] developed an integrated framework of machine learning to predict scour at pile groups.

5.2. Artificial neural network

Figure 5-1 illustrates the structure of a multi-layer artificial neural network, which is composed of the input layer, the hidden layers, and the output layer. Several neurons are located in the multiple layers to process the input signals. The signals transfer from the input layer to the output layer without a loop. This kind of neural network is known as the feedforward neural network. For the problem in this study, the input layer is namely the recorded wave forces in the past and the output layer is the prediction of wave forces over the receding horizon. In this thesis, a four-layer artificial neural network (with two hidden layers) is used for the wave force prediction.

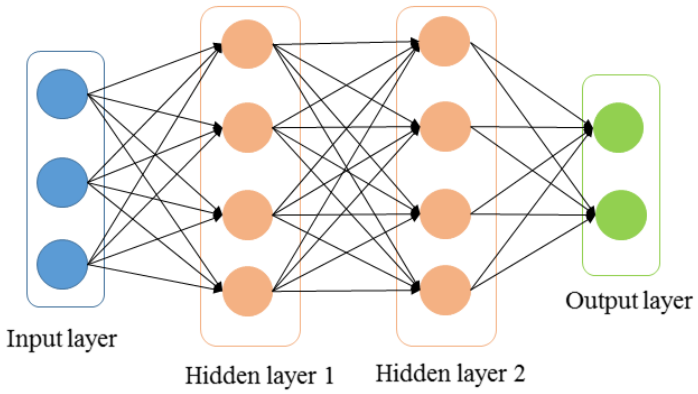

Figure 5-1 Structure of neural network

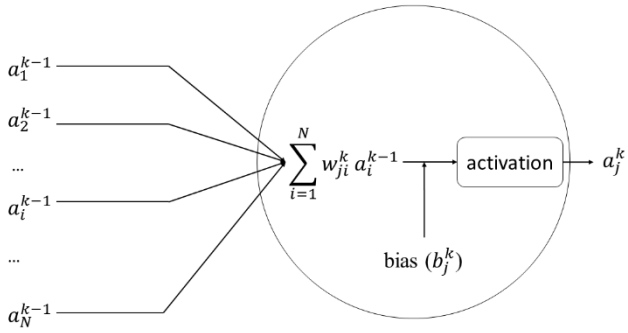

Figure 5-2 The j^{th} neuron in the k^{th} layer

As shown in Figure 5-2, the neuron processes the inputs by two sets of parameters, $\boldsymbol{w}$ = (w_{11}^2, w_{12}^2,…, w_{ji}^k,…) and $\boldsymbol{b}$ = (b_1^2, b_2^2,…, b_j^k,…). w_{ji}^k is the weight for the connection from the i^{th} neuron in the $(k-1)^{\text{th}}$ layer to the j^{th} neuron in the k^{th} layer. b_j^k is the bias of the j^{th} neuron in the k^{th} layer. a_i^{k-1} is the output of the i^{th} neuron in the $(k-1)^{\text{th}}$ layer, also the input of the neurons in the k^{th} layer. Then, the activation of the j^{th} neuron in the k^{th} layer is determined by the activations of all neurons in the $(k\text{-}1)^{\text{th}}$ layer:

$$a_j^k = \sigma\left(z_j^k\right), z_j^k = \sum_{i=1}^{N} w_{ji}^k a_i^{k-1} + b_j^k \tag{5.1}$$

where $\sigma(x)$ is the activation function. The sigmoid function ($\sigma(x) = 1/(1+e^{-x})$) is selected here as the activation function. z_j^k is the weighted input to the activation function of neuron j in layer k.

5.3. Machine learning algorithm

The neural network is a data-driven prediction approach. It learns from observational data, figuring out its own solution to the problem at hand. More specifically, the neural network optimizes the parameters $\boldsymbol{w}$ and $\boldsymbol{b}$ by learning from training examples according to the specific learning algorithm defined by the user. In this thesis, the neural network is trained with the descent gradient method.

5.3.1. Descent gradient method

Denote y is the output and a is the desired target, the objective of the learning algorithm is to optimize parameters $\boldsymbol{w}$ and $\boldsymbol{b}$ to match the output with the target. Define a cost function Θ to estimate the performance of the neural network.

$$\Theta(\boldsymbol{w},\boldsymbol{b}) = \frac{1}{2n}\sum_{k=1}^{n}\|y-a\|^2 \tag{5.2}$$

n is the number of training examples. Given the examples, the objective of 'training' is to find the optimal parameters $\boldsymbol{w}$ and $\boldsymbol{b}$ that minimize the cost function Θ. In this

thesis, the optimal values are searched using the gradient descent method. To clarify how the gradient descent method searches the minimum, It is temporally assumed that Θ is a function of just two variables v_1 and v_2. When a point in the surface is moved a small amount v_1 in v_1 direction and a little amount v_2 in v_2 direction, the cost function changes as

$$\Delta\Theta \approx \frac{\partial\Theta}{\partial v_1}\Delta v_1 + \frac{\partial\Theta}{\partial v_2}\Delta v_2 \tag{5.3}$$

Since the training is aimed at minimizing Θ, v_1 and v_2 must be chosen so as to make $\Delta\Theta$ negative. Otherwise, the cost function will increase and the optimization becomes unstable. Re-express Eq. (5.3) as following:

$$\Delta\Theta \approx \nabla\Theta \cdot \Delta\boldsymbol{v} \tag{5.4}$$

Although Eq. (5.4) is equal to Eq. (5.3), what's really exciting about the equation is that it lets us see how to choose $\Delta\boldsymbol{v}$ so as to make $\Delta\Theta$ negative:

$$\Delta\boldsymbol{v} = -\phi\nabla\Theta \tag{5.5}$$

where ϕ is a positive parameter called the learning rate. Defining $\boldsymbol{v}$ according to Eq. (5.5) guarantees that

$$\Delta\Theta \approx \nabla\Theta \cdot (-\phi\nabla\Theta) = -\phi\left\|\nabla\Theta\right\|^2 < 0 \tag{5.6}$$

So Θ will always decrease if one change $\boldsymbol{v}$ according to Eq. (5.5). Although the descent gradient method is explained here with the assumption that Θ is a function of two variables, everything works just as well even when Θ is a function of many more variables. Suppose Θ is a function of variables $\boldsymbol{v} = (\boldsymbol{w}, \boldsymbol{b})$, where $\boldsymbol{w} = (w_{11}^1, w_{12}^1, \ldots, w_{ji}^k, \ldots)$ and $\boldsymbol{b} = (b_1^1, b_2^1, \ldots, b_j^k, \ldots)$. Then the change of cost function $\Delta\Theta$ produced by a small change $\Delta\boldsymbol{v}$ is:

$$\begin{aligned}
&\Delta\Theta \approx \nabla\Theta \cdot \Delta \boldsymbol{v} \\
&\nabla\Theta = \left(\frac{\partial\Theta}{\partial w_{11}^1}, \frac{\partial\Theta}{\partial b_1^1}, ..., , \frac{\partial\Theta}{\partial w_{ji}^k}, \frac{\partial\Theta}{\partial b_j^k}, ... \right) \\
&\Delta \boldsymbol{v} = \left(\Delta w_{11}^1, \Delta b_1^1, ..., \Delta w_{ji}^k, \Delta b_j^k, ... \right)
\end{aligned} \tag{5.7}$$

Just like the two-variable case, select

$$\Delta \boldsymbol{v} = -\phi \nabla\Theta \tag{5.8}$$

Therefore, the update rule of parameters $\boldsymbol{w}$ and $\boldsymbol{b}$ is defined as:

$$\begin{aligned}
\boldsymbol{w}' &= \boldsymbol{w} - \phi \frac{\partial\Theta}{\partial \boldsymbol{w}} \\
\boldsymbol{b}' &= \boldsymbol{b} - \phi \frac{\partial\Theta}{\partial \boldsymbol{b}}
\end{aligned} \tag{5.9}$$

$\boldsymbol{w}$' and $\boldsymbol{b}$' are the updated weight and bias after training. According to Eq. (5.9), the learn rate represents the sensitivity of the network to the training. A low-level learning rate is beneficial to the reliability of the training, although it makes the learning very slow. If the ϕ is equal to 0, the neural network is totally numb, and it learns nothing from the training examples. The drawback of high learning rate is that the training may become unstable, especially in the late training stage. Although adapting the learning rate during the training process helps address this issue [94], it is very complicated and out of the scope of the present study. Therefore, a constant value of $\phi = 0.01$ is adopted across the training process.

The descent gradient method gives us a way of searching for the minimum of the cost function. Actually, this way is optimal. Suppose that it is to make a move $\Delta \boldsymbol{v}$ in position so as to decrease $\Delta\Theta$ as much as possible. This is equivalent to maximizing $\Delta\Theta \approx \nabla\Theta \cdot \Delta \boldsymbol{v}$. If the size of movement is fixed, one should find the movement direction which decreases Θ as much as possible. Apparently, such direction is the gradient direction $\nabla\Theta$. So gradient descent can be viewed as a way of taking small steps in the direction which does the most to immediately decrease Θ.

5.3.2. Backpropagation algorithm

The descent gradient method develops the updating rule of the weights $\boldsymbol{w}$ and the bias $\boldsymbol{b}$. According to Eq. (5.9), the next task is to estimate the gradient of the cost function at various layers. This thesis adopts the backpropagation algorithm to estimate the gradient of the cost function. The backpropagation algorithm was originally proposed in the 1970s. It is not widely accepted by the research community until the paper of Rumelhart et al. [95]. In that famous paper, they described several neural networks where backpropagation works far faster than earlier learning approaches.

According to Eq. (5.1), if a small change Δz_j^k is added to the weighted input of the neuron, the activation of the neuron will be $\sigma(z_j^k + \Delta z_j^k)$. This small change will propagate through the layers leading to a change of the cost function $\frac{\partial \Theta}{\partial z_j^k} \Delta z_j^k$. It gives a guideline on how to reduce the cost function. Regardless of the sign of $\frac{\partial \Theta}{\partial z_j^k}$, one can choose Δz_j^k to have the opposite sign. In this way, the cost function is always reduced. If $\frac{\partial \Theta}{\partial z_j^k}$ has a relatively large value, then a small change Δz_j^k could lead to a noticeable change of the cost function. It indicates that the neural network is far from optimal. If $\frac{\partial \Theta}{\partial z_j^k}$ is very small, then the change of cost function will be limited since Δz_j^k is also a small value. In this circumstance, the neural network is stable and near optimal. Consequently, one can use the gradient of the cost function to represent the error of the j^{th} neuron in the k^{th}

$$\delta_j^k = \frac{\partial \Theta}{\partial z_j^k} \tag{5.10}$$

The backpropagation algorithm presents a way of estimating the error at each layer and then relating the error to the gradient of the cost function, which is of real interest in the machine learning. Before the interpretation of the backpropagation algorithm, four fundamental equations are given at first.

Equation1: estimation of the error in the output layer

$$\delta_j = \frac{\partial \Theta}{\partial a_j} \sigma'\left(z_j\right) \tag{5.11}$$

Equation2: the relation between the error in two adjacent layers

$$\delta_i^k = \sum_i w_{ji}^{k+1} \delta_j^{k+1} \sigma'\left(z_i^k\right) \tag{5.12}$$

Equation3: gradient of the cost function with respect to bias

$$\frac{\partial \Theta}{\partial b_j^k} = \delta_j^k \tag{5.13}$$

Equation4: gradient of the cost function with respect to weight

$$\frac{\partial \Theta}{\partial w_{ji}^k} = a_i^{k-1} \delta_j^k \tag{5.14}$$

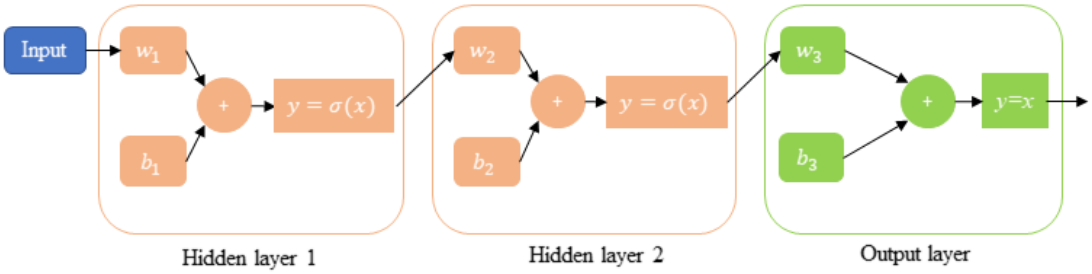

Figure 5-3 A four-layer neural network

The backpropagation algorithm is summarized as following:

1. Select the input.
2. Compute the weighted input $z_j^k = \sum_i w_{ji}^k a_i^{k-1} + b_j^k$ and the activation $a_j^k = \sigma\left(z_j^k\right)$ at each layer.
3. Compute the error at the output layer (Eq. (5.11)).
4. Backpropagate the error (Eq. (5.12)).

5. Estimate the gradient of the cost function (Eq. (5.13) and Eq. (5.14)).

5.4. Estimation of prediction ability

It is well-known that the successful implementation of real-time control requires accurate prediction of wave forces otherwise the control performance may become poor [96]. The prediction ability of the trained neural network is checked through comparison with the traditional prediction methodology-the first-order grey model with one variable, GM(1,1). The detailed procedure of using the grey model for prediction can be found in Appendix B.

The random wave elevations measured in Li et al. [97] is used to examine the prediction ability of the two models. The measured data were low-pass filtered to remove the high-frequency wave noise. The significant wave height of the random wave elevations is 0.04 m and the wave peak period is 1.13 s. Although the neural network forecasts wave forces in the present research, it can be validated by the wave elevations since both variables are random signals by nature. 100 s of wave elevation measurement are selected as the training example. The first 50 s data are used to train the neural network and the last 50 s are used for validation. Hong and Billings [98] proposed a simplified prediction index for quantitative assessment of the prediction

$$Er(\Delta t) = \frac{\int_{\Delta t}^{T} h^2(\tau) d\tau}{\int_{0}^{T-\Delta t} \bar{h}^2(\tau + \Delta t | \tau) d\tau} \tag{5.15}$$

where $h(t)$ is the measured wave elevation at time instant t; $\bar{h}(t + \Delta t | t)$ is the Δt time ahead wave elevation predicted at time instant t. $Er < 1$ indicates that the predicted values are larger than the target and vice versa. Er close to 1 represents a good prediction capacity.

Figure 5-4 compares the prediction performances of the two models. The neural network behaves better than the grey model. The index Er estimated by the neural network is generally around 1. It indicates that the training based on 100 s data is reliable. Although the training performance may improve using more data, the over-

fit problem may also incur. Therefore, 100 s data are used here. Figure 5-5 plots the predicted wave elevation histories. The wave elevation predicted by the neural network agrees well with the measurement whereas the grey model overestimates the wave elevation substantially.

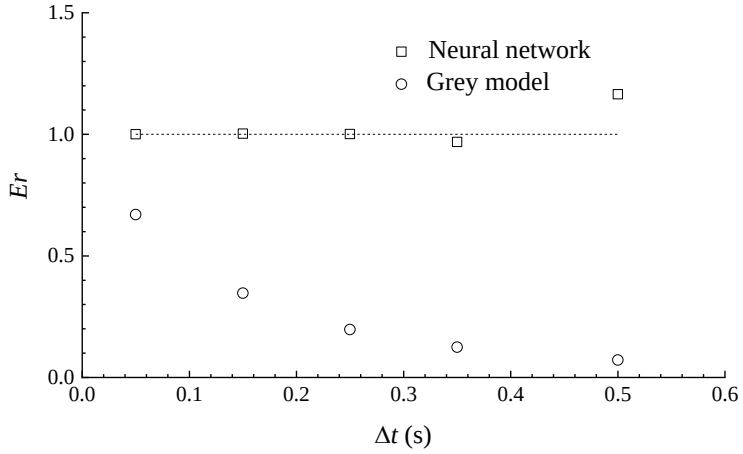

Figure 5-4 Prediction index *Er*.

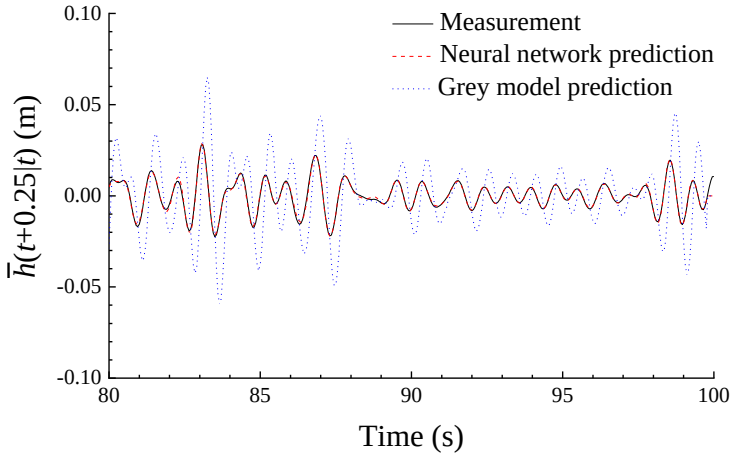

Figure 5-5 Histories of predicted wave elevation with Δt = 0.25 s.

5.5. Summary

As presented in Chapter 4, the model predictive control is non-causal. The current output of a non-causal system is based on variables in the future. The control input in the present control algorithm is the future wave excitation forces over the receding time horizon. According to linear wave theory, the future wave forces and past wave forces are closely correlated, but the correlation is difficult to identify in time-domain. Considering that the neural network can approximate most continuous functions, it is

used to identify such correlation and make the predictions. A feedforward multi-layer neural network is thus developed in this chapter for the short-term wave force prediction.

Unlike the deterministic prediction approach which must be defined by the user, the neural network is a data-driven forecasting method. The neural network itself adapts to the problem concerned by learning from examples with a pre-set learning algorithm. That is to say, the prediction model is defined by the training data and the learning algorithm, rather than by the user. In fact, the user even has no idea about the details of the neural network before the training process is finished.

The neural network is trained with the descent gradient method, which is aimed at searching the most efficient route (gradient direction) to decrease the output error. The descent gradient method optimizes the configurations (weight $\boldsymbol{w}$ and bias $\boldsymbol{b}$) by estimating the gradient of the so-called cost function at various layers. The gradient of the cost function is assessed using the backpropagation algorithm. The backpropagation algorithm establishes a relation between the gradient of the cost function and the output error at multiple layers. Also, how the output error transfer between layer is identified. So, the training process starts with estimating the error at the output layer, and then backpropagate the error to the front layers. In this way, the gradient of the cost function at multiple layers can be estimated and the parameters $\boldsymbol{w}$ and $\boldsymbol{b}$ are updated accordingly.

Comparison with the grey model GM(1,1) shows that the neural network has a better prediction ability. The prediction performances of both approaches become poor when the predictive horizon increases. If the predictive horizon is too long, then the prediction makes little sense since the error is so significant.

6. Control Effect on Energy Absorption

6.1. Introduction

The above chapters have developed the dynamic model, the real-time control algorithm, and the short-term wave force prediction model. Now, the smart controller is implemented to the heaving point-absorber in this chapter to maximize its energy absorption. This chapter will mainly concentrate on three aspects

- Enhancement of the energy absorption
- Effect of the receding horizon length
- Effect of the prediction error

6.2. Energy absorption in regular waves

To illustrate how the latching control enhances the energy absorption, the control performance in regular waves is investigated at first. Since the waves are regular, the wave forces over the prediction horizon are assumed already known. The wave amplitude A is 1 m. Figure 6-1 plots the sensitivity of energy absorption to the wave oscillation frequency. It is desirable to see that the energy absorption is increased with the controller, although it is not effective within the high-frequency range. According to Figure 4-2, the optimal latched duration reduces gradually when the wave frequency increases and it reduces to nearly zero in the case of very high-frequency waves. It implies that it is unable to regulate the point-absorber in high-frequency wave and thereby the energy absorption is hardly increased. Babarit et al. [48] pointed out that the optimal duration of a single locked stage is close to half natural period of the WEC on condition that the PTO damping coefficient C is sufficiently small (weak damping). Therefore, the solution of the control command is only available when the wave period is sufficiently long. Although the damping coefficient C is rather large in the present WEC model and the model predictive control algorithm is used here, their findings can still help to interpret why the latching control is merely effective in low-frequency waves. Considering that the effective frequency range [0.1 rad/s, 1 rad/s] covers the dominating frequencies of a typical wave spectrum, the real-time latching control

would be effective in random waves. Chapter 6.3 will investigate the control performance in random waves.

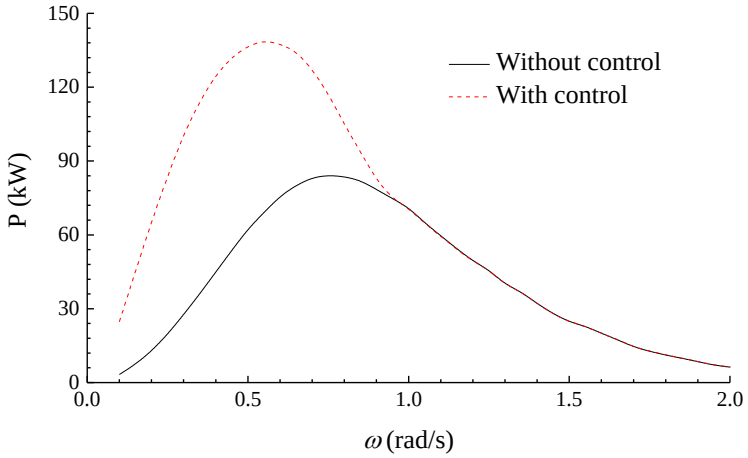

Figure 6-1. Average energy absorption in regular waves, A = 1m, $\tau = 0.2 \cdot (2\pi/\omega)$.

Figure 6-2 displays the phase portrait of the response. It is obvious that the velocity phase is tuned by the controller. As discussed, the latching control is a kind of phase control by nature and maximizes energy absorption by tuning velocity phase. Figure 6-3 illustrates the regulation of the controller on the dynamics of the point-absorber. The point-absorber is latched and released alternately so that the response is a succession of locked and ramp stages. Due to the regulation of the controller, the velocity and the wave forces are generally in phase so that wave forces will always accelerate the floater and the floater carries more kinetic energy as a result. Please note that the real-time control maximizes the energy extract over the receding horizon rather than over the entire time interval. Therefore, the real-time control is sub-optimal and the velocity and the wave force are not exactly in phase. In Figure 6-3, the receding horizon length is $0.2 \cdot (2\pi/\omega)$. If the receding horizon length is increased, the phase difference between the velocity and the wave force could be reduced. Please refer to Chapter 6.4 for more details.

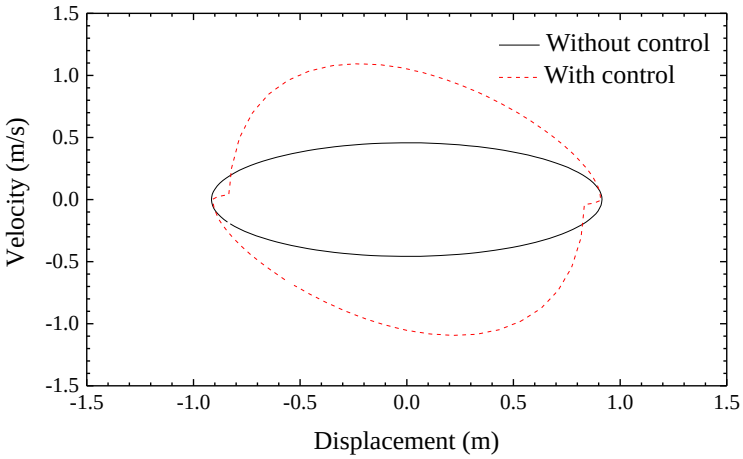

Figure 6-2. Phase portrait, ω = 0.5 rad/s, $\tau = 0.2 \cdot (2\pi/\omega)$.

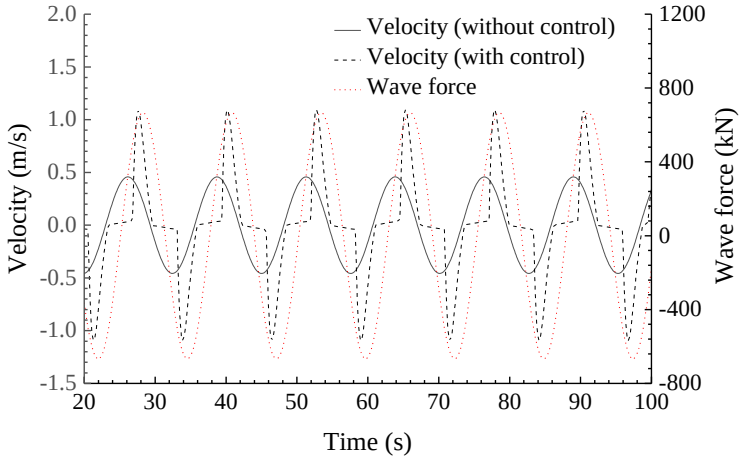

Figure 6-3. Responses of the floater in regular wave, ω = 0.5 rad/s, $\tau = 0.2 \cdot (2\pi/\omega)$.

Figure 6-4 plots the phase between the un-controlled velocity and the wave excitation force under the high-frequency regular wave. When the wave frequency is higher than the resonant frequency of the WEC, the movement is generally in phase with the wave force even in the absence of latching control. It inherently implies that it there is no need to apply the latching control to adjust the velocity phase. Therefore, the energy absorption is hardly increased on within the high-frequency range in Figure 6-1.

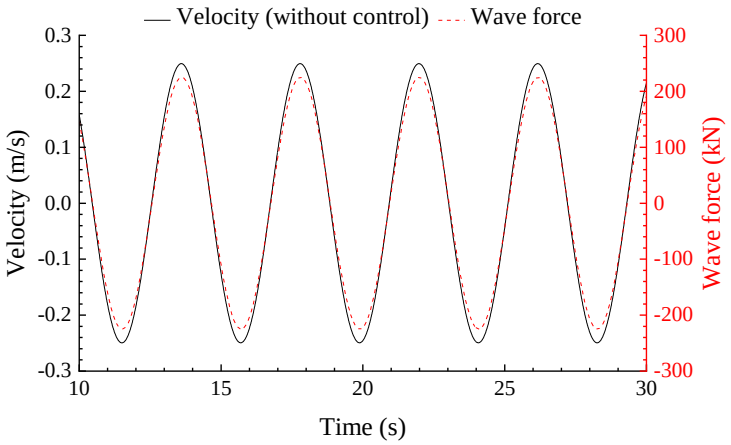

Figure 6-4. Responses of the floater in regular wave, ω = 1.5 rad/s.

6.3. Energy absorption in random waves

To check the effectiveness of the smart real-time controller, the performance of the point-absorber subject to random waves is simulated. The joint distribution model of stochastic waves proposed by Li et al. [99] is used to specify the wave condition. The distribution model is based on the field measurement at Atlantic from 2001 to 2010. The marginal distribution of significant wave height H_s follows a hybrid lognormal and Weibull distribution

$$f_{H_s}(h_s)=\begin{cases}\dfrac{1}{\sqrt{2\pi}\sigma_{LHM}h_s}\cdot\exp\left[-\dfrac{1}{2}\left(\dfrac{\ln(h_s)-\mu_{LHM}}{\sigma_{LHM}}\right)^2\right] & h_s\le h_0\\ \dfrac{\alpha_{HM}}{\beta_{HM}}\left(\dfrac{h_s}{\beta_{HM}}\right)^{\alpha_{HM}-1}\cdot\exp\left[\left(-\dfrac{h_s}{\beta_{HM}}\right)^{\alpha_{HM}}\right] & h_s>h_0\end{cases} \tag{6.1}$$

The conditional distribution of peak period T_p at a given significant wave height follows a lognormal distribution. Detailed values of these parameters can be found in Li et al. [99].

$$\begin{aligned}&f_{T_p|H_s}(t_p|h_s)=\frac{1}{\sqrt{2\pi}\sigma_{LTC}t_p}\cdot\exp\left[-\frac{1}{2}\left(\frac{\ln(t_p)-\mu_{LTC}}{\sigma_{LTC}}\right)^2\right]\\ &\mu_{LTC}=c_1+c_2\cdot h_s^{c_3}\\ &\sigma_{LTC}^2=d_1+d_2\cdot\exp(d_3\cdot h_s)\end{aligned} \tag{6.2}$$

A set of significant wave height H_s (2 m, 4 m, 6 m) are selected at first, and the most probable peak period T_p are subsequently determined based on the joint model. The selected random wave conditions are listed in Table 6-1. 4000 s of random wave elevations are generated totally in each simulation case and the response in the first 400 s is cut off to eliminate the transient effect arising in the early simulation stage. The receding horizon length is 2.5 s.

Table 6-1 Wave conditions

	Case 1	Case 2	Case 3
H_s (m)	2	4	6
T_p (s)	11.11	12.33	13.27

Figure 6-5 plots the response under the regulation of the controller. Like regular wave case, the point-absorber is locked and released alternately. The floater is locked when the velocity vanishes. Once the floater is released, the velocity ramps rapidly. Furthermore, the controller velocity is closely associated with the wave forces. The floater is locked when the velocity and the wave forces are reverse and released again when they become aligned. In the meanwhile, the velocity and the wave forces nearly reach their maximum at the same time instant. It seems that the resonance is achieved with the real-time control. As stated before, the latching control is a kind of phase control, which maximizes the energy absorption by making the velocity in phase with the wave force. According to Figure 6-5, the velocity and the wave force are indeed in phase. In this circumstance, the wave forces will always accelerate the floater so that it will carry more kinetic energy. As shown in Figure 6-6, the wave forces sometimes slow down the floater without the real-time control since the work done on the floater is negative occasionally. When the floater motion is controlled, one can see that the wave excitation forces mostly do positive work to the floater.

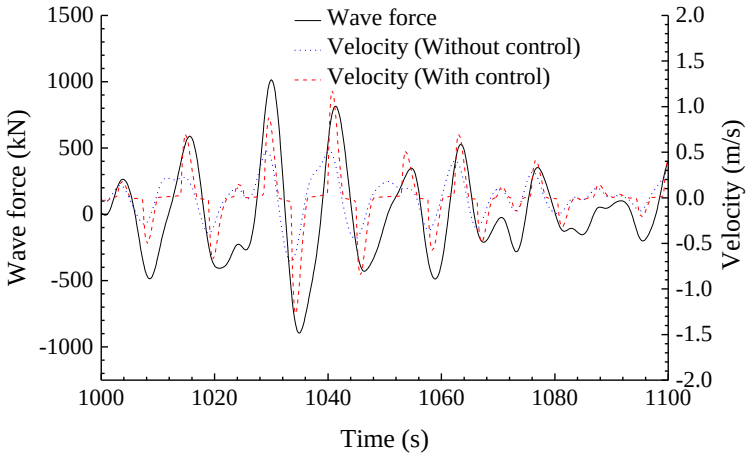

Figure 6-5. Responses of the point-absorber, Case1.

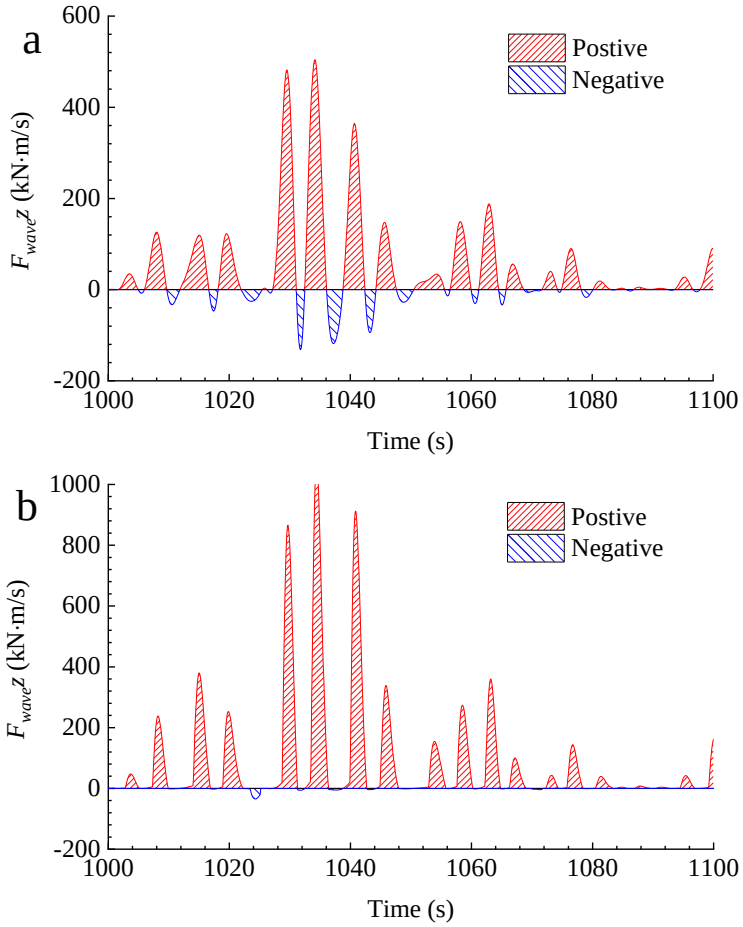

Figure 6-6 Work on the floater done by the wave excitation force. Case1. (a) Without control; (b) With control.

The control effect on the energy absorption is illustrated in Figure 6-7. Although the point-absorber is locked frequently and the PTO systems stop working during this duration, the energy extraction ramps once the point-absorber is set free since the velocity runs up rapidly during the ramp stage. It leads to the improvement of the

overall energy absorption. The 1-hr average energy harvesting under various wave conditions is presented in Figure 6-8. Generally, the point-absorber produces 60%~80% more energy when the smart controller is working.

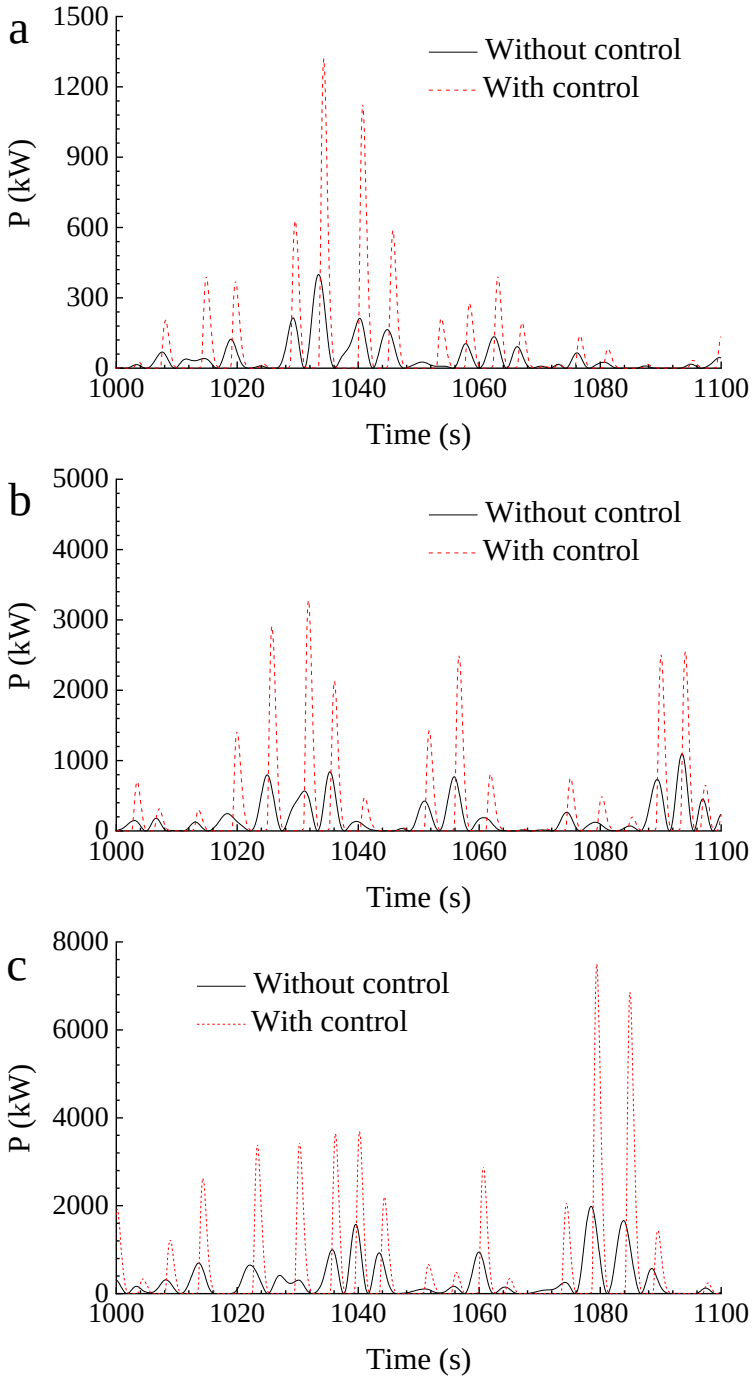

Figure 6-7. Power capture. (a) Case1; (b) Case2; (c) Case3.

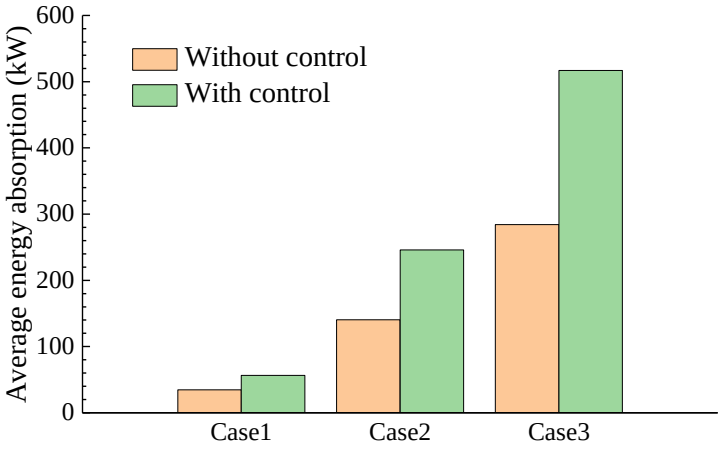

Figure 6-8. Average energy harvesting.

To demonstrate the advantage of the neural network against traditional prediction approach, the smart controller is compared with that using the grey model GM(1,1) to predict wave forces. The control efficiency will be evaluated to show the effectiveness of the two prediction models. Table 6-2 lists the average power extraction of the point-absorber using different wave force prediction models. As shown, the control efficiency is increased considerably when the wave forces are predicted by the neural network. Since the point-absorber is subject to identical wave forces regardless of the prediction model used, the discrepancies on the control performance are totally caused by the different control commands.

Table 6-2 Average power extraction with different prediction models

	Case1	Case2	Case3
Neural network	56 kW	246 kW	517 kW
GM(1,1)	50 kW	201 kW	429 kW

Figure 6-9 plots the optimal control command and the control command predicted by the two forecasting models. Due to the unavoidable prediction deviation, the predicted control command is somewhat different from the optimal one. Even so, it is still easy to find that the command predicted by the neural network is closer to the theoretical optimal one, attributing to the better prediction capacity. A more appropriate control command indicates the point-absorber will be released and locked at the right instant and thereby the point-absorber extracts more power from the ocean waves.

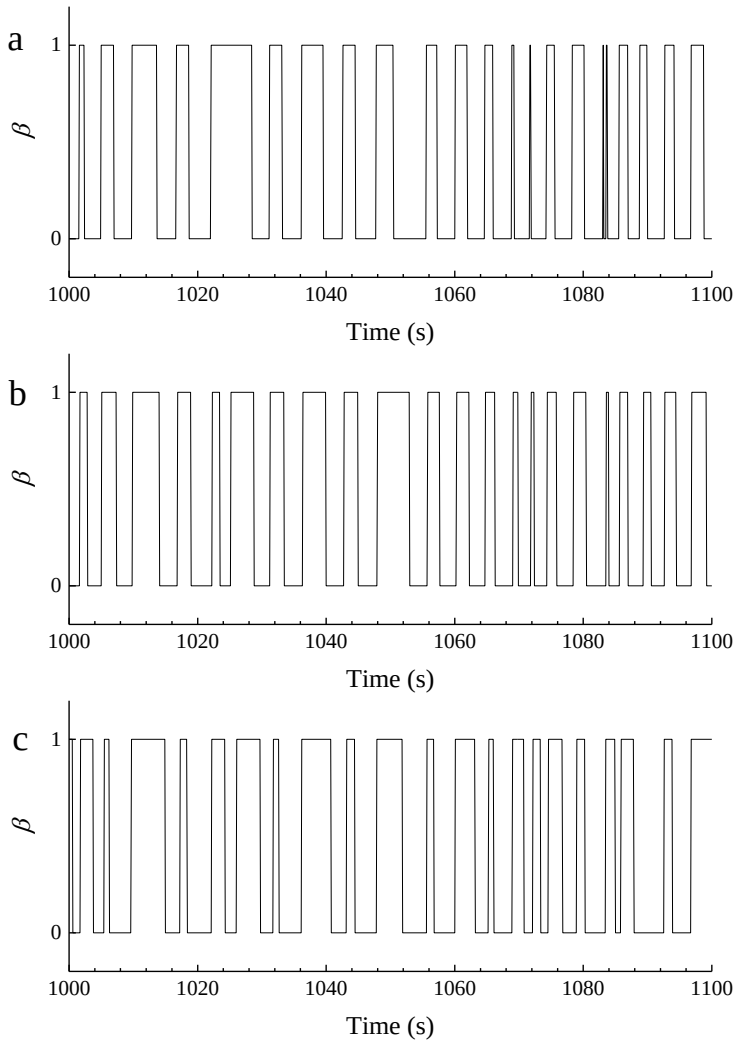

Figure 6-9 Control command forecasted with different prediction models, Case1. (a) Theoretical optimal; (b) Neural network; (c) GM(1,1).

As discussed in Chapter 4.3, the model predictive control can be regarded as a kind of sub-optimal control. Consequently, the efficiency of the real-time controller is evaluated by comparing with the optimal control (the theoretical limit). Please note that by implementing the optimal control it inherently implies that the wave forces over the entire interval are already known. Table 6-3 lists the average energy absorption obtained by using the real-time control and the optimal control. Generally, the real-time control generally underestimates the energy harvesting by around 10%. Although the real-time control algorithm is sub-optimal and the future wave forces are predicted, the control efficiency is still satisfactory.

Table 6-3 Average energy absorption estimated by real-time control and optimal control.

	Real-time control	Optimal control
Case1	56 kW	61 kW
Case2	246 kW	266 kW
Case3	517 kW	571 kW

The difference in energy absorption is caused by the control command, which is displayed in Figure 6-10. The control command given by the smart controller is generally close to the optimal one, indicating that the efficiency of the smart controller is satisfactory. Some discrepancies are observed since the receding horizon control is sub-optimal by nature. It cannot acquire the optimal sequence since the control command is optimized over the prediction horizon. Also, the prediction deviation is unavoidable. The control command is derived based on the predicted wave force whereas the point-absorber is subject to the real wave force, and thereby the derived control command may be not compatible with the actual situation completely. Chapter 6.4 and Chapter 6.5 will investigate the two issues, respectively.

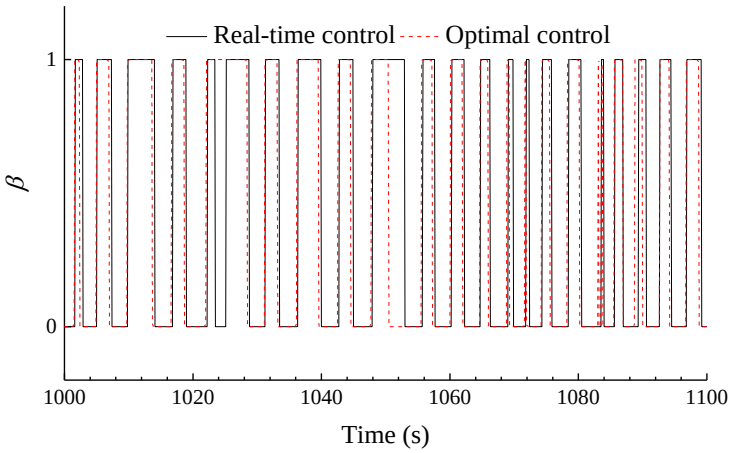

Figure 6-10. Control command, Case 1.

Additionally, one can find that the agreement between the real-time control and the optimal control is bad at time intervals [1020 s, 1028 s] and [1080 s, 1080s]. According to the time series of the wave forces plotted in Figure 6-5, the high-frequency variations of the wave forces are observable. Since the receding horizon is 2.5 s, if more wave force cycles appear in this period, the prediction performance of the

artificial neural network becomes worse and thereby significant discrepancies are observed between the two control strategies.

6.4. The influence of receding horizon length

The effect of receding horizon length is investigated in this sub-chapter. To eliminate the prediction deviation, the wave forces over the receding horizon are given so that the prediction deviation is exactly zero.

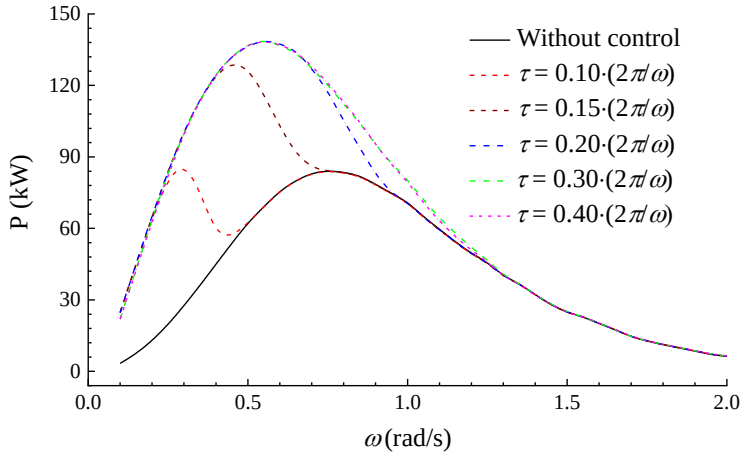

Figure 6-11. Average energy absorption in regular waves with various receding horizon lengths, A= 1 m.

Figure 6-11 illustrates the energy absorption in regular waves corresponding to various receding horizon lengths. A notable feature in Figure 6-11 is that the real-time control is more efficient with a long receding horizon τ (The receding horizon is represented by the percentage with respect to wave period). In the case of τ = 0.2·($2\pi/\omega$), the efficiency of the real-time control is sufficiently high. It is why τ = 0.2·($2\pi/\omega$) is adopted in Chapter 6.2. When the receding horizon is as long as the entire simulation interval, the model predictive control reduces to the optimal control. It is why the energy conversion increases with the length of receding horizon. As shown in Eq. (4.5), the control command is derived by assuming that the Lagrange multipliers $\boldsymbol{\chi}$ satisfy $\boldsymbol{\chi}(T) = \mathbf{0}$. Such an assumption is adopted since $\boldsymbol{\chi}$ must calculated given an initial condition. Please note that it is just an assumption, not the actual case. When T is sufficiently long, this assumption has a very limited influence on the control command. It is similar with the dynamic model of the point-absorber. The initial condition $\boldsymbol{x}(0) = \mathbf{0}$ (Eq. (3.28)) is given to calculate the dynamic response of the floater.

The transient effect induced by the initial condition will dissipate as long as the simulation is run enough time. In the optimal control, the simulation interval [0, T] is typically sufficiently long so that the transient effect produced by the initial condition $\boldsymbol{\chi}(T) = \mathbf{0}$ is negligible. However, the control command in the model predictive control is merely based on the receding horizon [t_{i+1}, $t_{i+1}+\tau$] and thereby such effect is not negligible. The transient effect also dissipates as the horizon length τ increases, explaining why the real-time control is more efficient with a long horizon length.

Furthermore, long regular waves are more sensitive to the receding horizon. As shown, a relatively short receding horizon is sufficient in long wave to enlarge the energy absorption. For example, receding horizon equal to 15% of the wave period can significantly increase the energy capture at ω = 0.3 rad/s whereas it is not effective at all at ω = 0.6 rad/s. Figure 6-12 shows the effect of receding horizon more clearly. The variation of energy absorption is characteristic of a sigmoid curve, in which three regions are identified. When the determination of control command is based on a short horizon length, the energy absorption remains relatively stable regardless of the expansion of the prediction horizon. In this region, the control action is not effective at all and the energy absorption is identical to that without control. The performance of the point-absorber is most sensitive to the receding horizon within the middle region, where the energy absorption increases rapidly. As the receding horizon continues increasing, the energy absorption gradually converges to the optimal level. Any further increase of prediction horizon length has a very limited influence on the performance. By checking the slope of the curves within the middle segment, it manifests that the energy absorption is indeed more sensitive to the receding horizon at long regular waves.

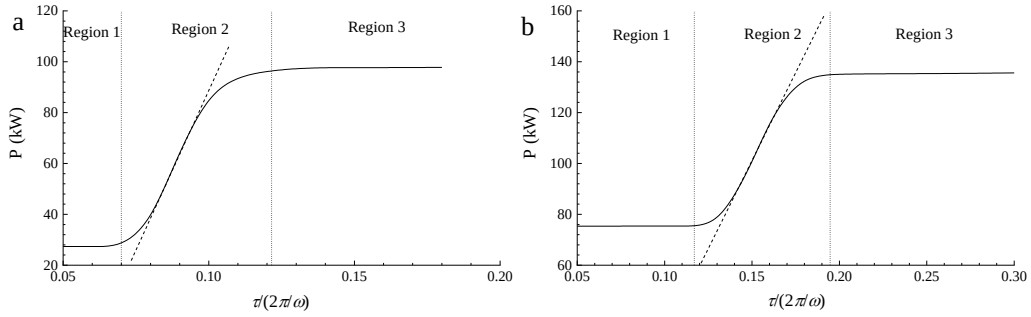

Figure 6-12. Variation of average energy absorption with receding horizon. (a) ω = 0.3 rad/s; (b) ω = 0.6 rad/s

To interpret the strategy behind, Figure 6-13 plots the control command and the corresponding velocity. When the deduction of the control command is based on short receding horizon, the latching action is seldom applied, implying that the velocity phase is hardly tuned. Consequently, the response remains sinusoidal and the enhancement of energy absorption is limited. As the receding horizon becomes longer, the latching action becomes stronger. As shown in Figure 6-13(b), the point-absorber is locked for a longer period and the tuning of the velocity phase is more considerable. In this circumstance, the energy absorption is increased. When the receding horizon is sufficiently long, the control command converges. Figure 6-14 illustrates the variation of the response phase with the receding horizon. The response phase is hardly tuned with short prediction horizon. As the duration keeps increasing, the phase portrait rephrases gradually until converges to the optimal one in the end.

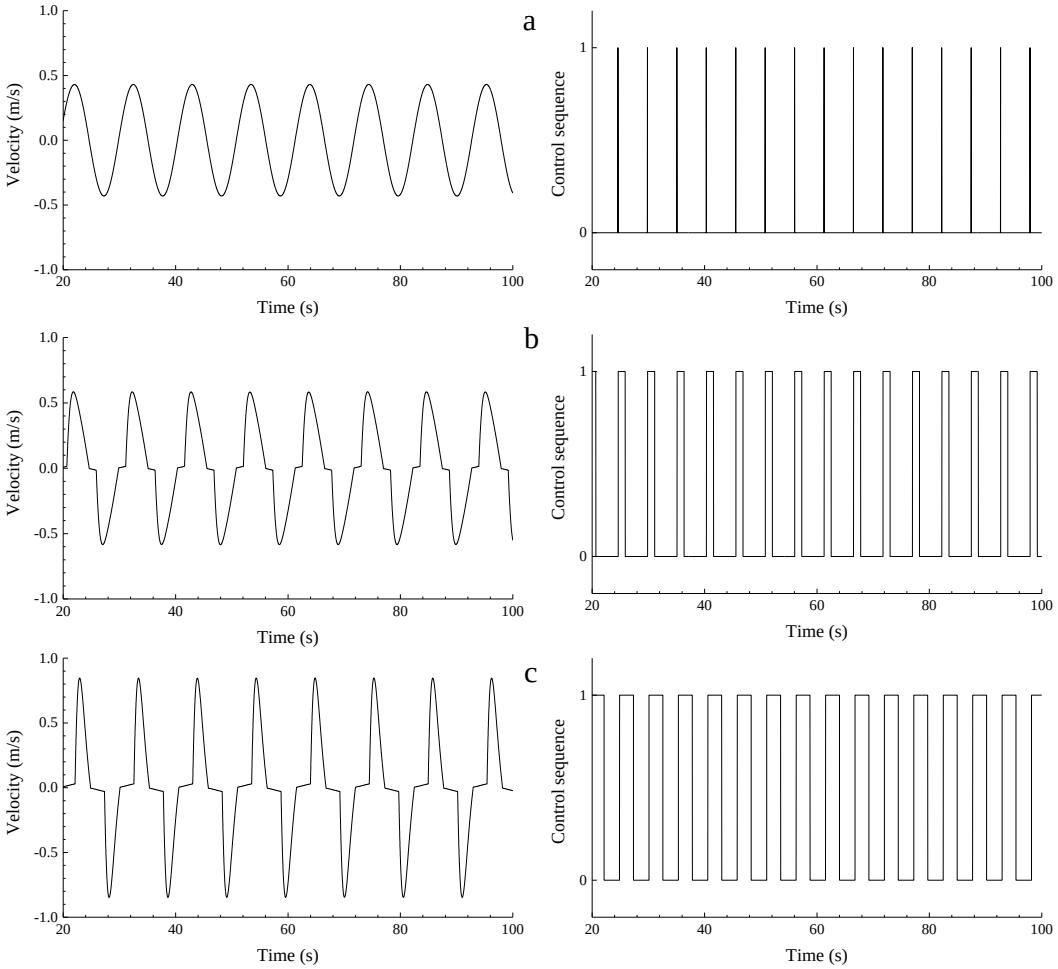

Figure 6-13. Time series of velocity and control command, ω = 0.6 rad/s. (a) τ = 0.1T; (b) τ = 0.15T; (c) τ = 0.2T.

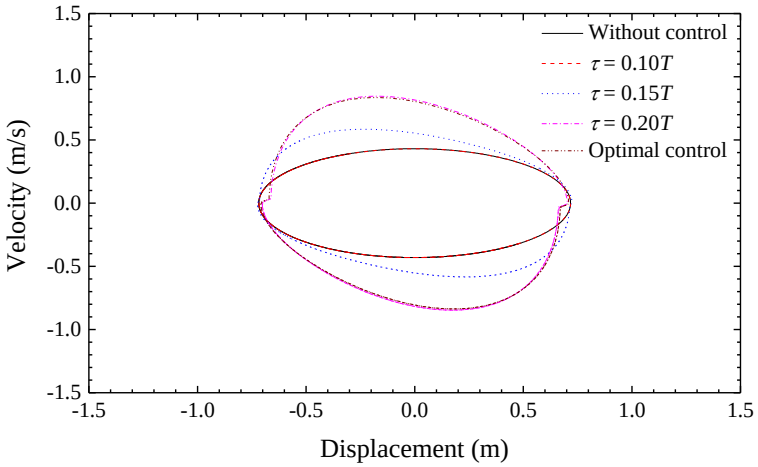

Figure 6-14. Variation of phase portrait with prediction horizon, ω = 0.6 rad/s.

Figure 6-15 illustrates how the average energy absorption varies with the length of the receding horizon in irregular waves. Three segments are identified within which the energy absorption shows different features. When the determination of control command is based on a short horizon length, the energy absorption remains relatively stable. In this segment, the control action is not effective at all as the energy absorption is identical to that without control. The performance of WEC is most sensitive to the horizon length within the middle segment. In this region, the energy absorption increases significantly with the prediction horizon. As the horizon length continues increasing, the energy absorption gradually converges to a fixed level. Any further increase of prediction horizon length has a very limited influence on the performance.

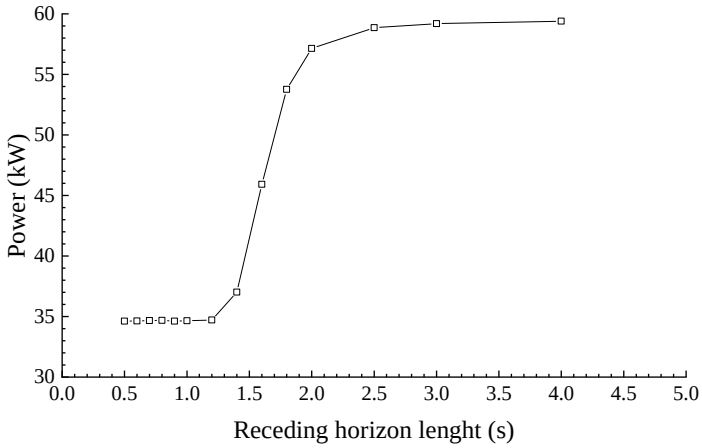

Figure 6-15 Variation of energy absorption with prediction horizon length, Case1.

Figure 6-16 illustrates how the receding horizon length influences the control command. When the length is very short, one can see that there is nearly no control action on the PTO system. For most of the moment, the floater is released. It is why the energy capture performance is hardly improved. As the length increases, the floater is latched more frequently indicating that the control action grows stronger. As a result, energy absorption increases gradually. When the receding horizon is sufficiently long, the control command in Figure 6-16 (c) and Figure 6-16 (d) match well with each other. Consequently, the curve in Figure 6-15 converges to a fixed level at the tail region.

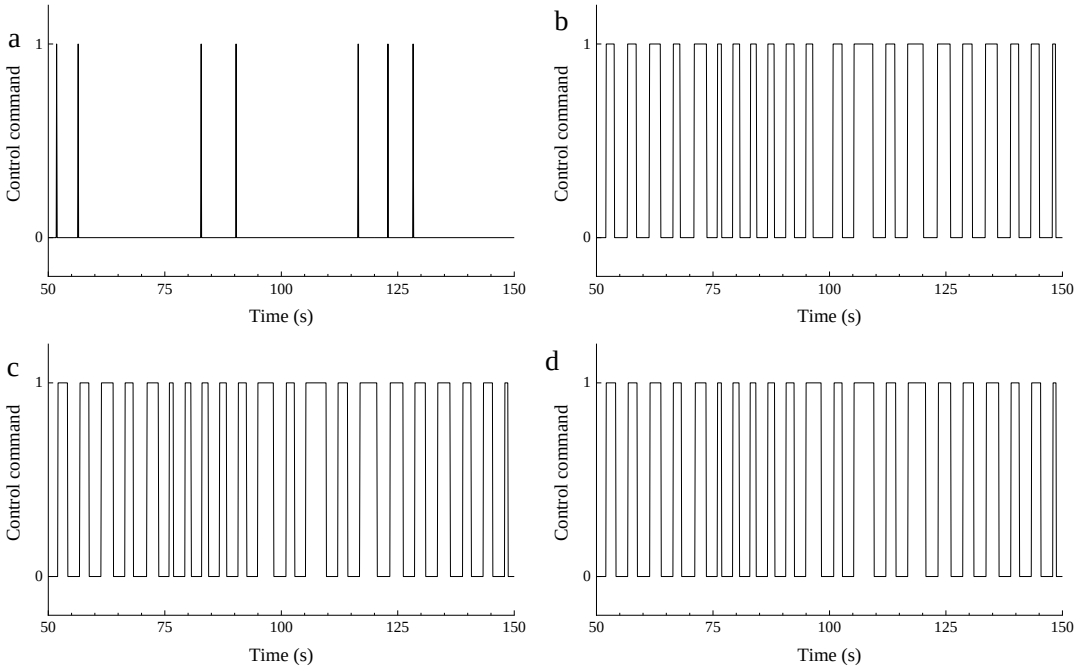

Figure 6-16 Control command with various prediction horizon lengths, Case1. (a) τ = 1.0 s; (b) τ = 2.0 s; (c) τ = 3.0 s; (d) τ = 4.0 s.

6.5. The influence of prediction error

The discussions in Chapter 6.4 are based on the assumption that the wave forces over the receding horizon are known so as to eliminate the prediction deviation. The derivation of the control command is based on the relationship between the velocity $\dot{z}$ and the Lagrange multipliers χ. Moreover, χ is a function of wave forces. Consequently, the control command is dependent on the velocity and the wave forces. In practical application, the control command must be derived based on the predicted wave forces whereas the point-absorber is subject to the true wave forces, implying that the control

command is not completely compatible with the point-absorber motion. That is to say, the control command based on wave force prediction may lock and release the point-absorber at the wrong time instants. For example, the predicted wave forces are out of phase with the velocity and thereby the control algorithm decides to the lock the point-absorber. However, the true wave forces are in phase with the velocity, in which condition the point-absorber should be released. Consequently, the effectiveness of the latching control is reduced. Apparently, such effect is caused by the prediction deviation.

According to Eq. (3.16), the prediction deviation can be separated into two components, namely the amplitude deviation and the phase deviation. Therefore, the predicted wave forces with arbitrary deviations are defined manually

$$\begin{aligned} \bar{F}_{amplitude}(t) &= \mathrm{Re}\left[\alpha\psi(\omega)Ae^{i(\omega t+\varepsilon)}\right] \\ \bar{F}_{phase}(t) &= \mathrm{Re}\left[\psi(\omega)Ae^{i(\omega t+\varepsilon+\theta)}\right] \end{aligned} \tag{6.3}$$

where $\bar{F}_{amplitude}$ are the predicted wave forces involving only deviation of amplitude, $\bar{F}_{phase}$ are the predicted wave forces involving only deviation of phase. α and θ are parameters to represent deviations of amplitude and phase, respectively. $\alpha = 1$ and $\theta = 0$ means that there is no prediction deviation. The control command over the receding horizon is based on the defined wave forces (Eq. (6.3)) whereas the dynamics of the point-absorber is still determined by the real wave forces (Eq. (3.16)). Please note that by applying Eq. (6.3), the wave forces over the prediction horizon is pre-generated artificially rather than predicted with the neural network.

Figure 6-17 shows the sensitivity of average energy absorption to the amplitude deviation. It is not unexpected to find that the energy absorption performance varies hardly with the amplitude deviation. The latching control is a kind of phase control by nature so that amplitude deviation will have little influence on the control command.

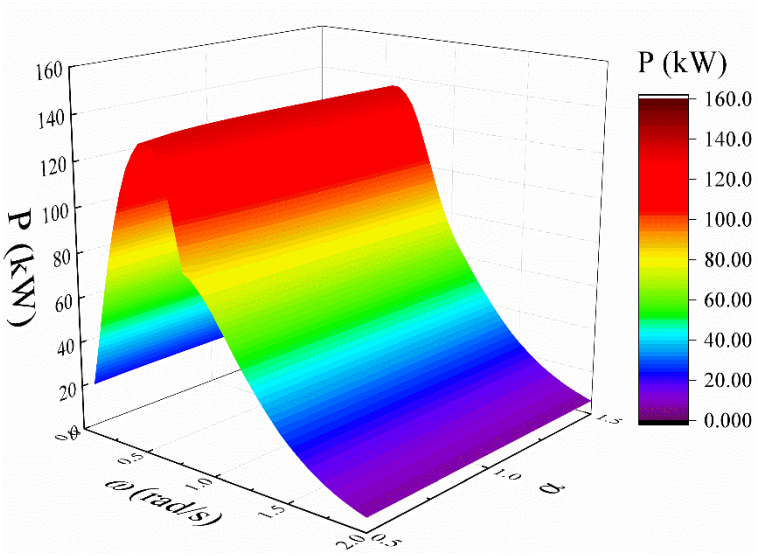

Figure 6-17 Influence of amplitude deviation on the energy absorption, A = 1 m, τ = 0.2T.

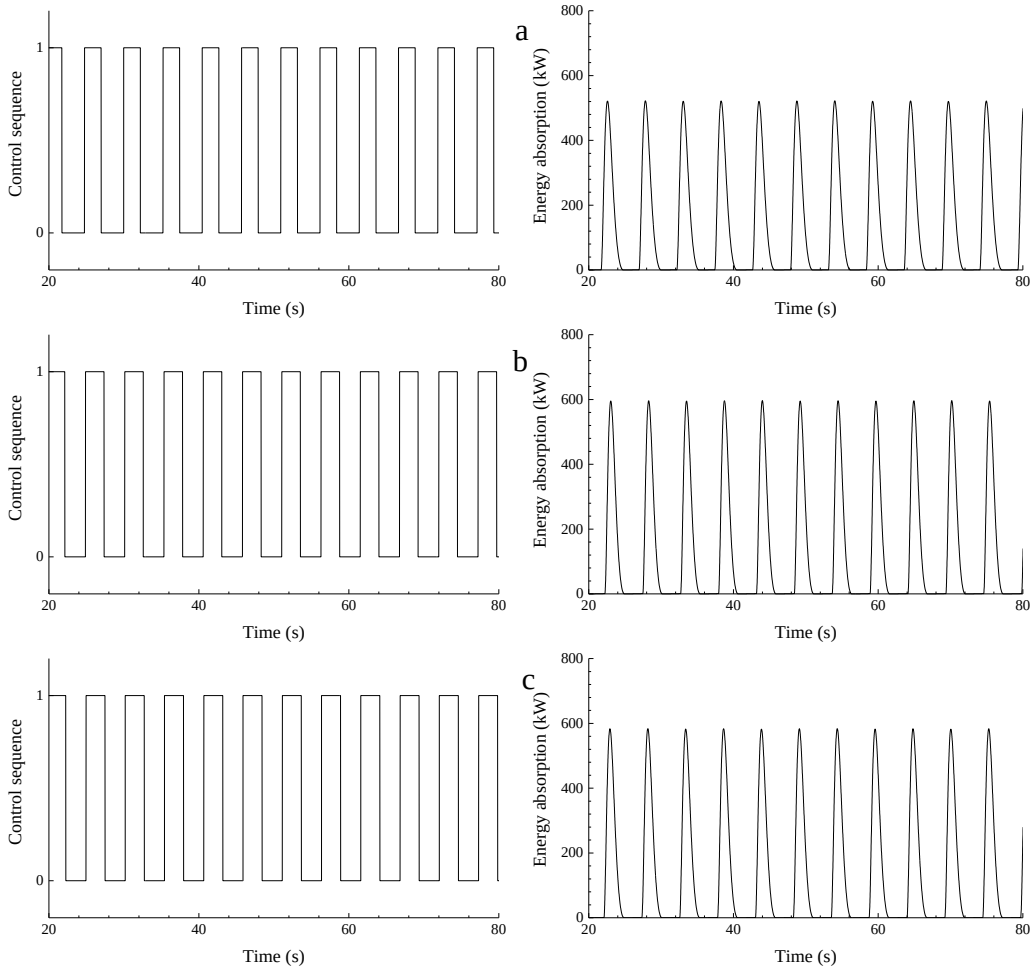

Figure 6-18 Influence of phase deviation on energy absorption, ω = 0.6 rad/s. (a) α = 0.5; (b) α = 1; (c) α = 1.5.

Figure 6-18 plots the derived control command and the corresponding energy absorption when different levels of amplitude deviation are involved. As shown, the control command varies hardly with the amplitude deviation and so is the energy absorption. According to Eq. (3.28), the amplitude deviation will only influence the amplitudes of velocity and Lagrange multiplier χ whereas the signs are not reversed. Therefore, the control command nearly remains the same and the energy absorption varies hardly.

Figure 6-19 displays the average energy absorption considering the prediction deviation of phase. It can be seen that the effect of phase deviation on average energy absorption is significant. In the high-frequency range, the contour is relatively flat since the control algorithm can't find the solution in this region. The explanation has been presented in the above chapter and previous studies [45, 48]. Consequently, the control command is equal to zero even in the presence of phase deviation. The maximum energy absorption is achieved at $\theta = 0$ in the absence of phase deviation. As the phase deviation extends, the energy absorption drops rapidly. Such variation trend is straightforward to understand. Since the latching control maximises energy absorption by tuning the phase, it is thus most sensitive to the phase deviation. Due to the phase deviation, the predicted wave force may be out of phase with the velocity whereas the real situation is that the wave force is in phase with the velocity. In this circumstance, the control command will lock the floater whereas the floater should be released. Consequently, the energy absorption drops with the phase deviation.

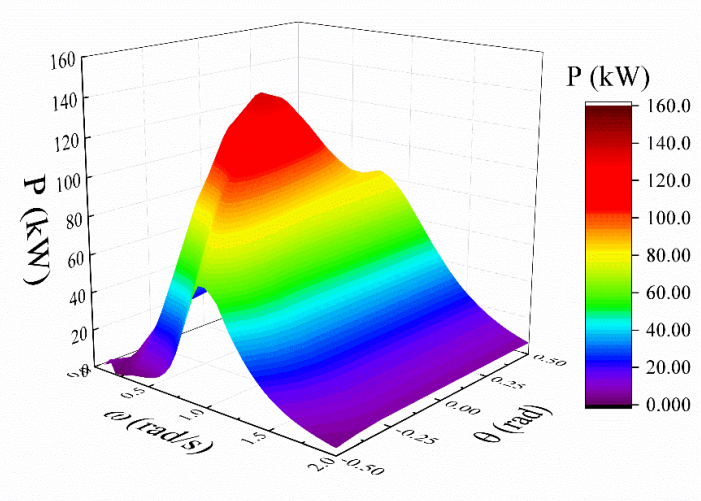

Figure 6-19. Influence of phase deviation on the energy absorption, A = 1 m, τ = 0.2T.

Figure 6-20 shows the influence of phase deviation on the control command. Compared with that in Figure 6-18, the control command is very sensitive to the phase deviation. When the phase deviation expands, the latched duration shrinks indicating that the control action becomes weaker. In this circumstance, the velocity phase is only tuned slightly. Moreover, the latching action is applied earlier than it should be with the consideration of phase deviation. It implies that the WEC is locked when it should be released. Due to these factors, the efficiency of the real-time control is reduced with the phase deviation.

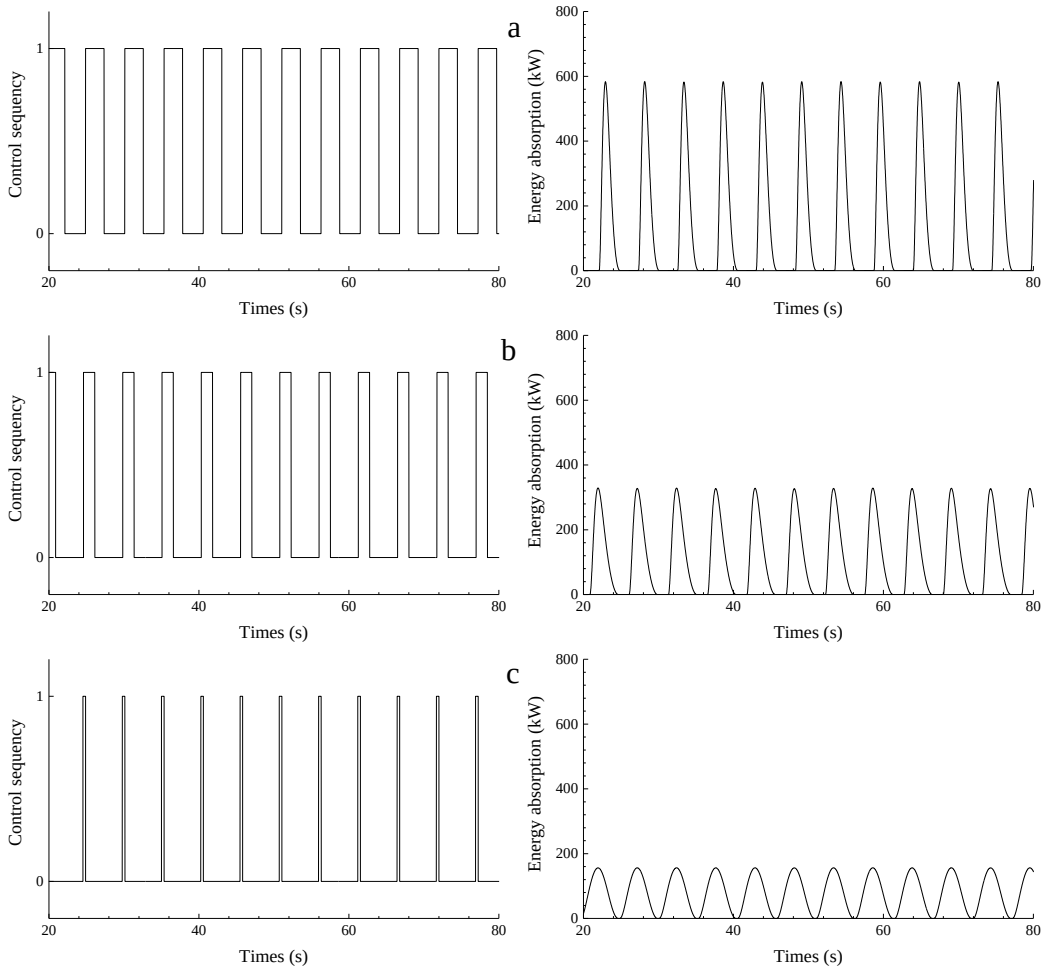

Figure 6-20. Influence of phase deviation on energy absorption, ω = 0.6 rad/s. (a) θ = 0; (b) $\theta = \pi/4$; (c) $\theta = \pi/2$.

According to the above simulation results, long receding horizon is beneficial to the energy absorption whereas the prediction deviation has a negative effect. In practice, the prediction deviation does not follow Eq. (6.3). Instead, the prediction deviation is dependent on the prediction model and the receding horizon. Given a certain prediction

model, the error accumulates over the receding horizon. Consequently, one have to face the trade-off between the receding horizon length and the prediction deviation. Figure 6-21 demonstrates the effect of the receding horizon (including the prediction deviation) on the energy absorption in random waves. When a short receding horizon of 1 s is applied, the prediction deviation is limited and thereby the energy absorption with and without prediction deviation is nearly identical. As pointed out in Chapter 6.4, a larger receding horizon length is beneficial to the energy absorption. Consequently, the point-absorber harvests more energy when the receding horizon length is increased to 2 s even if the prediction deviation becomes larger. As the prediction deviation accumulates with the receding horizon, discrepancies appear between the results with and without prediction deviation. The control with prediction deviation underestimates the power absorption. In the case of larger prediction deviation, the discrepancies with and without prediction deviation become more notable. It suggests that one should be careful with the selection of receding horizon when applying the real-time control to a realistic WEC. For the random waves considered in this study, a duration equal to 2.5 s is the optimal choice. That is why a receding horizon of 2.5 s is used in Chapter 6.3. Please note that this value may vary when a different wave force prediction model is applied.

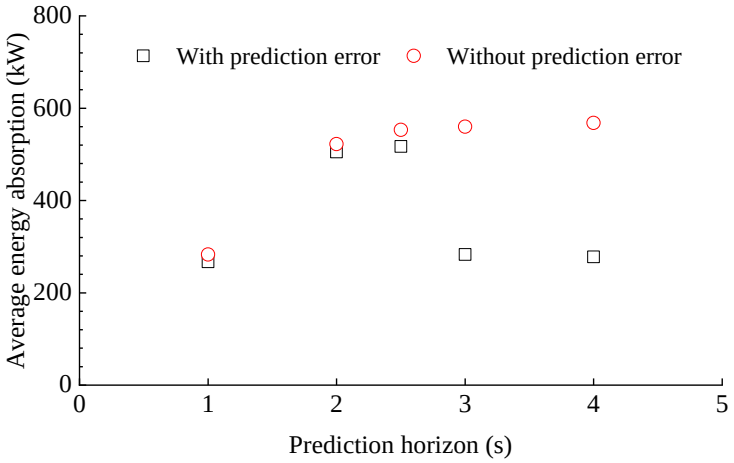

Figure 6-21 Energy absorption with different predictive horizons, Case3

6.6. Summary

The real-time smart controller is implemented to the heaving point-absorber to maximize its energy absorption. Investigations in both regular and irregular waves

indicate that the real-time controller indeed enhances the energy absorption substantially. By carefully checking the velocity and the wave forces, it is found that the controlled velocity is always in phase with the wave forces. Consequently, the wave forces always accelerate the floater so that it carries much more kinetic energy. As interpreted in Chapter 4.3, the real-time controller just maximizes the energy absorption over the receding horizon, and thereby it is sub-optimal. Even so, the control efficiency is still satisfactory, just approximately 10% lower than the optimal control (the theoretical limit). However, the latching control is not effective within the high-frequency range. This is because the un-controlled velocity is nearly in phase with the wave force so that is it is not necessary to apply the latching control anymore.

Since the energy absorption is maximized over the receding horizon, the length of the receding horizon will have an influence on the control performance. The energy absorption increases with the receding horizon. The variation trend can be approximated by the sigmoid function. When the receding horizon is very short, the energy absorption remains at the controlled level. The energy absorption is most sensitive to the moderate receding horizon length and remains stable within long receding horizon range. It indicates that the real-time control efficiency is satisfactory even if the receding horizon is not long.

Since the control command is derived on the basis of the predicted wave forces whereas the point-absorber is subject to the real wave forces, the prediction error will lead to the inappropriate control command. It is shown that the amplitude error has a very little influence on the energy absorption since the latching control is a phase control. On the contrary, the phase error reduces the energy absorption substantially. In the presence of phase error, the floater is locked and released at the wrong time instants. Since the prediction deviation accumulates over the receding horizon, a moderate receding horizon length is recommended in the practical application.

7. Control Effect on Extreme Response and Fatigue Damage Load

7.1. Introduction

From the energy absorption point of view, the control goal is to amplify the floater movement as much as possible in order to maximize the energy absorption. In that case, the PTO force will increase accordingly, probably exceeding the ultimate strength. In the meanwhile, the cyclic wave loads produce fatigue damage to the PTO system. The fatigue may become more serious with the latching control. Therefore, this chapter investigates the control effect on the structural integrity of the PTO system, in terms of short-term extreme response, short-term fatigue damage, and long-term limit state at survival mode.

In the real oceans, the sea state over a short period can be assumed constant. the up-crossing rate method [100] will be used to evaluate the short-term extreme PTO force. The up-crossing rate is a stochastic description of the extreme response, representing the frequency of the response exceeding a pre-given level. This approach has been widely used by researchers to examine the short-term extreme response of the offshore structure. Cheng et al. [101] compared the extreme structural response of a horizontal axis floating wind turbine and a vertical axis floating wind turbine. Li et al. [102] adopted the same approach in their estimation of the extreme response of an integrated floating wind turbine.

Fatigue is the weakening of a material caused by repeatedly applied loads. It is the progressive and localized structural damage that occurs when a material is subjected to cyclic loading. The nominal maximum stress values that cause fatigue damage may be much less than the ultimate strength of the material. Fatigue analysis approach can be categorized into two groups. The first group is the crack propagation theory, which is a very detailed description of how the fatigue grows. The second one is the famous S-N curve method, which plots the magnitude of a cyclic stress against the logarithmic scale of cycles to failure. By applying the S-N curve, it is assumed that the fatigue damage accumulates with each load cycle. Li et al. [103] investigated the fatigue

analysis for the tower base of a spar-type wind turbine. The effects of simulation length, wind-wave misalignment on the fatigue damage were studied. Marino et al. [104] investigated the fatigue loads of a floating wind turbine with both linear and non-linear wave models. The S-N curve method will be used in Chapter 7.3 to estimate the short-term fatigue damage load.

The sea state during the life cycle of an offshore structure varies so that the short-term approach is no longer valid in the estimation of long-term extreme response. Therefore, a distribution model of the waves must be developed at first. The long-term analysis integrates the short-term response with a given environmental distribution model to value the lifetime values, which is the basic idea of the so-called full long-term analysis (FLTA). Coe et al. [105] performed a full long-term analysis of the dynamic responses of a WEC. The FLTA requires massive simulations of short-term response to cover every combination of environmental parameters. It is inefficient, and many alternative methods have been developed. Winterstein et al. [106] introduced an inverse first-order reliability method (IFORM). The IFORM is based on the transformation between a standardized normal space and a physical space. All the possible combinations of variables at a given return period are firstly identified in the normal space and transformed back to the physical space again. The critical environmental condition is selected from the contour surfaces, which are the combinations of the transformed variables. Xiang and Liu [107] used the IFORM to predict the probabilistic fatigue life. A further simplification of the IFORM is the so-called environmental contour method (ECM), which ignores the variability of the response and assumes that the critical environmental condition locates on the *N*-year contour surface. As not many simulation realizations are required, the ECM has been widely used to estimate the extreme response induced by wave loads. Muliawan et al. [108] used the ECM to predict the long-term load of a floating WEC. In Chapter 7.4, the ECM will be used to evaluate the long-term extreme PTO force at the survival mode.

7.2. Short-term extreme response

The short-term extreme PTO force is estimated based on the mean up-crossing rate method. In an arbitrary time interval [0, *T*], it can be assumed that the random number of up-crossing is approximated by the Poisson distribution. Once a pre-given level *y* is selected, the distribution of extreme value y_{max} for a random signal *y*(*t*) is described as

$$P(y_{\max} \le y) = \exp\left(-\int_0^T v^+(y,t)dt\right) \tag{7.1}$$

where $v^+(y,t)$ is the up-crossing rate corresponding to level *y*, which denotes the instantaneous frequency of the positive slop crossings of the defined level. In this circumstance, the probability of y_{max} exceeding the defined level *y* is given by

$$\begin{aligned} P(y_{\max} > y) &= 1 - \exp\left(-\hat{v}^+(y)T\right) \\ \hat{v}^+(y) &= \frac{1}{T}\int_0^T v^+(y,t)dt \end{aligned} \tag{7.2}$$

The mean up-crossing rate $\hat{v}^+(y)$ can be easily obtained from the time series of the signal that is going to be analysed. For example, if there are *k* independent realizations of the random process and let $n_j^+(y,T)$ denote the number of up-crossings in realization *j*, then the sample-based mean up-crossing rate is given by

$$\begin{aligned} \hat{v}^+(y) &\approx \overline{v}^+(y) \\ \overline{v}^+(y) &= \frac{1}{kT}\sum_{j=1}^{k} n_j^+(y,T) \end{aligned} \tag{7.3}$$

Eq. (7.3) is the basic formula to approximate the mean up-crossing rate $\hat{v}^+(y)$ through numerical simulations. If the defined level *y* is not very high, then just a few simulation realizations of the random process will produce a satisfactory approximation. Otherwise, extensive simulations are required to evaluate the extreme values in the tail region. To save computation resources, the extrapolation method proposed by Naess and Gaidai [109] is used in this thesis to predict the mean up-

crossing rate corresponding to a high level y. The extrapolation method is based on the observation of marine structures so that it is applicable in this thesis. The mean up-crossing rate is approximated by

$$\begin{aligned} &\overline{v}^{+}(y) \approx v_{fit}^{+}(y) \\ &v_{fit}^{+}(y) = q \cdot \exp\left\{-a(y-b)^{c}\right\}, y \geq y_0 \end{aligned} \tag{7.4}$$

where q, a, b and c are all constant values. The mean square error Θ is introduced

$$\Theta = \sum_{j=1}^{N} \left| \log\left(\overline{v}^{+}(y_j)\right) - \log(q) + a(y_j - b)^{c} \right|^2 \tag{7.5}$$

The least square method is used to obtain q, a, b and c by minimizing Θ.

Figure 7-1 to Figure 7-3 plot the extrapolated up-crossing rate of the 1-hr short-term extreme PTO force. Regardless of the sea states, the up-crossing rate of extreme PTO force is increased substantially by the real-time controller, implying that the extreme PTO force has a higher probability to exceed a certain level. For example, the up-crossing rate corresponding to 600 kN is 5.93×10^{-4} in Case1 whereas this value jumps to 3.14×10^{-2} with the real-time. It seems that the real-time controller exposes the PTO system to more loads when it tries to maximize the energy absorption.

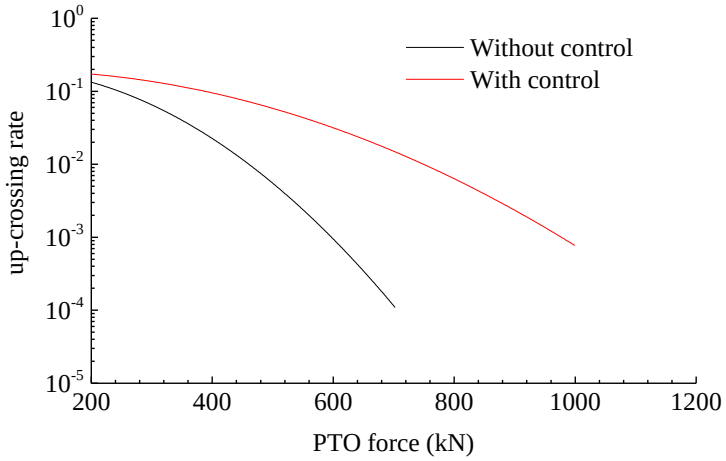

Figure 7-1 Extrapolated up-crossing rate of PTO force, Case1.

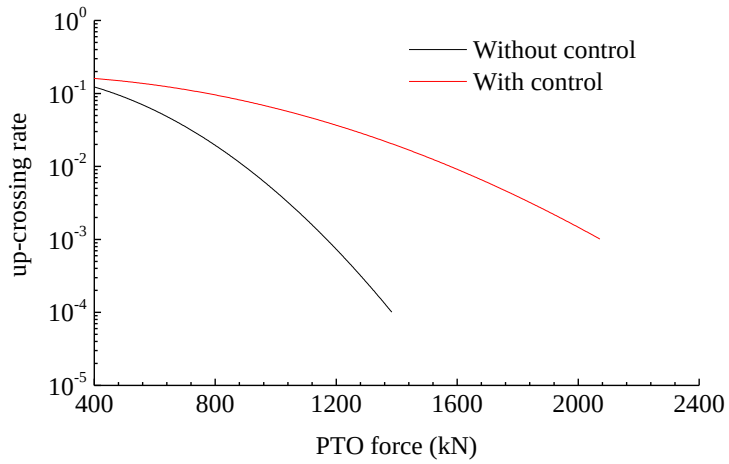

Figure 7-2 Extrapolated up-crossing rate of PTO force, Case2.

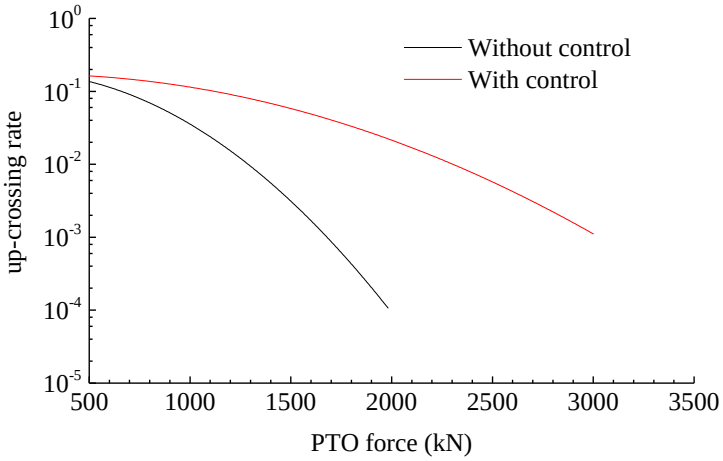

Figure 7-3 Extrapolated up-crossing rate of PTO force, Case3

7.3. Short-term fatigue damage load

The short-term fatigue damage is estimated using the fatigue analysis software package MLife developed by National Renewable Energy Laboratory [110]. The fluctuating PTO loads are broken down into individual hysteresis cycles by matching local minima with local maxima in the time series, which are characterized by a load-mean and range. It is assumed that the damage accumulates linearly with each of these cycles according to Miner's Rule. In this case, the overall damage rate produced by all the cycles is given by

$$DR = \sum_i \frac{n_i}{N_i(L_i^{RF})} / T$$
$$N_i(L_i^{RF}) = \left(2 \cdot \frac{L^{ult} - \left| L^{MF} \right|}{\left(L_i^{RF} \right)} \right)^m \tag{7.6}$$

n_i is the damage count, N_i is the number of cycles to failure, L_i^{RF} is the cycle's load range corresponding to the fixed load-mean L^{MF}, L^{ult} is the design ultimate load and m is the Whöler exponent. When the damage rate accumulates to 1, the structure failure occurs. It is assumed that the interface between the generator and the buoy is a cylinder with a radius of 0.5 m and the yield limit is 235 MPa (a typical value for steel). Therefore, the design ultimate load is around 188 kN (235MPa×π×0.25m^2=188 kN). The value of m is based on DNV design standard [111]. Considering the load type applied at the PTO system, the B1 S-N curve is selected. Since this thesis just assesses the short-term fatigue damage so that the total load cycles are less than 10^7. Give these factors, the Whöler exponent m = 4 is recommend by the DNV design standard [111].

Table 7-1 summarizes the short-term fatigue damage rate of the PTO system in several sea states. When the sea state becomes severe, the heaving point-absorber is subject to more sea waves loads and the amplitude of PTO cyclic loads are augmented as a result. Therefore, the PTO system failure is more likely to occur. The fatigue damage rate is increased substantially by the implementation of the real-time control. As presented previously, the dynamic response of the point-absorber is increased by the real-time control so that the fatigue damage accumulates more quickly when the response is controlled.

Table 7-1 Fatigue damage rate

	Case 1	Case 2	Case 3
Without control	3.64×10^{-10}	2.65×10^{-9}	7.60×10^{-9}
With control	1.30×10^{-9}	1.14×10^{-8}	3.44×10^{-8}

7.4. Long-term limit state at survival mode

In the severe sea states, the WEC will enter the survival mode to ensure the survivability of the structure. One of the survival strategies is to submerge the floater

below the sea and prevent it from oscillating. In the survival mode, the WEC is locked and stops to operation. In this thesis, this survival strategy is adopted. As shown in Figure 7-4, the floater is submerged 8 m below the sea level in the survival state.

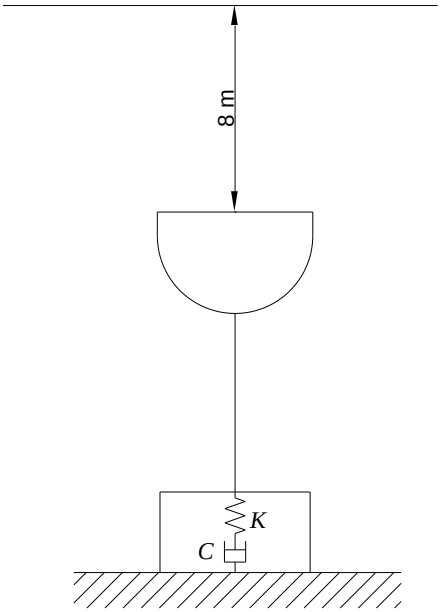

Figure 7-4 Survival state.

The ECM is used here to examine the long-term extreme PTO force at the survival mode. The ECM is aimed at selecting the most important environmental condition, namely the essential combination of environmental parameters, located on the contour line with a desired *N*-year return period. In this thesis, the 1-hr short-term CDF (cumulative distribution function) is used to extrapolate the *N*-year long-term CDF [112]

$$F_{N-year}^{LT}(x)=\left[F_{1-hr|H_s,T_p}^{ST}(x|h_N,t_N)\right]^{N\times 365.25\times 24} \tag{7.7}$$

(h_N, t_N) is the environmental parameter leading to the largest extreme response in the *N*-year return period contour line. The generation of the environmental contour line is based on the Rosenblatt transformation, which transforms the environmental parameter X from the initial X-space into a nonphysical U-space (see Figure 7-5).

$$U=T_2(T_1(X)) \tag{7.8}$$

$$T_1 : Y = \begin{pmatrix} F_1(x_1) \\ \cdots \\ F_{n-1|1,\ldots,n-2}(x_{n-1} \,|\, x_1, \ldots, x_{n-2}) \\ F_{n|1,\ldots,n-1}(x_n \,|\, x_1, \ldots, x_{n-1}) \end{pmatrix} \tag{7.9}$$

$$T_2 : U = \begin{pmatrix} \Phi^{-1}(y_1) \\ \cdots \\ \Phi^{-1}(y_{n-1}) \\ \Phi^{-1}(y_n) \end{pmatrix} \tag{7.10}$$

$F_{n|1,\ldots,n-1}(x_n \,|\, x_1, \ldots, x_{n-1})$ is the conditional cumulative distribution function of environmental parameter x_n at given environmental parameters (x_1, x_2,…, x_{n-1}). Φ is CDF of the standard normal distribution. For the study in this thesis, the involved environmental parameters are H_s and T_p so that Eq. (7.9) and Eq. (7.10) reduce to

$$T_1 : Y = \begin{pmatrix} F_1(H_s) \\ F_{2|1}(T_p \,|\, H_s) \end{pmatrix} \tag{7.11}$$

$$T_2 : U = \begin{pmatrix} \Phi^{-1}(y_1) \\ \Phi^{-1}(y_2) \end{pmatrix} \tag{7.12}$$

Once again, the joint distribution model of stochastic waves proposed by Li et al. [99] is used here. Please refer to Eq. (6.1) and Eq. (6.2) for the details of the joint wave model.

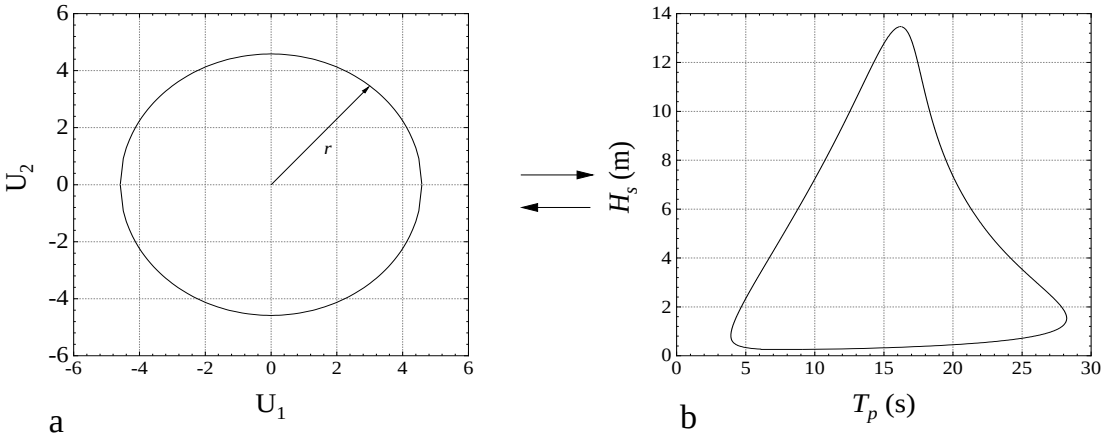

Figure 7-5. Rosenblatt transformation. (a) U-space; (b) X-space.

In the U-space, all combinations of transformed environmental parameters with respect to *N*-year return period are located on a sphere with radius *r*

$$r = \Phi^{-1}(1 - \frac{1}{N \times 365.25 \times 24}) \tag{7.13}$$

Then the environmental contour line can be obtained by transforming the sphere back to the U-space. The procedures of ECM are outlined in Figure 7-6.

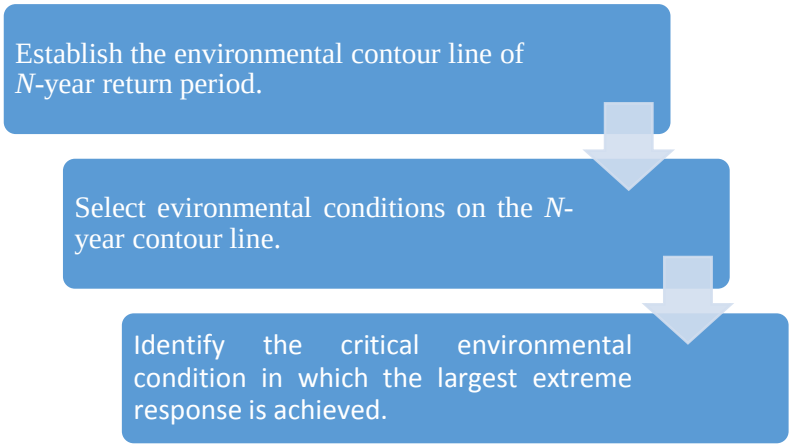

Figure 7-6. Procedures of ECM.

Given that the critical environmental condition has been identified by the ECM, a certain amount of simulations are required to extrapolate the CDF of short-term extreme value $F^{ST}_{1-hr|H_s,T_p}(x|h_N,t_N)$. Assuming that the short-term extreme PTO force converges to the Gumbel distribution

$$F^{ST}_{1-hr|H_s,T_p}(x|h_N,t_N) = \exp(-\exp(-(x-\mu)/\sigma)) \tag{7.14}$$

Then the most probable long-term extreme value corresponding to *N*-year return period is given by Eq. (7.15)

$$M_{N-year} = \mu + \sigma \ln\left(N \times 365.25 \times 24\right) \tag{7.15}$$

One way to examine whether sufficient simulation realizations are performed is to check the 95% confidence interval. Assuming that the errors of the extreme values are normally distributed, the confidence interval is given by

$$M_{CI\pm}(n) = \hat{M}(n) \pm t_{2.5\%,n}\sqrt{std(\hat{M}(n))/n} \tag{7.16}$$

where $\widehat{M}$ is the estimated extreme PTO force based on n simulation realizations. $t_{2.5\%,n}$ is the 97.5% factile value Student's t-distribution with n degrees of freedom. A parameter CI is introduced to value whether the number of realizations is sufficient

$$CI(n) = \frac{\hat{M}_{CI+}(n) - \hat{M}_{CI-}(n)}{\hat{M}(n)} \tag{7.17}$$

It is found that estimating μ and σ by Eq. (7.14) directly requires a huge amount of simulation realizations to acquire satisfactory approximation. Therefore, Eq. (7.14) is transformed into a linear equation and re-written by Eq. (7.18).

$$x = \sigma\left\{-\ln\left[-\ln\left(F^{ST}_{1-hr|H_s,T_p}(x|h_N,t_N)\right)\right]\right\} + \mu \tag{7.18}$$

Figure 7-7 displays the estimation of parameters μ and σ for the extreme PTO force with respect to 20-year return period (N = 20). Different numbers of simulation realizations are examined, and the results are listed in Table 7-2. As shown, 300 simulation realizations are sufficient to produce a reliable prediction. Therefore, the following extreme responses presented in this thesis are based on 300 simulation realizations.

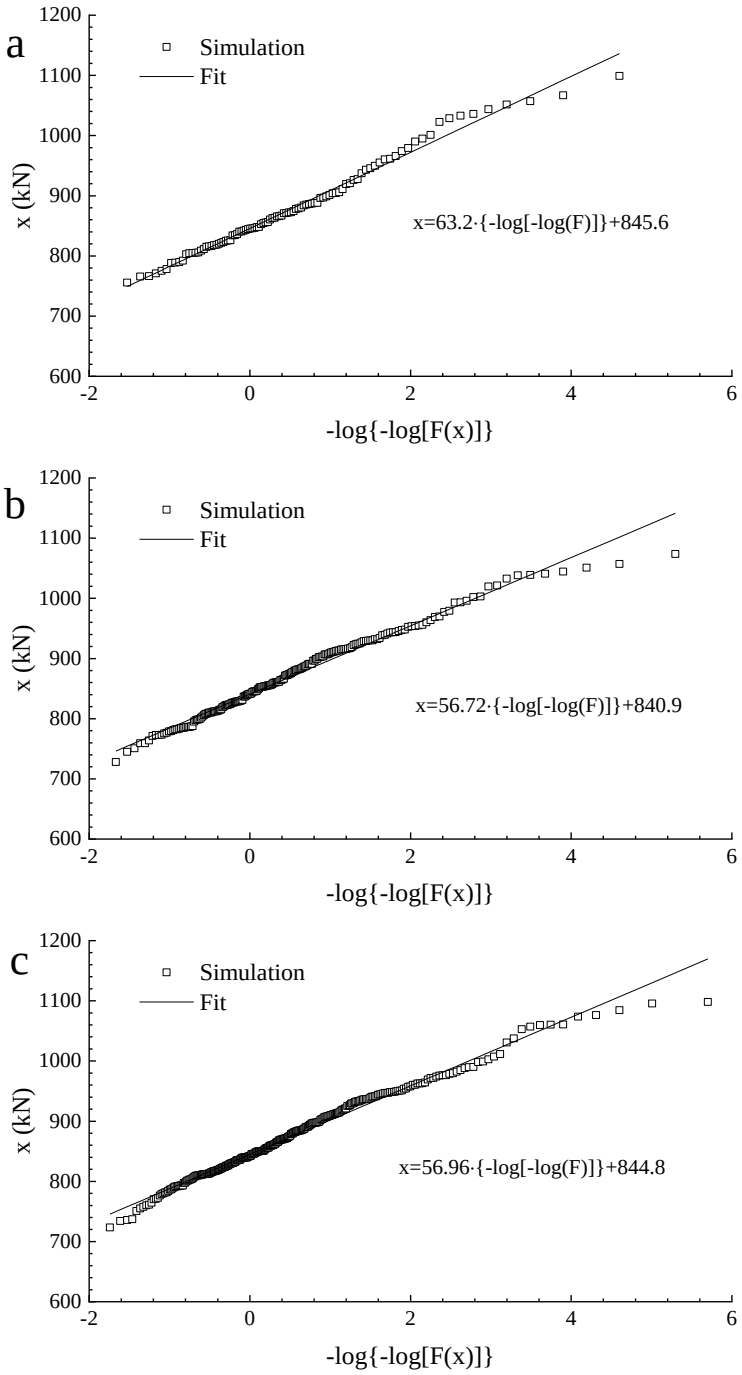

Figure 7-7. Estimation of parameters μ and σ for PTO force. (a) 100 realizations; (b) 200 realizations; (c) 300 realizations.

Table 7-2. *CI* with different number of simulations realizations.

n	μ	σ	CI
100	845.6	63.2	4.4%
200	840.9	56.72	3.3%
300	844.8	56.96	2.8%

Based on the estimated μ and σ, Figure 7-8 plots the CDF of 20-year extreme PTO force. The most possible 20-year extreme PTO force is 1532 kN according to Eq. (7.15).

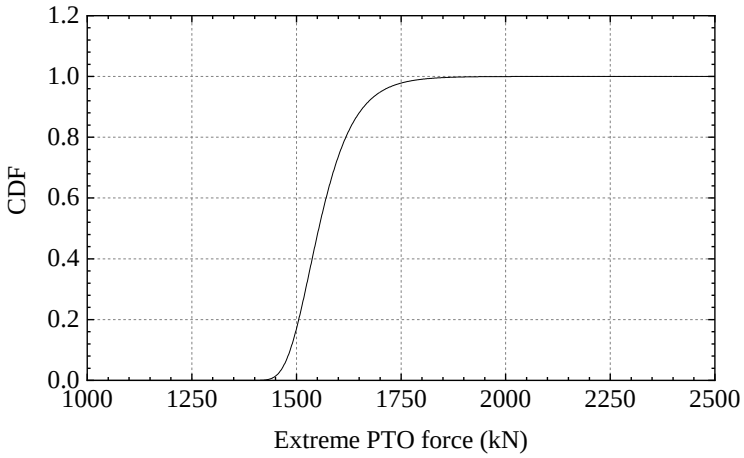

Figure 7-8 CDF of 20-year extreme PTO force

7.5. Summary

It has been demonstrated in the previous chapter that the energy absorption of the heaving point-absorber is increased with the application of the real-time latching control, which is desirable to see. This chapter investigates the structural response of the PTO system in the presence of the latching control. The short-term extreme response, short-term fatigue damage, and the long-term response in survival state are examined.

The shorter-term extreme PTO force is estimated using the up-crossing rate method. The up-crossing rate of PTO force is increased substantially when the real-time control is present. It indicates that, while the energy absorption is maximized with the real-time control, the PTO force is more likely to exceed a pre-given level. Short-term fatigue damage is also investigated in this chapter, using the linear S-N curve method and assuming that the accumulation of fatigue damage is linear with the load cycles. The fatigue damage accumulates more quickly with the real-time control.

Although the implementation of the control enhances the energy absorption sufficiently, it has negative influences on the structural responses. It can be interpreted as a trade-off between energy absorption and structural safety. In this thesis, the

priority is put on the energy absorption and neglect the potential structural failure. It is obviously not the case in practice, where the structural safety plays an essential role. It leads to the so-called constraint control, which takes both the energy absorption and the limit state into account.

8. Multi-stable Mechanism

8.1. Introduction

In Chapter 6, the energy absorption of a linear point-absorber is investigated. Since the system is linear, the energy harvesting efficiency is unsatisfactory with the off-resonance range and that's why the real-time latching control is introduced. In addition to the latching control, an alternative approach to enhance the energy conversion efficiency is the multi-stable mechanism.

Although the multi-stable mechanism has been fully examined in the realm of structural vibration, it is investigated inadequately by researchers and experts in the wave energy community. Despite the proposal of various configurations, most of them operate with the single stability mechanism. Even if they can achieve multi-stability, the mechanical configuration is too complicated and may be infeasible to be adopted by an industrial WEC product (see Figure 8-1 and Figure 8-2). In this chapter, a non-linear PTO system with two oblique springs is proposed, which is able to operate with the multi-stable mechanism. The PTO system can be either monostable or bistable just by adjusting the initial configuration of the oblique springs. Correspondingly, the WEC operates with different mechanisms. It will examine whether the multi-stable mechanism can help to enhance the performance of the WEC, in terms of energy capture and bandwidth.

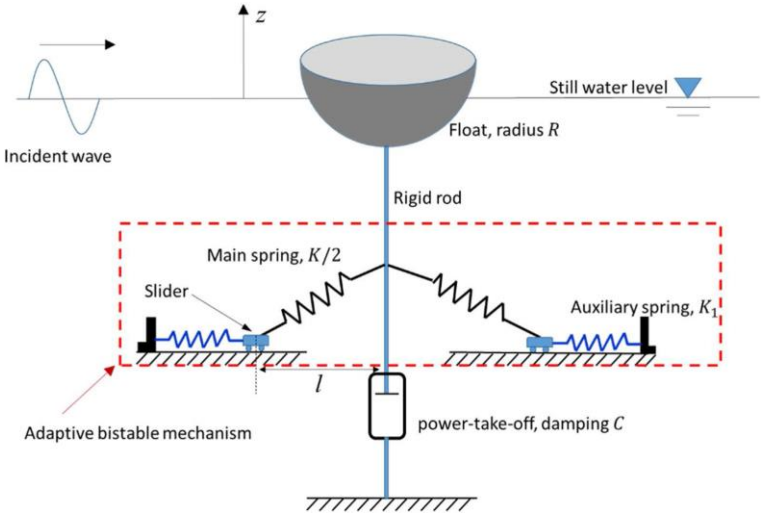

Figure 8-1. The non-linear PTO system proposed by Zhang et al. [75]

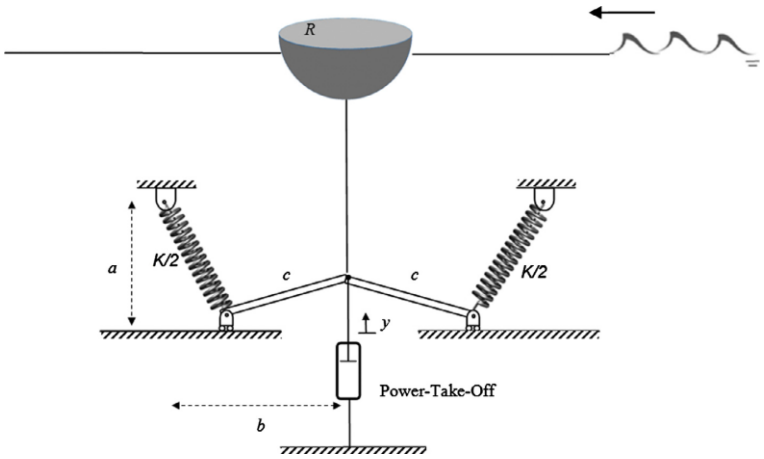

Figure 8-2. The non-linear PTO system proposed by Younesian and Alam [25].

8.2. Static feature of the multi-stable mechanism

As shown in Figure 8-3, the non-linear PTO system is composed of four oblique linear springs and a linear damper. For both PTO systems, the damping coefficient is *C*. The stiffness coefficient of the non-linear PTO system is *k* whereas it is selected as 4*k* for the linear PTO system ($4k = K$, $K = 0.1\rho g\pi R^2$. Refer to Chapter 3.2). The initial position of the WEC refers to that at $\beta_1 = -\beta_2$. Although the non-linear PTO system consists of linear damper and linear springs, both the restoring stiffness (please refer to Figure 8-4) and the potential well (please refer to Figure 8-5) are non-linear since the springs are arranged obliquely. The following part will interpret the non-linear property of the PTO system in detail.

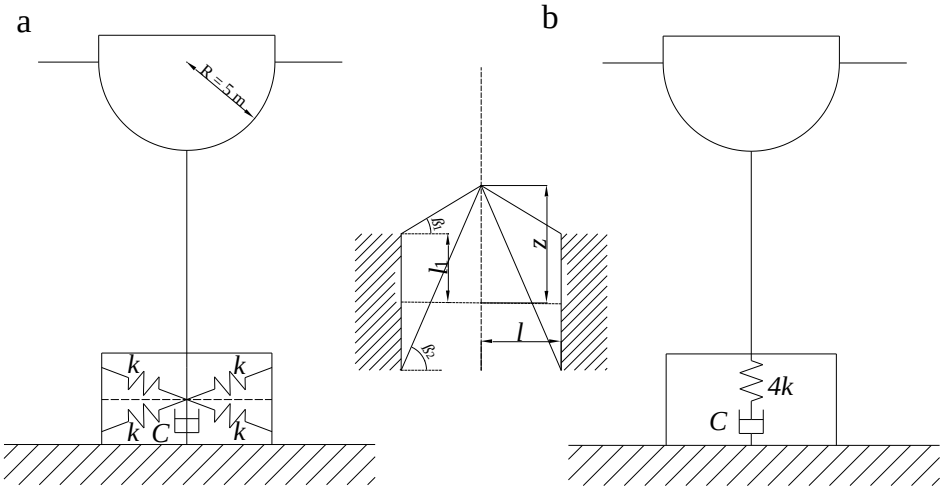

Figure 8-3. The oscillating-buoy point-absorber. (a) with a non-linear PTO system; (b) with a linear PTO system.

Similar to the linear point-absorber, the dynamic model of the non-linear one is expressed as

$$\begin{aligned}&(M+m)\ddot{z}(t)+\int_0^t H(t-\tau)\dot{z}(\tau)d\tau+\rho g\pi R^2 z(t)\\&=F_{wave}(t)-C\dot{z}(t)-2k\left(1-\frac{l_0}{\sqrt{(z-l_1)^2+l^2}}\right)(z-l_1)\\&\quad-2k\left(1-\frac{l_0}{\sqrt{(z+l_1)^2+l^2}}\right)(z+l_1)\end{aligned}\tag{8.1}$$

Once again, define a state vector $\boldsymbol{x}=[z(t),\dot{z}(t),\boldsymbol{u}(t)^T]^T$ with dimension (n+2)×1. Then Eq. (8.1) is re-expressed as

$$\dot{\boldsymbol{x}}=\boldsymbol{\lambda}(\boldsymbol{x})+\boldsymbol{\eta}$$

$$\boldsymbol{\lambda}=\begin{bmatrix}0 & 1 & \mathbf{0}\\ -\dfrac{\rho g\pi R^2+2k\left(1-l_0/\sqrt{(x_1\pm l_1)^2+l^2}\right)}{M+m} & -\dfrac{C}{M+m} & -\dfrac{\boldsymbol{C}}{M+m}\\ \mathbf{0} & \boldsymbol{B} & \boldsymbol{A}\end{bmatrix}$$

$$\boldsymbol{\eta}=\begin{bmatrix}0\\ \dfrac{F_{wave}\pm 2k\left(1-l_0/\sqrt{(x_1\mp l_1)^2+l^2}\right)l_1}{M+m}\\ \mathbf{0}\end{bmatrix}\tag{8.2}$$

According to the configuration in Figure 8-3 (a), the restoring force of the non-linear PTO system is given by

$$\begin{aligned}&F=2k(\sqrt{(z-l_1)^2+l^2}-l_0)\sin\beta_1+2k(\sqrt{(z+l_1)^2+l^2}-l_0)\sin\beta_2\\&\sin\beta_1=\frac{z-l_1}{\sqrt{(z-l_1)^2+l^2}},\sin\beta_2=\frac{z+l_1}{\sqrt{(z+l_1)^2+l^2}}\end{aligned}\tag{8.3}$$

Where l_0 is the initial length of the oblique springs. In this thesis, l_0 is set to 4 m and l_1 is set to 0.1 m. Denote a parameter $\alpha=\sqrt{l_1^2+l^2}/\,l_0$ representing the initial condition

of the oblique springs. The pre-tension of the oblique spring is zero at $\alpha = 1$. When $\alpha > 1$, the four oblique springs are stretched at z = 0. On the contrary, the springs are compressed initially. Figure 8-4 displays the dimensionless restoring force versus dimensionless displacement. The non-linear PTO system has a displacement-dependent restoring force. When the springs are initially stretched, the restoring force always tries to pull the floater back to the equilibrium position. Once $\alpha < 1$, the restoring stiffness is negative within a specific range. Apparently, the PTO system is not stable within this region.

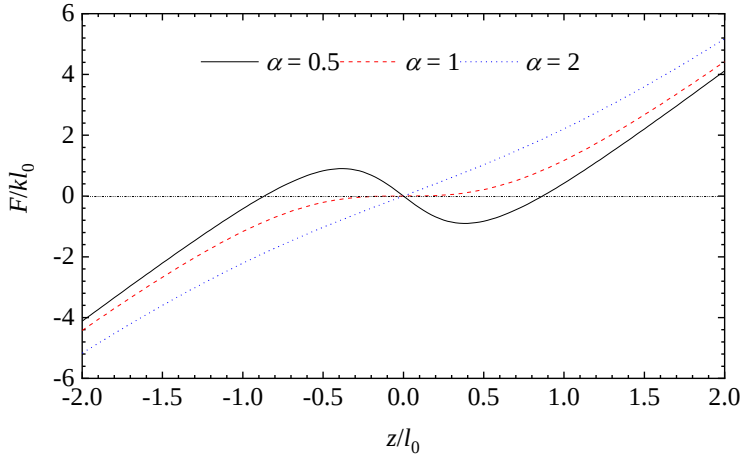

Figure 8-4. Dimensionless restoring force.

For the non-linear PTO system, the potential energy stored in the springs is given by

$$E = k\left[(\sqrt{(z-l_1)^2+l^2}-l_0)^2+(\sqrt{(z+l_1)^2+l^2}-l_0)^2\right] \tag{8.4}$$

The potential energy E with respect to different initial configurations are shown in Figure 8-5. Depending on the initial configuration of the oblique springs, the PTO system is characterized as either monostable or bistable. When $\alpha > 1$, the system has a single equilibrium position and a single potential well. Although the system is non-linear, it behaves in a similar way as the linear PTO system. There is only one type of motion for the floater, which is a sinusoidal-type oscillating motion around the equilibrium position. On the other hand, the non-linear PTO system is bistable with two potential wells at $\alpha < 1$. There are three equilibrium positions. $z = 0$ is no longer a stable position. Once a little external excitation is applied, the floater will move to one

of the other two stable equilibrium positions. Accordingly, there are two types of floater motions. When the sea wave amplitude is small, the floater is trapped within either potential well. If the wave excitation is strong enough, the floater will get across the unstable position, moving around the two potential wells. In this case, the motion of floater may be non-monochromatic even if subject to a sinusoidal wave. It can be seen that the non-linear system behaves with a quite different mechanism.

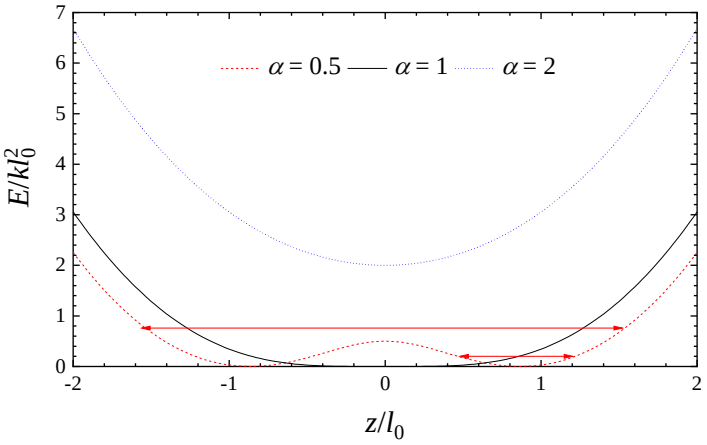

Figure 8-5. Multi-stable mechanism.

In the following part of this chapter, the results are normalized according to

$$P^* = P / \rho g A^2 \tag{8.5}$$

$$\omega^* = \omega / \omega_n, \omega_n = \sqrt{\frac{\rho g \pi R^2 + 4k}{M + m(\infty)}} \tag{8.6}$$

$$C^* = C / C_n, C_n = 2M\omega_n \tag{8.7}$$

8.3. Energy absorption

8.3.1. Monostable mode ($\alpha \geq 1$)

Figure 8-6 shows the power absorption with various initial conditions of the oblique springs in regular waves. The optimal frequency for the two PTO systems is nearly identical regardless of parameter α, which is around $0.5 \cdot \omega_n$. The maximum power output of the linear PTO system is 8.37. Due to the non-linear behaviour of the oblique springs, this value reaches 9.40 at α = 1, increased by 12.5%. At α = 8, the power

capture of the non-linear PTO system is nearly the same with that of the linear one. The Taylor series of the restoring force at $z = 0$ is

$$F(z) = 4kz + 12kl^2 l_0 \left[\frac{1}{\sqrt{\left(l_1^2 + l^2\right)^5}} - \frac{5l_1^2}{\sqrt{\left(l_1^2 + l^2\right)^7}} \right] z^3 + O(z^5) \tag{8.8}$$
$$= K_1 z + K_2 z^3 + O(z^5)$$

where the second term represents the nonlinear effect. When $\alpha = 8$, K_2/K_1 is as low as 0.003. It indicates that the nonlinear component is nearly negligible compared with the linear component. Therefore, the nonlinear system behaves very like the linear one when α increases.

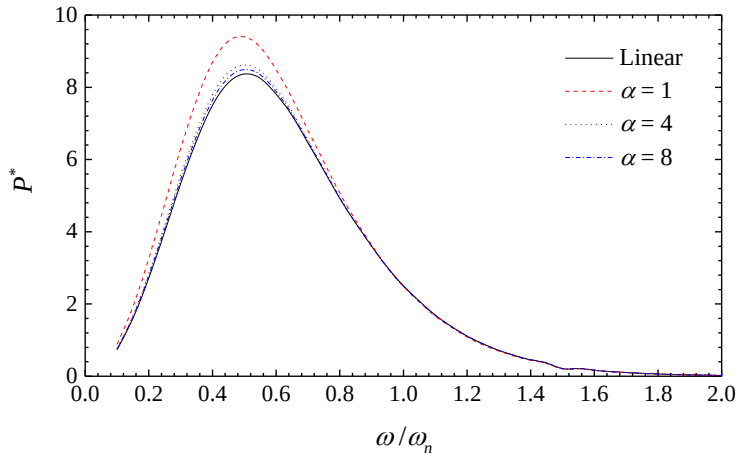

Figure 8-6. Energy absorption at different wave frequencies, A = 1 m, $C = C_n$.

The motions of the floater are plotted in Figure 8-7. Due to the nature of the linear PTO system, the motion is sinusoidal and thereby the phase portrait is an elliptical trajectory. It is interesting to find that the motion of the non-linear WEC is also sinusoidal even if the restoring stiffness is non-linear. The features of motion and phase portrait are very like those of the linear system. According to Figure 8-4, the two oblique springs behave very like the linear one although the restoring stiffness is non-linear. Therefore, the motion of the non-linear WEC is nearly sinusoidal-type.

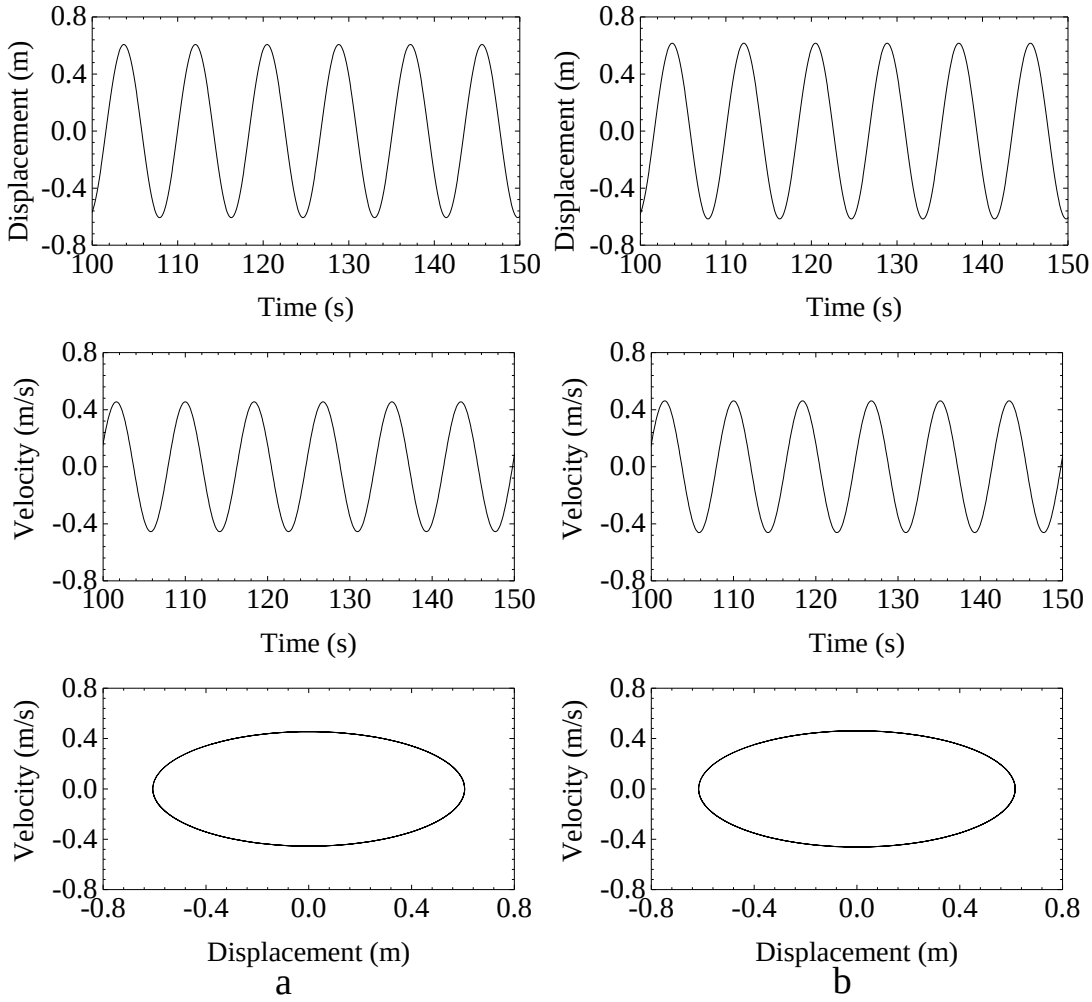

Figure 8-7. Steady motion of the floater, A = 1 m, $\omega = 0.5 \cdot \omega_n$. (a) Linear PTO system; (b) Non-linear PTO system, α = 4;

In a realistic operation condition, the sea waves are always random so that the performance of the WEC may vary considerably. Also, the damping coefficient may be adjusted. Consequently, it is worth investigating how the PTO system performs with different wave frequencies and PTO damping coefficients. Figure 8-8 demonstrates the sensitivity of energy absorption to the two variables. In general, the discrepancies between the linear and non-linear PTO systems are negligible. The non-linear PTO system increases the optimum energy absorption by no more than 14%. Besides, the optimal operation conditions identified are also very close (see Figure 8-9). It suggests that the power capture performances of the two WECs are very similar.

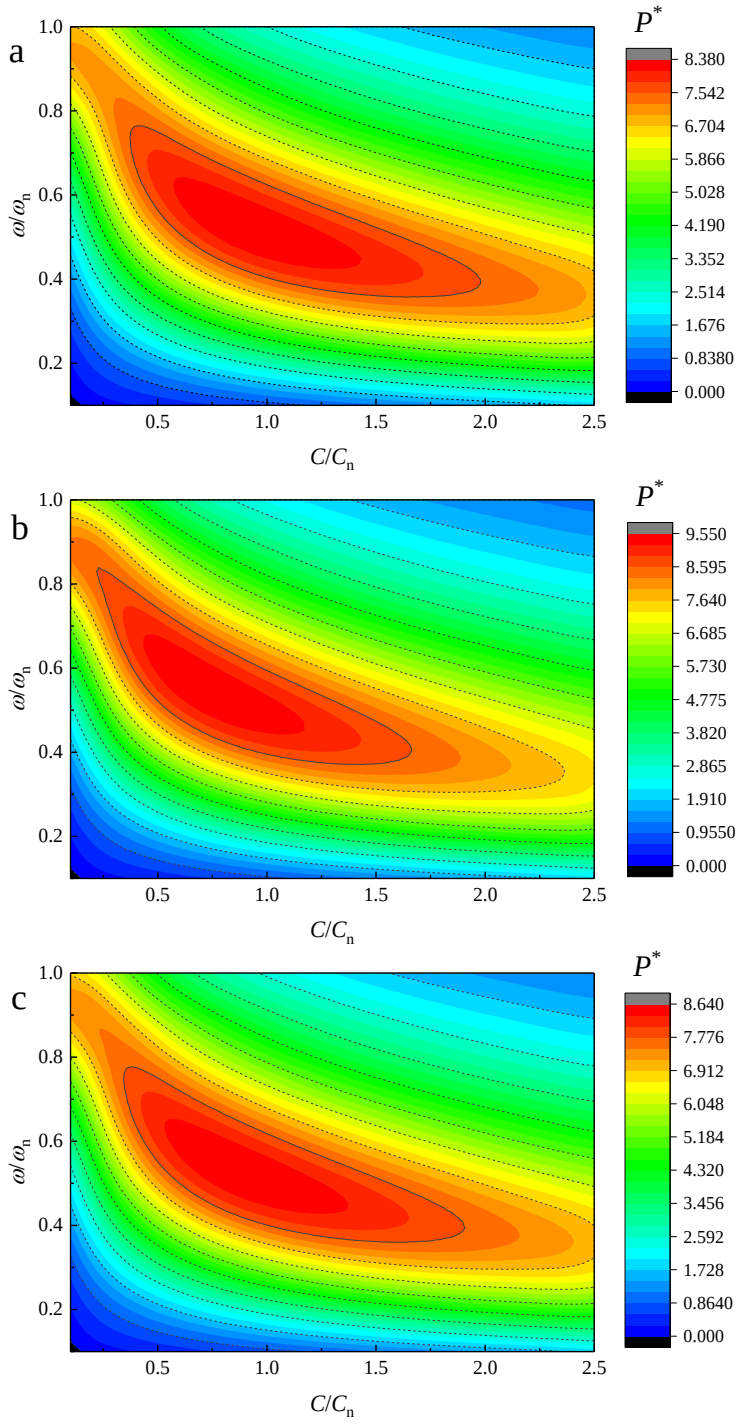

Figure 8-8. Variation of energy absorption with wave frequency and PTO damping, A = 1 m. (a) Linear; (b) Non-linear, α = 1; (c) Non-linear, α = 4.

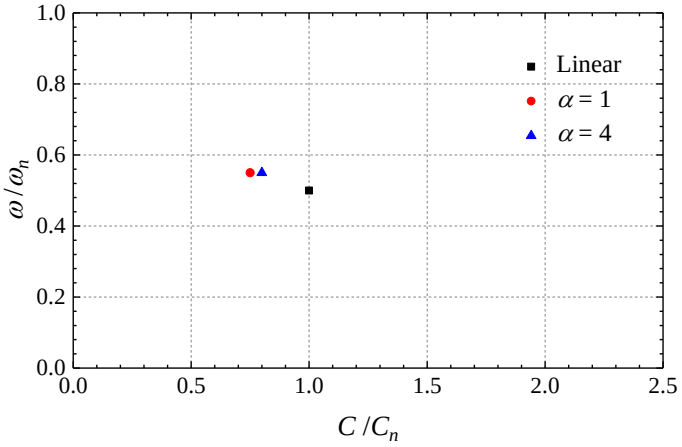

Figure 8-9. Optimum operational conditions.

In order to elaborate the sensitivity of energy absorption to wave frequency and PTO system damping quantitatively, an effective power contour (the solid inner contour in Figure 8-8) is drawn to identify the region within which $P^* > 0.9 \cdot P^*_{\text{optimum}}$ is satisfied. Then, the damping bandwidth (the largest longitude width of the effective power contour) and frequency bandwidth (the largest vertical width of the effective power contour) are introduced. The two parameters represent the sensitivity of energy absorption to the two variables. The damping bandwidth and frequency bandwidth are plotted in Figure 8-10. Checking the geometry of the rectangular, it suggests that both the linear and the non-linear PTO systems are sensitive to the wave frequency whereas relatively robust to the PTO damping. The non-linear PTO system only gives a slightly narrowed damping bandwidth than the linear system whereas the frequency bandwidth is somewhat broadened. It inherently implies that the non-linear WEC may harvest more energy in random waves.

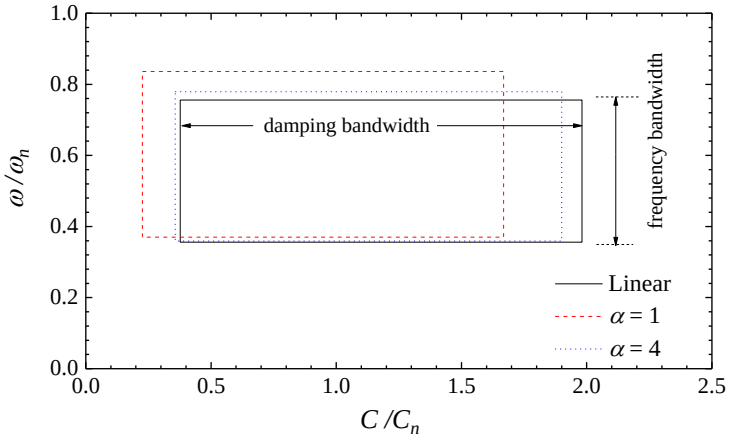

Figure 8-10. Bandwidth.

Table 8-1 compares the total energy absorption in random waves over a 1-hour period when the two comparative PTO systems are used. As shown, the total energy absorption of the nonlinear WEC is just increased slightly by 10% approximately. It is consistent with the results displayed in Figure 8-8.

Table 8-1 1-hour energy absorption, $\alpha = 1$, $C = C_n$.

	Case1	Case2	Case3
Linear	37 kW·h	142 kW·h	303 kW·h
Nonlinear	42 kW·h	162 kW·h	346 kW·h

Based on the above results, the non-linear PTO system seems to work very like the linear one at the monostable mode. Although the restoring stiffness is non-linear, the WEC responds to the wave in a linear way. The energy absorption is just increased slightly. Furthermore, the optimum operation condition and bandwidths of damping and frequency vary hardly compared with those of the linear WEC. Figure 8-5 illustrates that the non-linear PTO system works with a single potential well at the monostable mode, just like the linear one. It explains the similar behaviors of the two WECs.

8.3.2. Bistable mode ($\alpha < 1$)

The non-linear PTO system is bistable when the two oblique springs are compressed initially. This section will examine the performance of the WEC at the bistable mode.

Figure 8-11 demonstrates how the parameter α influences the energy absorption when the PTO damping coefficient is fixed at C_n. As shown, the initial configuration of the two oblique springs has a considerable influence on the energy absorption at the bistable mode. The maximum dimensionless power production increases significantly as α becomes smaller. At the same time, the optimal frequency keeps shifting to a lower value.

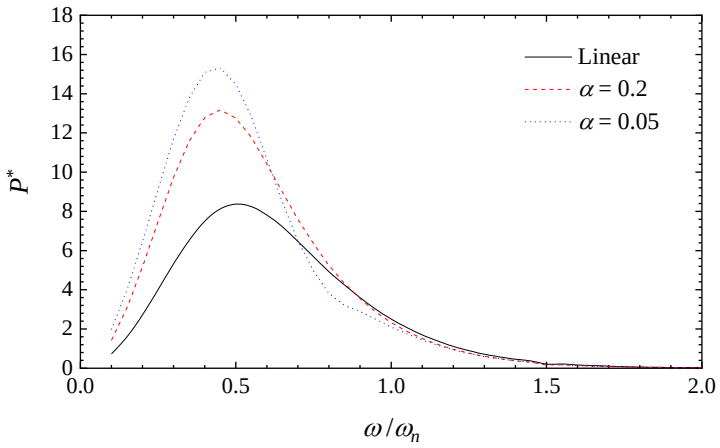

Figure 8-11. Energy absorption at different wave frequencies, A = 1 m, $C = C_n$.

The variation of energy absorption with wave frequency and PTO damping is shown in Figure 8-12. The three contours exhibit notable discrepancies, suggesting that the non-linear PTO system is very sensitive to α. The optimum energy absorption increases from 8.4 to 15.5 with α = 0.2. This value continues increasing and reaches 19.2 at α = 0.05. Besides, the identified optimum operating conditions are far from each other (see Figure 8-13). If the non-linear PTO system can work near its optimum operational condition, the energy harvesting efficiency will be significantly improved.

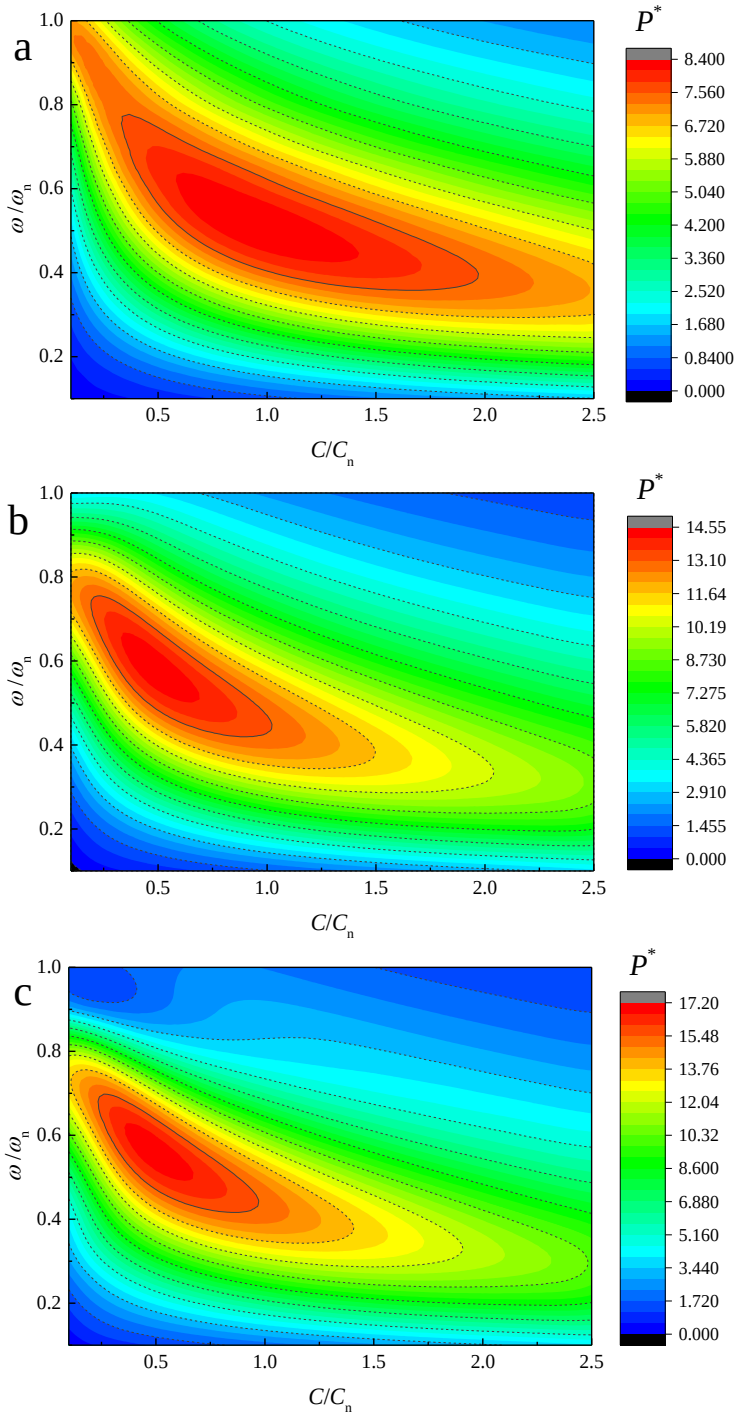

Figure 8-12. Variation of energy absorption with wave frequency and PTO damping, A = 1 m. (a) Linear; (b) Non-linear, α = 0.2; (c) Non-linear, α = 0.05.

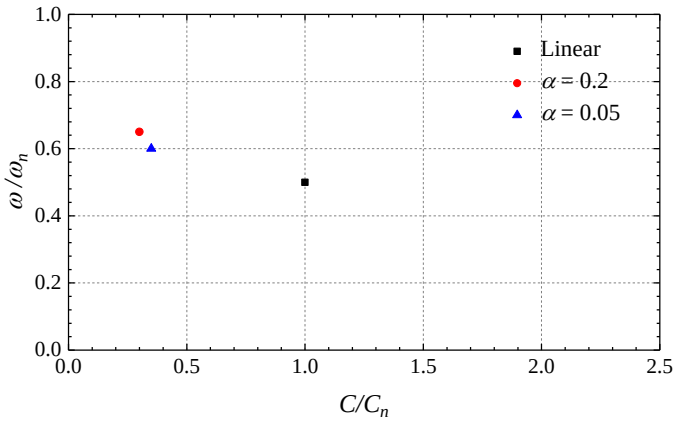

Figure 8-13. Optimum operational conditions.

Figure 8-14 displays the bandwidths of wave frequency and PTO damping. At the monostable mode, the energy absorption responds to the variation of frequency and damping in the same way regardless of the pre-tension of the oblique springs. Comparatively, parameter α has a considerable influence on the sensitivity of energy absorption to the two parameters at the bistable mode. The optimum energy absorption increases significantly when α becomes smaller. At the same time, the bandwidths of frequency and damping are both narrowed implying that the WEC is more sensitive to the variation of environmental conditions. At first sight, the non-linear PTO system is not certain to harvest more energy than the linear one. The bistable mechanism is beneficial to the optimum power production but the effective bandwidth is narrowed at the same time. Investigating the contours in Figure 8-12 quantitatively, it is found that the non-linear PTO system (α = 0.05) gives a larger power output than the linear one in most part of the region considered. Therefore, the non-linear WEC still harvests more energy in random waves even if it is more sensitive to wave frequency.

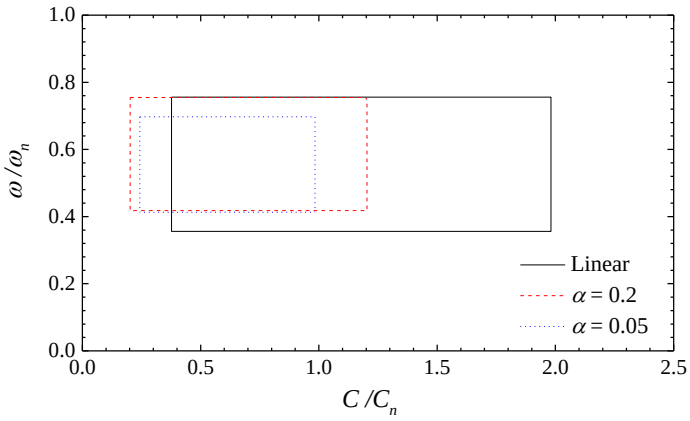

Figure 8-14. Bandwidth.

One may wonder why the energy absorption is increased substantially at the bistable mode. To elaborate the strategy behind, two operational points (C/C_n = 0.5, ω/ω_n = 0.5) and (C/C_n = 2, ω/ω_n = 0.8) are selected and the motions of the floater at the two points are shown in Figure 8-15. It has been shown that the floater motion is sinusoidal-type (see Figure 8-7) at the monostable mode although the PTO system is non-linear. Due to this fact, the non-linear PTO system behaves very like the linear one. Two types of motions are identified at the bistable mode. In Figure 8-15 (a), the floater crosses the unstable equilibrium position (z = 0) and moves around the two potential wells. Although the WEC is subject to sinusoidal wave, the bistable mechanism leads to a non-monochromatic response. Thereby, the phase portrait is not an elliptical trajectory but surrounds around the two equilibrium positions. As shown in Figure 8-4, the restoring stiffness of the two oblique springs is negative within the middle region, implying that the floater is subject to repulsion within this region. Once outside the unstable region, the restoring stiffness of the oblique springs converts positive immediately. Therefore, the velocity is held for a short period rather than continues speeding up. Distinguished from the response at Point 1, the floater motion at Point 2 exhibits new feature. The most remarkable characteristic is that the floater gets trapped within one single potential well. It merely oscillates around the stable equilibrium position and unable to come across the unstable equilibrium position. Meanwhile, the motion is nearly sinusoidal, verified by the elliptical trajectory of the phase portrait which surrounds a single point. One can see that the operating mechanism at Point 2 is nearly identical to that of the linear PTO system and the discrepancy is that the floater is oscillating around a new equilibrium position. It suggests that the WEC operates with the different mechanism at various combinations of wave frequency and PTO damping.

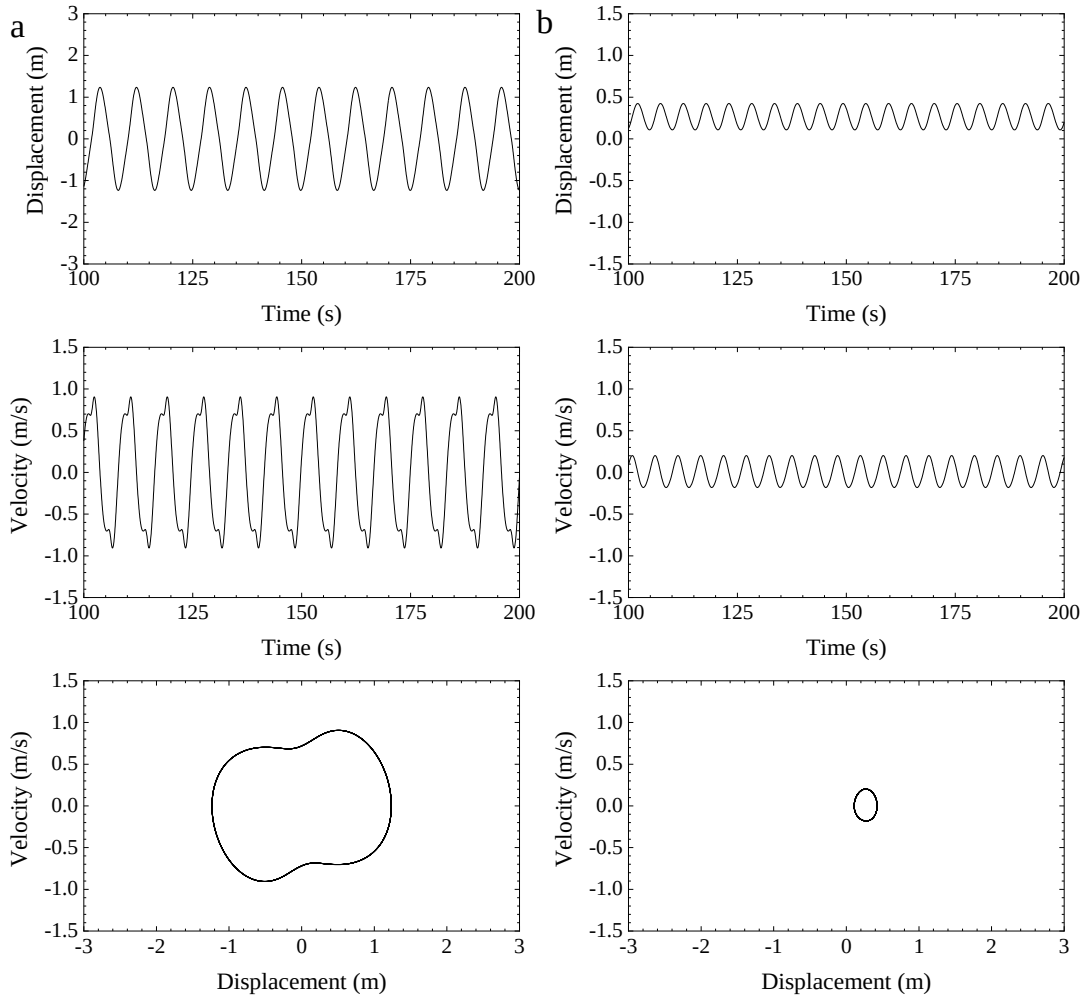

Figure 8-15. Steady motion of the floater, A= 1 m. (a) Point 1; (b) Point 2.

Figure 8-16 displays the phase between floater velocity and wave excitation force. When the floater experiences the unstable region, the velocity is held so that the phase of the velocity is tuned as well. This effect is very like that of the latching control. Owing to the non-linear snap-through, the velocity of the non-linear WEC (α = 0.05) is nearly in phase with the wave force so that the energy absorption is significantly enhanced at Point 1. On the contrary, the PTO operates with a single-well potential without the unstable region at the monostable mode (α = 4). In this circumstance, the tuning of velocity phase is very limited so that the movement of the floater is hardly changed. Please note that this tuning is not always beneficial to the power capture. For example, the non-linear point-absorber (α = 0.05) harvests less energy than the linear one at $C = 0.5C_n$, $\omega = 0.8\omega_n$, meaning that the role of phase tuning is negative. This problem can be addressed by adjusting parameter α from 0.05 to 0.2.

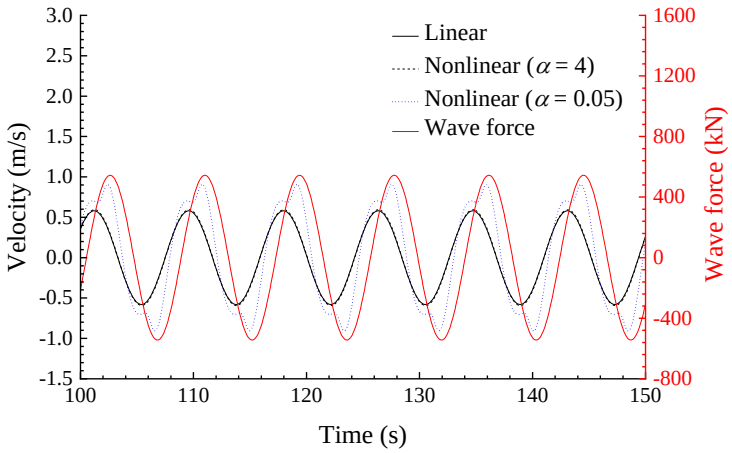

Figure 8-16. The phase between velocity and wave excitation force (Point 1).

Contrary to the response of a linear system, the energy absorption of a non-linear system may not vary linearly with respect to the square of wave amplitude. The influence of wave amplitude on the dimensionless energy absorption is shown in Figure 8-17. Generally, the contours with respect to different wave amplitudes are very similar despite that a larger wave amplitude results in a lower dimensionless energy absorption. By further increasing the wave amplitude, the absolute energy absorption remains relatively stable and thereby the dimensionless energy absorption drops accordingly. Such a saturation phenomenon has been reported by Younesian and Alam [25] and Zhang et al. [15] in their investigations of non-linear PTO systems.

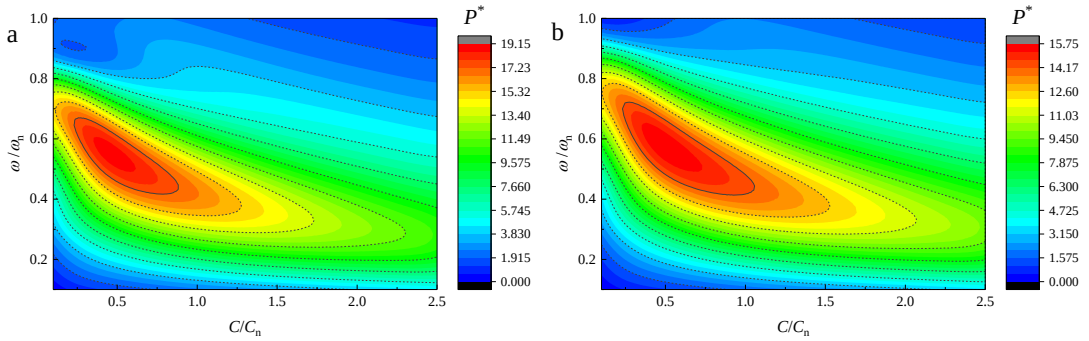

Figure 8-17. Influence of wave amplitude on dimensionless energy absorption, α = 0.05. (a) A =1 m, (b) A = 1.5 m.

The total energy absorbed in random waves is shown in Figure 8-18. Unlike that at the monostable mode, the energy is enhanced substantially at the bistable mode.

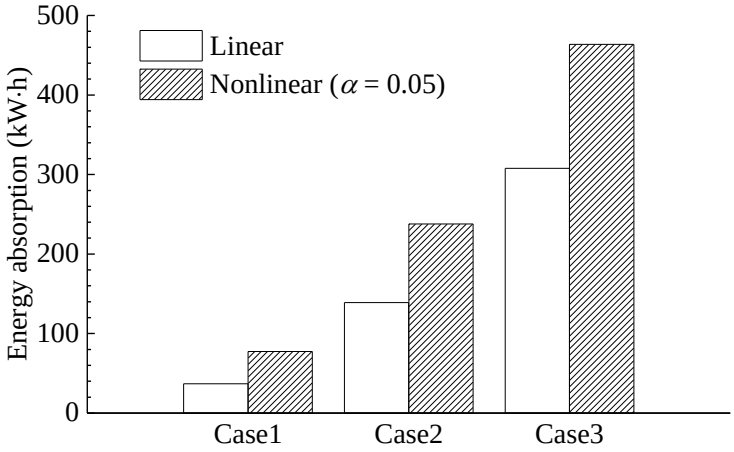

Figure 8-18. Overall energy absorption during the 1-hour period, $C = C_n$.

At the bistable mode, the non-linear WEC behaves quite differently with the linear one. The energy absorption is increased substantially in both regular wave and random waves with the bistable mechanism. In addition, the identified optimum operational condition is far from that of the linear PTO system. The bandwidths of frequency and damping are narrowed implying that the PTO system is more sensitive to the two parameters.

8.4. Summary

In this chapter, the multi-stable mechanism of the point-absorber is investigated by introducing an oblique spring system. Depending on whether the springs are stretched or compressed initially, the system is characteristic of monostable mode or bistable mode.

The system is monostable when the springs are pre-stretched. In this circumstance, the PTO system has a single potential well with one stable equilibrium position and the restoring stiffness of the two springs are always positive. Therefore, the snap-through never happens. Due to this nature, the non-linear WEC behaves very like a linear one. The energy absorption is indeed increased, but just slightly. The identified optimum operation condition also remains relatively stable regardless of parameter α. Besides, the bandwidths of PTO damping and wave frequency are hardly changed by adjusting α. By checking the phase portrait and the time series of floater movement, it

is found that the response of the floater is nearly sinusoidal type. In summary, the non-linear WEC is nearly identical to the linear one in spite of some tiny discrepancies.

The system is bistable when the oblique springs are pre-compressed. At the bistable mode, the PTO system is characteristic of a double-well potential. Accordingly, the system has a non-linear snap-through with an unstable equilibrium position and two stable equilibrium positions. In this circumstance, an unstable region is formed within which the restoring stiffness is negative. At the bistable mode, two types of floater motions are identified. Sometimes, the floater gets trapped in a single well and oscillates around the stable equilibrium position. Occasionally, the floater moves around between the two potential wells if the external excitations are strong enough. Under other condition, the non-linear WEC operates with distinctive mechanism at different operation conditions. It explains why the WEC becomes very sensitive to the wave frequency and PTO damping at the bistable mode. By checking the overall energy absorption under various random wave conditions, the non-linear WEC is proved to harvest more energy. The bandwidths of PTO damping and wave frequency are narrowed.

The enhancement of energy capture is mainly attributed to the tuning of the velocity phase when the floater experiences the unstable region. Simulation results show that the energy absorption is significantly increased when the tuned velocity is in phase with the wave excitation force. Moreover, the tuning of velocity phase is only considerable at the bistable mode when the floater can move between the two potential wells. It is why the power capture is hardly improved at the monostable mode. However, the tuning effect is not always positive. Actually, the non-linear WEC harvests less energy in some operating conditions. A feasible solution to this problem is adjusting the parameter α.

9. Conclusions and Recommendations

9.1. Conclusions

The main conclusions are outlined below:

1. Compared with the traditional deterministic prediction approach, the prediction method in this thesis does not require the dynamic model of the physical process concerned. It is purely determined by the examples of the physical process. Compared with the traditional prediction approach grey model GM(1,1), the current data-driven approach has a better prediction ability.
2. The real-time control algorithm based on the artificial neural network is effective in random waves, even without the knowledge of future wave forces. The control efficiency is close to the theoretical limit.
3. In the absence of prediction error, the energy absorption increases with the prediction horizon and converges to the theoretical limit gradually. It is because the control command is merely derived over the prediction horizon rather than the entire time interval concerned.
4. Since the WEC is subject to the real wave forces whereas the control command is derived on the predicted wave forces, the prediction error will lead to inappropriate control command and has a negative influence on the control performance. This thesis demonstrates that it is the phase error that leads to the poor control efficiency whereas the amplitude error has a small effect.
5. It shows that the extreme force and the fatigue damage load are both increased with the implementation of the real-time control. Since this thesis focuses on the enhancement of energy absorption, the negative effect on structural survivability is temporarily neglected.
6. Depending on the initial condition of the two springs, the non-linear point-absorber proposed in this thesis is either monostable or bistable. The non-linear point-absorber behaves is similar with a linear one in the monostbale model whereas its response feature is quite distinctive in the bistable mode. The system is sometimes trapped within one potential well and sometimes cross the two

potential wells. It is shown that the energy conversion is increased considerably in the bistable mode.

9.2. Recommendations

In this thesis, the linear potential flow theory is used to model the dynamics of the floater in waves and apply unconstraint control to enhance the energy absorption. The present research can be improved in the following three aspects:

1. The linear flow theory is a reasonable approximation of the wave-structure interaction, which neglects the viscous effect and the higher-order components of the waves. The simulation accuracy can be improved by considering the non-linear Froude-Krylov force.
2. The control objective is the maximization of the energy absorption without consideration of the PTO force. According to the simulation results, both the extreme force and the fatigue damage load are increased in the presence of the real-time control. Apparently, this issue must be carefully addressed in the actual case. A solution to this problem is the introduction of the so-called constrained control, which set a limit to the structural load.

References

[1] S.H. Salter, Wave Power, Nature 249(5459) (1974) 720-724.

[2] Wae Dragon ApS, Wave Dragon, 2013. http://www.wavedragon.net/. (Accessed 11 May 2018).

[3] European Marine Eerngy Centre, Pelamis Wave Power, 2018. http://www.emec.org.uk/about-us/wave-clients/pelamis-wave-power/. (Accessed 11 May 2018).

[4] US Departmetn of Energy, Innovative Wave Power Device Starts Producing Clean Power in Hawaii, 2015. https://www.energy.gov/eere/articles/innovative-wave-power-device-starts-producing-clean-power-hawaii. (Accessed 10 December 2018).

[5] R. Genest, J.V. Ringwood, Receding Horizon Pseudospectral Control for Energy Maximization With Application to Wave Energy Devices, Ieee Transactions on Control Systems Technology 25(1) (2017) 29-38.

[6] P.D. Sclavounos, Y. Ma, Wave Energy Conversion using Machine Learning Forecasts and Model Predictive Control, 33st International Workshop on Water Waves and Floating Bodies, Brest, France, 2018.

[7] A. Kurniawan, X. Zhang, Application of a Negative Stiffness Mechanism on Pitching Wave Energy Devices, 5th Offshore Energy and Storage Symposium, 2018.

[8] B.L. Smith, M.J. Demetsky, Short-term traffic flow prediction models-a comparison of neural network and nonparametric regression approaches, Proceedings of IEEE International Conference on Systems, Man and Cybernetics, 1994, pp. 1706-1709.

[9] M.S. Dougherty, M.R. Cobbett, Short-term inter-urban traffic forecasts using neural networks, Int J Forecasting 13(1) (1997) 21-31.

[10] F. Yu, X.Z. Xu, A short-term load forecasting model of natural gas based on optimized genetic algorithm and improved BP neural network, Appl Energ 134 (2014) 102-113.

[11] D.A. Fadare, Modelling of solar energy potential in Nigeria using an artificial neural network model, Appl Energ 86(9) (2009) 1410-1422.

[12] S.A. Kalogirou, Artificial neural networks in renewable energy systems applications: a review, Renew Sust Energ Rev 5(4) (2001) 373-401.

[13] N. Elvin, A. Erturk, Advances in energy harvesting methods, Springer Science & Business Media2013.

[14] M. Lopez, F. Taveira-Pinto, P. Rosa-Santos, Influence of the power take-off characteristics on the performance of CECO wave energy converter, Energy 120 (2017) 686-697.

[15] X.T. Zhang, J.M. Yang, Power capture performance of an oscillating-body WEC with nonlinear snap through PTO systems in irregular waves, Applied Ocean Research 52 (2015) 261-273.

[16] V.G. Boltyanskiĭ, R.V. Gamkrelidze, L.S. Pontryagin, On the theory of optimal processes, Dokl. Akad. Nauk SSSR 110 (1956) 7-10.

[17] ExxonMobile, Outlook for Energy: A View to 2040, 2017.

[18] F. He, Z.H. Huang, A.W.K. Law, An experimental study of a floating breakwater with asymmetric pneumatic chambers for wave energy extraction, Appl Energ 106 (2013) 222-231.

[19] A. Babarit, F. Wendt, Y.H. Yu, J. Weber, Investigation on the energy absorption performance of a fixed-bottom pressure-differential wave energy converter, Applied Ocean Research 65 (2017) 90-101.

[20] Y.L. Zhang, Q.P. Zou, D. Greaves, Air-water two-phase flow modelling of hydrodynamic performance of an oscillating water column device, Renew Energ 41 (2012) 159-170.

[21] D.V. Evans, A.d.O. Falcão, Hydrodynamics of ocean wave-energy utilization, Springer Berlin et al.1986.

[22] L. Margheritini, D. Vicinanza, R. Frigaard, SSG wave energy converter: Design, reliability and hydraulic performance of an innovative overtopping device, Renew Energ 34(5) (2009) 1371-1380.

[23] D. Vicinanza, P. Contestabile, J.Q.H. Norgaard, T.L. Andersen, Innovative rubble mound breakwaters for overtopping wave energy conversion, Coastal Engineering 88 (2014) 154-170.

[24] M. Masubuchi, R. Kawatani, Frequency-Response Analysis of an Ocean Wave Energy Converter, J Dyn Syst-T Asme 105(1) (1983) 30-38.

[25] D. Younesian, M.R. Alam, Multi-stable mechanisms for high-efficiency and broadband ocean wave energy harvesting, Appl Energ 197 (2017) 292-302.

[26] X.T. Zhang, J.M. Yang, L.F. Xiao, An Oscillating Wave Energy Converter with Nonlinear Snap-Through Power-Take-Off Systems in Regular Waves, China Ocean Engineering 30(4) (2016) 565-580.

[27] X.L. Xiao, L.F. Xiao, T. Peng, Comparative study on power capture performance of oscillating-body wave energy converters with three novel power take-off systems, Renew Energ 103 (2017) 94-105.

[28] A. Wells, Fluid driven rotary transducer, in: B.p. spec (Ed.) UK, 1976, pp. 595-700.

[29] B.I. ANDREEVICH, Apparatus for converting sea wave energy into electrical energy, US Patent 3,922,739, 1975.

[30] R. Curran, T. Denniss, C. Boake, Multidisciplinary design for performance: ocean wave energy conversion, The Tenth International Offshore and Polar Engineering Conference, International Society of Offshore and Polar Engineers, 2000.

[31] A.F.D. Falcao, Wave energy utilization: A review of the technologies, Renew Sust Energ Rev 14(3) (2010) 899-918.

[32] AWS Ocean Eerngy. Ltd, Archimedes Waveswing Submerged Wave Power Buoy, 2018.
http://www.awsocean.com/archimedes-waveswing.html.
(Accessed 11 May 2018).

[33] Ocean Power Technologies, PowerBuoy Technology, 2018.
https://www.oceanpowertechnologies.com/powerbuoy.
(Accessed 11 May 2018).

[34] I. Simonetti, L. Cappietti, H. Elsafti, H. Oumeraci, Evaluation of air compressibility effects on the performance of fixed OWC wave energy converters using CFD modelling, Renew Energ 119 (2018) 741-753.

[35] B. Devolder, V. Stratigaki, P. Troch, P. Rauwoens, CFD Simulations of Floating Point Absorber Wave Energy Converter Arrays Subjected to Regular Waves, Energies 11(3) (2018) 641.

[36] O.M. Faltinsen, Sea Loads on Ships and Offshore Structures, Cambridge University Press1993.

[37] J.N. Newman, Marine hydrodynamics, MIT press1977.

[38] W. Cummins, The impulse response function and ship motions, David Taylor Model Basin, Washington DC, 1962, pp. 101-109.

[39] R. Taghipour, T. Perez, T. Moan, Hybrid frequency-time domain models for dynamic response analysis of marine structures, Ocean Eng 35(7) (2008) 685-705.

[40] X.T. Zhang, J.M. Yang, W.H. Zhao, L.F. Xiao, Effects of wave excitation force prediction deviations on the discrete control performance of an oscillating wave energy converter, Ships Offshore Struc 11(4) (2016) 351-368.

[41] D. Son, R.W. Yeung, Real-time implementation and validation of optimal damping control for a permanent-magnet linear generator in wave energy extraction, Appl Energ 208 (2017) 571-579.

[42] J. Hals, J. Falnes, T. Moan, Constrained Optimal Control of a Heaving Buoy Wave-Energy Converter, Journal of Offshore Mechanics and Arctic Engineering 133(1) (2011) 011401-1-011401-15.

[43] A. Babarit, M. Guglielmi, A.H. Clement, Declutching control of a wave energy converter, Ocean Eng 36(12-13) (2009) 1015-1024.

[44] K. Budal, J. Falnes, Interacting point absorbers with controlled motion, in Power from Sea Waves, BM Count, Academic Press1980.

[45] A. Babarit, A.H. Clement, Optimal latching control of a wave energy device in regular and irregular waves, Applied Ocean Research 28(2) (2006) 77-91.

[46] M. Greenhow, S.P. White, Optimal heave motion of some axisymmetric wave energy devices in sinusoidal waves, Applied Ocean Research 19(3-4) (1997) 141-159.

[47] R.E. Hoskin, N. Nichols, Optimal strategies for phase control of wave energy devices, 3th International Symposiumon Wave, Tidal, OTEC, and Small Scale Hydro Energy, Bedford, UK, 1986.

[48] A. Babarit, G. Duclos, A.H. Clement, Comparison of latching control strategies for a heaving wave energy device in random sea, Applied Ocean Research 26(5) (2004) 227-238.

[49] D. Son, R.W. Yeung, Optimizing ocean-wave energy extraction of a dual coaxial-cylinder WEC using nonlinear model predictive control, Appl Energ 187 (2017) 746-757.

[50] G. Li, G. Weiss, M. Mueller, S. Townley, M.R. Belmont, Wave energy converter control by wave prediction and dynamic programming, Renew Energ 48 (2012) 392-403.

[51] J. Hals, J. Falnes, T. Moan, A Comparison of Selected Strategies for Adaptive Control of Wave Energy Converters, Journal of Offshore Mechanics and Arctic Engineering 133(3) (2011) 031101-1-031101-12.

[52] J. Cretel, A.W. Lewis, G. Lightbody, G.P. Thomas, An Application of Model Predictive Control to a Wave Energy Point Absorber, IFAC Proceedings Volumes 43(1) (2010) 267-272.

[53] T.K.A. Brekken, On Model Predictive Control for a point absorber Wave Energy Converter, 2011 IEEE Trondheim PowerTech, 2011, pp. 1-8.

[54] J. Falnes, Ocean waves and oscillating systems: linear interactions including wave-energy extraction, Cambridge university press2002.

[55] J. Falnes, A review of wave-energy extraction, Mar Struct 20(4) (2007) 185-201.

[56] E. Rusu, C.G. Soares, Numerical modelling to estimate the spatial distribution of the wave energy in the Portuguese nearshore, Renew Energ 34(6) (2009) 1501-1516.

[57] M.H. Kazeminezhad, A. Etemad-Shahidi, S.J. Mousavi, Application of fuzzy inference system in the prediction of wave parameters, Ocean Eng 32(14-15) (2005) 1709-1725.

[58] M. Ozger, Z. Sen, Prediction of wave parameters by using fuzzy logic approach, Ocean Eng 34(3-4) (2007) 460-469.

[59] M.R. Belmont, J.M.K. Horwood, R.W.F. Thurley, J. Baker, Filters for linear sea-wave prediction, Ocean Eng 33(17-18) (2006) 2332-2351.

[60] F. Fusco, J.V. Ringwood, Short-Term Wave Forecasting for Real-Time Control of Wave Energy Converters, IEEE T Sustain Energ 1(2) (2010) 99-106.

[61] M. Ge, E.C. Kerrigan, Short-term ocean wave forecasting using an autoregressive moving average model, 11th International Conference on Control, IEEE, Belfast, UK, 2016, pp. 1-6.

[62] J.R. Halliday, D.G. Dorrell, A.R. Wood, An application of the Fast Fourier Transform to the short-term prediction of sea wave behaviour, Renew Energ 36(6) (2011) 1685-1692.

[63] D.Q. Truong, K.K. Ahn, Wave prediction based on a modified grey model MGM(1,1) for real-time control of wave energy converters in irregular waves, Renew Energ 43 (2012) 242-255.

[64] M.C. Deo, C.S. Naidu, Real time wave forecasting using neural networks, Ocean Eng 26(3) (1999) 191-203.

[65] J. Oh, K.D. Suh, Real-time forecasting of wave heights using EOF - wavelet - neural network hybrid model, Ocean Eng 150 (2018) 48-59.

[66] J.D. Agrawal, M.C. Deo, On-line wave prediction, Mar Struct 15(1) (2002) 57-74.

[67] S. Mandal, N. Prabaharan, Ocean wave forecasting using recurrent neural networks, Ocean Eng 33(10) (2006) 1401-1410.

[68] W.Y. Tseng, J. Dugundji, Nonlinear Vibrations of a Buckled Beam under Harmonic Excitation, J Appl Mech 38(2) (1971) 467-476.

[69] S.R. Panigrahi, B.P. Bernard, B.F. Feeny, B.P. Mann, A.R. Diaz, Snap-through twinkling energy generation through frequency up-conversion, J Sound Vib 399 (2017) 216-227.

[70] S. Baglio, V. Marletta, E. Pergolizzi, V. Ferrari, M. Ferrari, A.R. Bulsara, Nonlinear snap-through-buckling devices for energy harvesting from vibrations, Sensors, Springer2015, pp. 409-413.

[71] F. Cottone, P. Basset, H. Vocca, L. Gammaitoni, T. Bourouina, Bistable electromagnetic generator based on buckled beams for vibration energy harvesting, J Intel Mat Syst Str 25(12) (2014) 1484-1495.

[72] A.F. Arrieta, P. Hagedorn, A. Erturk, D.J. Inman, A piezoelectric bistable plate for nonlinear broadband energy harvesting, Appl Phys Lett 97(10) (2010).

[73] W. Godoy, M.A. Trindade, Design and optimization of a non-linear dynamic vibration absorber based on snap-through geometry, Proceedings of the 8th National Congress of Mechanical Engineering. ABCM, Uberlndia, Brazil, 2014.

[74] Z.Y. Zhou, W.Y. Qin, P. Zhu, Improve efficiency of harvesting random energy by snap-through in a quad-stable harvester, Sensor Actuat a-Phys 243 (2016) 151-158.

[75] X. Zhang, X. Tian, L. Xiao, X. Li, L. Chen, Application of an adaptive bistable power capture mechanism to a point absorber wave energy converter, Appl Energ 228 (2018) 450-467.

[76] A. Bharath, J.R. Nader, I. Penesis, G. Macfarlane, Nonlinear hydrodynamic effects on a generic spherical wave energy converter, Renew Energ 118 (2018) 56-70.

[77] R.W. Yeung, A. Peiffer, N. Tom, T. Matlak, Design, Analysis, and Evaluation of the UC-Berkeley Wave-Energy Extractor, J Offshore Mech Arct 134(2) (2012).

[78] P.C. Vicente, A.F.O. Falcao, P.A.P. Justino, Nonlinear dynamics of a tightly moored point-absorber wave energy converter, Ocean Eng 59 (2013) 20-36.

[79] J.L. Hess, A. Smith, Calculation of non-lifting potential flow about arbitrary three-dimensional bodies, DTIC Document, 1962.

[80] L. Li, Z.Q. Hu, J. Wang, Y. Ma, Development and Validation of an Aero-hydro Simulation Code for Offshore Floating Wind Turbine, J Ocean Wind Energy 2(1) (2015) 1-11.

[81] D.N. Veritas, WADAM—Wave Analysis by Diffraction and Morison Theory, SESAM user's manual, Høvik, 1994.

[82] M. Vantorre, R. Banasiak, R. Verhoeven, Modelling of hydraulic performance and wave energy extraction by a point absorber in heave, Applied Ocean Research 26(1-2) (2004) 61-72.

[83] H. Gao, Y. Yu, The dynamics and power absorption of cone-cylinder wave energy converters with three degree of freedom in irregular waves, Energy 143 (2018) 833-845.

[84] Q. Zhong, R.W. Yeung, An Efficient Convex Formulation for Model-Predictive Control on Wave-Energy Converters, ASME 2017 36th International Conference on Ocean, Offshore and Arctic Engineering, American Society of Mechanical Engineers, 2017, pp. V010T09A035-V010T09A035.

[85] J.C.C. Henriques, L.M.C. Gato, A.F.O. Falcao, E. Robles, F.X. Fay, Latching control of a floating oscillating-water-column wave energy converter, Renew Energ 90 (2016) 229-241.

[86] P. Frigaard, M. Brorsen, A Time-Domain Method for Separating Incident and Reflected Irregular Waves, Coastal Engineering 24(3-4) (1995) 205-215.

[87] M. Nielsen, Neural Networks and Deep Learning, 2017.

[88] W.S. Mcculloch, W. Pitts, A Logical Calculus of the Ideas Immanent in Nervous Activity, B Math Biol 5(4) (1943) 115-133.

[89] G.E. Hinton, S. Osindero, Y.W. Teh, A fast learning algorithm for deep belief nets, Neural Comput 18(7) (2006) 1527-1554.

[90] Y.S. Lv, Y.J. Duan, W.W. Kang, Z.X. Li, F.Y. Wang, Traffic Flow Prediction With Big Data: A Deep Learning Approach, Ieee T Intell Transp 16(2) (2015) 865-873.

[91] M.P. Islam, T. Morimoto, Non-linear autoregressive neural network approach for inside air temperature prediction of a pillar cooler, Int J Green Energy 14(2) (2017) 141-149.

[92] A. Pourzangbar, M.A. Losada, A. Saber, L.R. Ahari, P. Larroude, M. Vaezi, M. Brocchini, Prediction of non-breaking wave induced scour depth at the trunk section of breakwaters using Genetic Programming and Artificial Neural Networks, Coastal Engineering 121 (2017) 107-118.

[93] I. Ebtehaj, H. Bonakdari, F. Moradi, B. Gharabaghi, Z.S. Khozani, An integrated framework of Extreme Learning Machines for predicting scour at pile groups in clear water condition, Coastal Engineering 135 (2018) 1-15.

[94] Y. Li, Y. Fu, H. Li, S.W. Zhang, The Improved Training Algorithm of Back Propagation Neural Network with Self-adaptive Learning Rate, Proceedings of the 2009 International Conference on Computational Intelligence and Natural Computing, Vol I (2009) 73-76.

[95] D.E. Rumelhart, G.E. Hinton, R.J. Williams, Learning Representations by Back-Propagating Errors, Nature 323(6088) (1986) 533-536.

[96] L. Li, Z. Yuan, Y. Gao, X. Zhang, Wave force prediction effect on the energy absorption of a wave energy converter with real-time control, IEEE T Sustain Energ (2018) 1-1.

[97] L. Li, Y. Gao, Z.Q. Hu, Z.M. Yuan, S. Day, H.R. Li, Model test research of a semisubmersible floating wind turbine with an improved deficient thrust force correction approach, Renew Energ 119 (2018) 95-105.

[98] X. Hong, S. Billings, Time series multistep‐ahead predictability estimation and ranking, Journal of Forecasting 18(2) (1999) 139-149.

[99] L. Li, Z. Gao, T. Moan, Joint Distribution of Environmental Condition at Five European Offshore Sites for Design of Combined Wind and Wave Energy Devices, J Offshore Mech Arct 137(3) (2015) 031901.

[100] A. Naess, T. Moan, Stochastic dynamics of marine structures, Cambridge University Press2012.

[101] Z.S. Cheng, H.A. Madsen, W. Chai, Z. Gao, T. Moan, A comparison of extreme structural responses and fatigue damage of semi-submersible type floating horizontal and vertical axis wind turbines, Renew Energ 108 (2017) 207-219.

[102] L. Li, Z.S. Cheng, Z.M. Yuan, Y. Gao, Short-term extreme response and fatigue damage of an integrated offshore renewable energy system, Renew Energ 126 (2018) 617-629.

[103] H.R. Li, Z.Q. Hu, J. Wang, X.Y. Meng, Short-term fatigue analysis for tower base of a spar-type wind turbine under stochastic wind-wave loads, International Journal of Naval Architecture and Ocean Engineering (2017).

[104] E. Marino, A. Giusti, L. Manuel, Offshore wind turbine fatigue loads: The influence of alternative wave modeling for different turbulent and mean winds, Renew Energ 102 (2017) 157-169.

[105] R.G. Coe, C. Michelen, A. Eckert-Gallup, C. Sallaberry, Full long-term design response analysis of a wave energy converter, Renewable Energy (2017).

[106] S.R. Winterstein, T.C. Ude, C.A. Cornell, P. Bjerager, S. Haver, Environmental parameters for extreme response: Inverse FORM with omission factors, Proceedings of the ICOSSAR-93, Innsbruck, Austria (1993) 551-557.

[107] Y. Xiang, Y. Liu, Application of inverse first-order reliability method for probabilistic fatigue life prediction, Probabilistic Engineering Mechanics 26(2) (2011) 148-156.

[108] M.J. Muliawan, Z. Gao, T. Moan, Application of the Contour Line Method for Estimating Extreme Responses in the Mooring Lines of a Two-Body Floating Wave Energy Converter, J Offshore Mech Arct 135(3) (2013).

[109] A. Naess, O. Gaidai, Monte Carlo methods for estimating the extreme response of dynamical systems, J Eng Mech-Asce 134(8) (2008) 628-636.

[110] NWTC Information Portal, Mlife, 2017.
https://nwtc.nrel.gov/MLife.
(Accessed 15-September 2017).

[111] DNV, Fatigue design of offshore steel structures, No. DNV-RP-C203, 2010.

[112] Q.Y. Li, Z. Gao, T. Moan, Modified environmental contour method to determine the long-term extreme responses of a semi-submersible wind turbine, Ocean Eng 142 (2017) 563-576.

Publications

Journals

[1] **L. Li**, X.T. Z.M. Yuan, Y. Gap, *Multi-stable mechanism of an oscillating-body wave energy converter*, **IEEE Transactions on Sustainable Energy** (2019), available on-line.

[2] **L. Li**, Z.M. Yuan, C.Y. Ji, Y. Gao, *Ultimate structural and fatigue damage loads of a spar-type floating wind turbine*, **Ships and Offshore Strucutres** (2018).

[3] **L. Li**, Z.M. Yuan, Y. Gao, X.T. Zhang, T. Tezdogan, *Investigation on long-term extreme response of an integrated offshore renewable energy device with a modified environmental contour method*, **Renewable Energy** 132 (2019) 33-42.

[4] **L. Li**, Z.M. Yuan, Y. Gao, *Maximization of energy absorption for a wave energy converter using the deep machine learning*, **Energy** 165(A) (2018) 340-349.

[5] **L. Li**, Z.S. Cheng, Z.M. Yuan, Y. Gao, *Short-term extreme response and fatigue damage of an integrated offshore renewable energy system*, **Renewable Energy** 126 (2018) 617-629.

[6] **L. Li**, Y. Gao, Z.Q. Hu, Z.M. Yuan, S. Day, H.R. Li, *Model test research of a semisubmersible floating wind turbine with an improved deficient thrust force correction approach*, **Renewable Energy** 119 (2018) 95-105.

[7] **L. Li**, Y. Gao, Z.M. Yuan, S. Day, Z.Q. Hu, *Dynamic response and power production of a floating integrated wind, wave and tidal energy system*, **Renewable Energy** 116 (2018) 412-422.

[8] **L. Li**, Y. Liu, Z.M. Yuan, Y. Gao, *Wind field effect on the power generation and aerodynamic performance of offshore floating wind turbines*, **Energy** 157 (2018) 379-390.

[9] **L. Li**, Z.M. Yuan, Y. Gao, X.S. Zhang, *Wave force prediction effect on the energy absorption of a wave energy converter with real-time control*, **IEEE Transactions on Sustainable Energy** (2018), In Press.

[10] **L. Li**, Z.M. Yuan, Y. Gao, *Wash wave effects on ships moored in ports*, **Applied Ocean Research** 77 (2018) 89-105.
[11] **L. Li**, Z.M. Yuan, C.Y. Ji, M.X. Li, Y. Gao, *Investigation on the unsteady hydrodynamic loads of ship passing by bridge piers by a 3-D boundary element method*, **Engineering Analysis with Boundary Elements** 94(C) (2018) 122-133.

Conferences Proceedings

[12] **L. Li**, Y. Gao, Z.M. Yuan, *Real-time latching control of wave energy converter with consideration of wave force prediction*, OTO'18, Kobe, 2018.
[13] **L. Li**, Z.M. Yuan, Y. Gao, *Dynamic Response and Power Production of an Integrated Offshore Renewable Energy System*, The 28th International Ocean and Polar Engineering Conference, International Society of Offshore and Polar Engineers, Sapporo, Japan, 2018.

Appendix A

There are generally two categories of coordinate systems in the discretization of the fluid boundaries: the reference coordinate system and element coordinate system. The input data and the influence coefficients should be based on the reference coordinate system, while the element coordinate system is used for calculating the exact induced velocity component. The transformation matrix can be obtained easily to transform the coordinate. Consider a plane quadrilateral source element lying in the $\xi\eta$-plane (element coordinate system) as shown in Figure 4.1. The source density of panel Q is written as $\sigma(Q)$. Denote the number of panels on body, free and control surface as N_B, N_F and N_C respectively. Apart from the reference coordinate system O-XYZ, an element system O'-$\xi\eta\zeta$ is established with O' on the geometry centroid and ζ axis on its normal vector, as shown in Fig. 1.

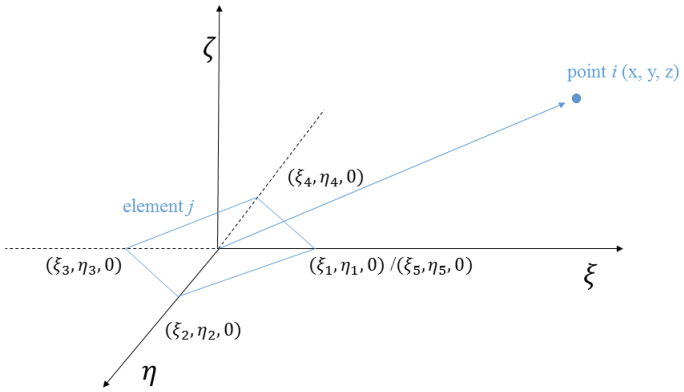

Fig. 1 A plane quadrilateral source element.

As shown in Fig. 1, a plane element j induces potential φ_{ij} at point i. σ_j is the the source strength assigned to element j. Following the definition of Hess and Smith [79], φ_{ij} is given by

$$\varphi_{ij} = G_{ij} \cdot \sigma_j \tag{A.1}$$

where G_{ij} is the influence coefficient

$$G_{ij} = \sum_{k=1}^{4} \frac{(\xi_{k+1} - \xi_k)(y - \eta_k) - (\eta_{k+1} - \eta_k)(x - \xi_k)}{l_{k,k+1}} \cdot \ln \frac{r_k + r_{k+1} + l_{k,k+1}}{r_k + r_{k+1} - l_{k,k+1}} + z \cdot \frac{\partial \varphi_{ij}}{\partial \zeta} / \sigma_j \tag{A.2}$$

$$r_k = \sqrt{(x-\xi_k)^2 + (y-\eta_k)^2 + (z-\zeta_k)^2} \tag{A.3}$$

$$l_{k,k+1} = \sqrt{(\xi_{k+1}-\xi_k)^2 + (\eta_{k+1}-\eta_k)^2} \tag{A.4}$$

$$m_{k,k+1} = \frac{\eta_{k+1}-\eta_k}{\xi_{k+1}-\xi_k} \tag{A.5}$$

$$e_k = z^2 + (x-\xi_k)^2 \tag{A.6}$$

$$h_k = (y-\eta_k)(x-\xi_k) \tag{A.7}$$

The gradient of potential is given by

$$\begin{aligned}
\frac{\partial \varphi_{ij}}{\partial \xi} &= \frac{\partial G_{ij}}{\partial \xi}\cdot\sigma_j = -\sigma_j \cdot \sum_{k=1}^{4} \frac{\eta_{k+1}-\eta_k}{l_{k,k+1}} \cdot \ln \frac{r_k + r_{k+1} + l_{k,k+1}}{r_k + r_{k+1} - l_{k,k+1}} \\
\frac{\partial \varphi_{ij}}{\partial \eta} &= \frac{\partial G_{ij}}{\partial \eta}\cdot\sigma_j = \sigma_j \cdot \sum_{k=1}^{4} \frac{\xi_{k+1}-\xi_k}{l_{k,k+1}} \cdot \ln \frac{r_k + r_{k+1} + l_{k,k+1}}{r_k + r_{k+1} - l_{k,k+1}} \\
\frac{\partial \varphi_{ij}}{\partial \zeta} &= \frac{\partial G_{ij}}{\partial \zeta}\cdot\sigma_j = \sigma_j \sum_{k=1}^{4} \left(\arctan \frac{m_{k,k+1}e_k - h_k}{z r_k} - \arctan \frac{m_{k,k+1}e_{k+1} - h_{k+1}}{z r_{k+1}} \right)
\end{aligned} \tag{A.8}$$

In the case of $z = 0$ (point i and element j are located in the same plane), $\frac{\partial \varphi}{\partial \zeta} = 2\pi$ if point i is within the plane element; $\frac{\partial \varphi}{\partial \zeta} = 0$ if point i is within the plane element [79].

Discretizing the entire boundary in to N elements, the potential and the velocity at the centre of element i are given by

$$\varphi_i = \sum_{j=1}^{N} G_{ij} \cdot \sigma_j \tag{A.9}$$

$$\frac{\partial \varphi_i}{\partial \xi} = \sum_{j=1}^{N} \frac{\partial G_{ij}}{\partial \xi} \cdot \sigma_j$$
$$\frac{\partial \varphi_i}{\partial \eta} = \sum_{j=1}^{N} \frac{\partial G_{ij}}{\partial \eta} \cdot \sigma_j \qquad \text{(A.10)}$$
$$\frac{\partial \varphi_i}{\partial \zeta} = \sum_{j=1}^{N} \frac{\partial G_{ij}}{\partial \zeta} \cdot \sigma_j$$

Substitute the two expressions into the boundary value formula, and the source strengths assigned to each element are determined.

Appendix B

Step1: At time step t_i, collect the raw data $\boldsymbol{X}$ over the past few seconds

$$\boldsymbol{X} = \left(x_1, x_2, ..., x_n \right) \tag{B.1}$$

Step2: Generate an accumulated series $\boldsymbol{Y}$

$$\begin{aligned} \boldsymbol{Y} &= \left(y_1, y_2, ..., y_n \right) \\ y_k &= \sum_{i=1}^{k} x_i, k = 1, 2, ..., n \end{aligned} \tag{B.2}$$

Step3: Generate the so-called background series $\boldsymbol{Z}$

$$\begin{aligned} \boldsymbol{Z} &= \left(z_2, z_3, ..., z_n \right) \\ z_k &= \left(y_k + y_{k-1} \right) / 2 \end{aligned} \tag{B.3}$$

Step4: Set the grey differential formula

$$x_k + a z_k = b, k = 2, 3, .., n \tag{B.4}$$

Step5: Estimate parameters a and b with the least square method

$$\begin{aligned} \begin{bmatrix} a \\ b \end{bmatrix} &= \left(\boldsymbol{A}^T \boldsymbol{A} \right)^{-1} \boldsymbol{A}^T \boldsymbol{B} \\ \boldsymbol{A} &= \begin{bmatrix} -z_2 & 1 \\ -z_3 & 1 \\ \vdots & \vdots \\ -z_n & 1 \end{bmatrix}, \boldsymbol{B} = \begin{bmatrix} x_2 \\ x_3 \\ \vdots \\ x_n \end{bmatrix} \end{aligned} \tag{B.5}$$

Step6: Establish the first order-one variable grey model GM(1,1) to predict the random signal within interval [t_{i+1},t_{i+p}]

$$\begin{aligned} \hat{x}_{n+p} &= \hat{y}_{n+p} - \hat{y}_{n+p-1} \\ \hat{y}_{n+p} &= \left(y_1 - \frac{b}{a} \right) e^{-a(n+p-1)} + \frac{b}{a} \end{aligned} \tag{B.6}$$

where $\hat{x}_{n+p}$ is the predicted data at time step t_{i+p}.